Dynamics of Compressible Convection and Thermochemical Mantle Convection

by **Xi Liu**

B.S., University of Science and Technology of China, 2010

A thesis submitted to the

Faculty of the Graduate School of the

University of Colorado in partial fulfillment

of the requirement for the degree of

Doctor of Philosophy

Department of Physics

2016

This thesis entitled:

Dynamics of Compressible Convection and Thermochemical Mantle Convection

written by Xi Liu

has been approved for the Department of Physics

_____

Shijie Zhong

_____

Michael Ritzwoller

Date_____

The final copy of this thesis has been examined by the signatories, and we find that both the content and the form meet acceptable presentation standards of scholarly work in the above mentioned discipline.

Liu, Xi (Ph.D., Geophysics, Department of Physics)

Dynamics of Compressible Convection and Thermochemical Mantle Convection

Thesis directed by Professor Shijie Zhong.

Abstract: The Earth's long-wavelength geoid anomalies have long been used to constrain the dynamics and viscosity structure of the mantle in an isochemical, whole-mantle convection model. However, there is strong evidence that the seismically observed large low shear velocity provinces (LLSVPs) in the lowermost mantle are chemically distinct and denser than the ambient mantle. In this thesis, I investigated how chemically distinct and dense piles influence the geoid. I formulated dynamically self-consistent 3D spherical convection models with realistic mantle viscosity structure which reproduce Earth's dominantly spherical harmonic degree-2 convection. The models revealed a compensation effect of the chemically dense LLSVPs. Next, I formulated instantaneous flow models based on seismic tomography to compute the geoid and constrain mantle viscosity assuming thermochemical convection with the compensation effect. Thermochemical models reconcile the geoid observations. The viscosity structure inverted for thermochemical models is nearly identical to that of whole-mantle models, and both prefer weak transition zone. Our results have implications for mineral physics, seismic tomographic studies, and mantle convection modelling.

Another part of this thesis describes analyses of the influence of mantle compressibility on thermal convection in an isoviscous and compressible fluid with infinite Prandtl number. A new formulation of the propagator matrix method is implemented to compute the critical Rayleigh number and the corresponding eigenfunctions for compressible convection. Heat flux and thermal boundary layer properties are quantified in numerical models and scaling laws are developed.

Dedication

This thesis is dedicated to my parents and my thesis advisor.

Acknowledgements

I am very fortunate to have come to join the CU-Boulder geophysics PhD program and worked with my thesis advisor, Professor Shijie Zhong. In the past six years I had the chance to get the best training for a young geophysicist. This thesis marks a milestone in my life and would always remind me of the happiness and challenges along my journey of the scientific exploration guided by my advisor on 7th floor of Gamow Tower on beautiful CU-Boulder campus.

I owe my greatest gratitude to my thesis advisor, Professor Shijie Zhong. This thesis would not exist without his guidance and encouragement. I vividly remembered how excited but also fearful when I first came abroad and started in the graduate school. Back then I was not sure about what scientific research is, how I can approach that, and what does it mean to be a good researcher. For six years Shijie has led me from the foothill to a viewpoint on the trail of geoscience despite lots of obstacles, and he constantly encourages me to keep going, to tackle problems and appreciate the strength I gained, and to expect the unknown wonderful scenes in front of me. During the six years of mentorship and collaboration, I gradually formed a picture of what a great scientist and teacher is like and Shijie provides as a role model to me. Shijie is always very passionate and engaged. He pursues his interest in geoscience and makes solid progress without being easily disturbed. I view him as a pure scholar, and his

attitude towards scientific exploration deeply influenced me. Shijie is a great advisor, too. He put tremendous amounts of time on his students. He trusts me and makes effort to understand me. He is always looking for my strengths, pointing out opportunities for me, and helping to expand my horizon. He keeps telling me that 'sky is the limit'. There have been many difficulties in the process, and Shijie teaches me to be optimistic and patient while focusing on my daily work. During the time working with Shijie, I have not only been trained to be a young scientist, but also grown up to be a better person, a more responsible and honest one that is confident and ready for my future life. Shijie inspires me so much, and as the historian Sima Qian pointed out: 'man of high virtue, like lofty mountains, earn our respect and admiration. Although it is difficult to reach this state of mind, I always yearn to be such man'.

I want to thank my dear friends who have spiritually supported me. I know Marty the first month I came to United States. She is like my mother in Boulder and has accompanied me and supported me during my ups and downs. We share similar interests and talk about everything. Jiayi and I were college roommates in China, and we also worked on the same floor here in Boulder. We have been friends for ten years and those are the most beautiful ten years in our lives. Sijia is my roommate here, and she is like my elder sister. She is the kindest person I have ever known and I am very grateful for her support during my stressful graduate school life. Ling is a tough and cheerful woman, and she teaches me to be independent and to enjoy my life. I had so much fun with my friends. Now we are heading to different places. I want to say many thanks to them and our time spent together in Boulder would be a most precious part in my memory.

I owe my gratitude to Boulder, a fantastic place where I now view as my second hometown. I will never forget how people here helped me, especially when I first came here. The Boulder Creek flowing not far from my apartment and the Flatirons sighted every day from my office make me feel peaceful. The students on campus make me feel energetic. They are beautiful scenery in Boulder and would remain in my memory forever.

I want to thank Professor Michael Ritzwoller for teaching me and talking to me about science and my career. I am deeply impressed by his comment that 'science is not about fancy, and when you focus and do it, fancy come along the way.' Professor John Wahr was a great scientist and was so kind to the students. Professor Lang Farmer and Professor Mark Rast broadened my view by making the class an adventure. I owe thanks to Professor Craig Jones and Professor Michael Calkins for being my committee and providing valuable comments. I am also grateful for my past and current group members including but not exclusively, Wei, Nan, Geruo, Tao, Chuan, Ashley, and Mingming, for our computer engineer Misha Barmine and for our administrative secretary Teri Keeler. They have offered their kind help to me.

I am thankful for University of Science and Technology of China, where I got my bachelor's degree. USTC benefited me with the solid mathematics and physics training. Moreover, I was influenced by scholars there, and I owe special thanks to my senior undergraduate thesis advisor Professor Jinshui Huang and other respected professors such as Professor Rongshan Fu, and Professor Xiaofei Chen.

Last, I want to say thank you to my parents and my sister. I am super lucky to have you and to be a member of our family. You are the best. Your love gives me the

courage to overcome all difficulties not only in my graduate school, but also in the unknown and wonderful future.

Contents

Chapter

Tables

Table

Figures

Figure

Chapter 1

Introduction

1.1. Compressible mantle convection

Thermal convection within planetary mantles controls thermal and dynamic evolution of planets. Most studies on Earth's mantle convection employ a Boussinesq approximation that assumes an incompressible mantle. Classic studies with the Boussinesq approximation provide an important understanding of Earth's mantle convection and interior dynamics (e.g., McKenzie *et al*., 1974).

As more exoplanets or super-Earths are detected (e.g., Charbonneau *et al*., 2009), there is a growing interest in understanding the mantle dynamics for these planets (e.g., O'Neill & Lenardic, 2007; Valencia *et al*., 2007; Van Heck & Tackley, 2011; Foley *et al*., 2012). A distinct character of super-Earths' mantles is their very large compressibility and Rayleigh number, due to their sizes and masses.

By formulating compressible mantle convection models, a number of studies have examined the effects of compressibility including depth-dependent density, viscous heating, and adiabatic heating (e.g., Jarvis & McKenzie, 1980; Steinbach, Hansen, & Ebel, 1989). In particular, large compressibility has a critical effect on mantle plume dynamics. Leng & Zhong (2008b) reported that the compressibility has a controlling effect on plume excess temperature and plume heat flux. It has also been

demonstrated that the number of plumes is reduced in compressible convection since small scale plumes merge to form super-plumes (Balachandar, Yuen, & Reuteler, 1992; Thompson & Tackley, 1998; Tan & Gurnis, 2005).

However, to better understand the thermal and atmosphere evolution of terrestrial planets with large compressibility, more studies are needed on the marginal stability analysis and scaling laws of convective heat flux for compressible mantle convection. Marginal stability analysis has been performed for compressible convection, but only with limited parameters and restricted boundary conditions (Jarvis & McKenzie, 1980; Bercovici *et al*., 1992). While scaling laws of heat flux and thermal boundary layer properties are well understood for Cartesian incompressible thermal convection, they remain poorly understood for compressible convection.

In Chapter 2, I described a marginal linear stability analysis on compressibility mantle convection using a new technique based on a propagator matrix method. I also computed finite amplitude compressible models with a wide range of mantle compressibility and Rayleigh number, and derive scaling laws for thermal boundary layer (TBL) properties and convective heat transfer.

1.2. The Earth's long wavelength structure from the geoid observation and seismic tomographic models

The Earth's gravitational equipotential surface that defines the sea level, the geoid, provides fundamental constraints on the Earth's interior structure (e.g., Hager and Richards, 1989; Ricard et al., 1993). With advances of the space satellite geodesy, the Earth geoid has been mapped in an ever high resolution with unprecedented details. It has long been noticed that the non-hydrostatic geoid is prevalently at long wavelengths (Lerch *et al*., 1983) and is characterized by a dominantly spherical

harmonic degree-2 structure with two geoid highs above Africa and the Pacific Ocean. While the geoid features at shorter wavelength, such as positive geoid at convergent zones, are associated with plate tectonics (e.g., Hager, 1984), the very long wavelength geoid (e.g., degree-2) shows little tectonic patterns and its primary source lies deep in the mantle (e.g., Hager & Richards, 1989).

The geoid is controlled by lateral density variations including both the interior buoyancy and those from deflections of internal and external boundaries (e.g., Pekeris, 1935; Hager and Richards, 1989). The isostatic component of the deflections (i.e., topographies) is fully compensated and makes zero contribution to the geoid, and the geoid modelling only considers the dynamic topographies (i.e., the residual topographies) that are supported by vertical stresses induced by the mantle flow (e.g., Hager, *et al*., 1985). The dynamic topographies, which are computed by solving the Stokes' flow equations, have a strong dependence on, and thus can constrain, the mantle viscosity profile (e.g., Hager and Richards, 1989). As a result, the Earth's non-hydrostatic geoid provides important constraints on the structure, rheology, and dynamics of the mantle (e.g., Hager and Richards, 1989; Ricard et al., 1993), making it an essential piece of information in probing the internal structure of the dynamic Earth by its surface manifestations.

Earth's internal structure can be more directly imaged by seismic methods (e.g, Dziewonski, 1984). Seismic wave anomalies can be mapped by tomographic inversions of seismic data. Seismic slow anomalies are typically associated with hot and buoyant mantle materials, while fast wave anomalies imply relatively cold materials (e.g., cold downwellings). The mantle tomographic models have clearly shown slow anomalies below mid-ocean ridges and hotspot, and fast anomalies beneath continent shields and subduction zones (e.g., Dziewonski, 1984; Tanimoto,

1990) in the shallow depths. However, the most prominent feature in all recent tomographic models are a dominantly degree-2 structure in the lower mantle, with two large low shear velocity provinces (LLSVPs) extending several hundred kilometers above the CMB below Africa and the Pacific Ocean, which are surrounded by seismically fast, circum-Pacific anomalies (e.g., Dziewonski, 1984; Tanimoto, 1990; Masters *et al*., 1996; Ritsema *et al*., 1999). These degree-2 anomalies are continuous across the mantle, despite weaker anomalies in the mid-mantle and more tectonic features at shorter wavelength in the shallow depths (e.g., Ritsema *et al*., 2011).

The seismic anomalies are often interpreted as purely due to the thermal effect in an isochemical, whole mantle convection framework, and the LLSVPs are thought as hot and buoyant roots of the 'super-plumes' that extend to the upper mantle, form the upwelling part of the global mantle convection, and cause the African and Pacific super-swell topography (e.g., Marty and Cazenave, 1989; Davies and Pribac, 1993; Lithgow-Bertelloni and Silver, 1998; Romanowicz and Gung, 2002). Representing the seismic structures as mantle density and buoyancy structure in the purely thermal, whole mantle convection model, geodynamic studies have not only reproduced the Earth's geoid, but also provided constraints on the mantle viscosity structure (e.g. Hager & Richards, 1989). Assuming thermal LLSVPs, Lithgow-Berterlloni and Silver (1993) also explains the dynamic topography which, similarly to the geoid, has two prominent topographic highs over southeast Africa and south Pacific.

1.3. Earth's mantle is compositionally heterogeneous

Purely thermal and whole mantle convection apparently means fast mixing and homogenization in the convective system. The Earth's mantle, however, is far

from being homogenized (e.g., Hofmann, 1997). Rich varieties of geochemical signatures found in mantle derived basalts suggest a mantle with complex composition reservoirs (e.g., Hofmann, 1997; Kellogg *et al*., 1999; Kunz *et al*., 1998). Fundamental geochemical differences have been found between the mid-ocean basalts (MORB) which sample the relatively depleted upper mantle, and oceanic island basalts (OIB) which are less depleted or even enriched in incompatible or radiogenic elements (e.g., Schilling, 1973). Although their exact mantle sources are still uncertain, OIBs have been proposed as created by plumes rising from the deep mantle (e.g., Morgan, 1971), and can shed lights to the lower mantle thermochemical structure as well as the differentiation and evolution of the Earth (e.g., Hofmann *et al*., 1986; Hofmann, 1997). Compositional distinct mantle layers and potentially primitive reservoirs in the lower mantle are two candidates of the origins of OIBs. Indeed, the layered mantle convection, where upper mantle and lower mantle are compositionally distinct materials and have separate convective systems, has long been the 'standard model' in geochemical studies (e.g., Schilling, 1973). However, the layered convection model fails to reconcile the Earth's geoid: to reproduce the observed geoid, a huge undulation at the compositional boundary at 670 km depth would occur in the layered mantle convection model, which contradicts the seismic observations (Hager & Richards, 1989). Can we propose mantle convection models that would reproduce both the geochemical signatures and the geoid?

Recently, seismic studies suggest that LLSVPs might be chemically distinct and dense piles. The anti-correlation between shear wave and bulk sound speeds in the LLSVPs suggests a thermochemical origin for the seismic heterogeneities in these regions (e.g., Masters et al. 2000). The sharp seismic velocity contrasts at the edges of LLSVPs are better explained as features of chemically distinct piles rather than purely

thermal anomalies (Wen *et al*., 2001; Ni *et al*., 2002). The thermochemical characteristics of the LLSVPs reconcile geochemical inferences of chemically distinct "reservoirs" that explain the difference between the oceanic island basalt (OIB) and the mid-ocean ridge basalt (MORB) (e.g., Hofmann, 1997; Kellogg et al., 1999; Kunz et al., 1998), and promote the studies of thermochemical mantle mode with chemically distinct piles in the lowermost mantle.

The large-scale chemically distinct piles, if they represent the LLSVPs as proposed (e.g., Garnero and McNamara, 2008), may have significant effects on the mantle dynamics. It has been suggested that thermochemical structures in the mantle affect the buoyancy force distribution, mantle flow configuration and convective heat transfer (e.g., Tackley, 1998; Kellogg *et al*., 1999; Davaille, 1999; McNamara and Zhong, 2005a; Zhang *et al*., 2010). However, the effects of thermochemical structures on the geoid are not well understood.

1.4. Geoid modelling of thermochemical mantle convection models

The geoid modelling using instantaneous mantle flow models based on seismic velocity anomalies can provide a critical constraint on the mantle rheology and buoyancy structure. However, constructing buoyancy structure from the seismic tomographic models in those chemically heterogeneous regions is difficult due to the mixture of both thermal and compositional effects, and uncertainties in seismic, compositional and mineral physics mantle models. In their geoid modelling study, Steinberger & Torsvik (2010) simply removed the buoyancy structure of the thermochemical layer (i.e., bottom 300 km of the mantle). Through a joint inversion of the geoid and seismic data with a parameterization of possible compositional effect on the buoyancy, Forte & Mitrovica (2001) concluded that the LLSVPs are overall

positively buoyant in order to fit the geoid (Forte and Mitrovica, 2001), thus raising the question of whether LLSVPs represent stable thermochemical structures over long time scales.

With all the difficulties in the direct geoid modelling based on seismic tomographic models, we seek to firstly examine the effects of chemical piles (e.g., the LLSVPs) on the geoid as well as whether positive geoid anomalies in a largely degree-2 convection as for the present-day Earth can be generated above stable chemical piles based on dynamically self-consistent mantle convection models.

A key in formulating dynamically self-consistent convection models to investigate the effects of thermochemical piles on the Earth's geoid is to generate long-wavelength convective structure with two major thermochemical piles above the CMB. This is accomplished here by modeling thermochemical convection (e.g., McNamara and Zhong, 2004a) with modestly strong lithosphere and a weak upper mantle (Zhong et al., 2007).

In time-dependent, dynamically self-consistent thermochemical mantle convection models, I found that the general characteristics of the surface geoid and dynamic topography over stable dense thermochemical piles, after reaching a dynamic equilibrium, resemble the observations. Additionally, I will show that dense thermochemical piles have a compensation effect on the geoid such that the bottom ~1000 km of the mantle (i.e., a compensation layer), or 2 to 3 times of the maximum thickness of the chemical piles, has a zero net contribution to the geoid at long wavelengths. As analyzed in Chapter 3, the compensation effect occurs because the geoid anomalies from negatively buoyant chemical piles are offset by those from hot and buoyant normal mantle above the piles.

Considering the compensation effect, the geoid modelling for the thermochemical model with stable chemical piles can be done following the same approach as that for whole mantle models (e.g., Hager & Richards, 1989) except that the mantle buoyancy structure in the compensation layer, including the LLSVPs, needs to be removed. The mantle above the compensation layer can be seen as isochemical with buoyancy structure that can be determined from seismic tomographic models with a conversion factor (e.g., Hager & Richards, 1989; Forte & Mitrovica, 2001; Ghosh, et al., 2010).

I then investigated how well the geoid can be explained in instantaneous flow models in which mantle buoyancy structure is derived from seismic tomographic models considering the compensation effect for the thermochemical mantle as described in Chapter 4. This study also re-examines the geoid constraints on mantle viscosity structure for a thermochemical mantle and compares the inverted mantle viscosity with that inferred from previous purely thermal mantle models.

1.5. Organization of the thesis

This thesis is organized as follows: Chapter 2 presents the work on the compressible mantle convection, Chapter 3 describes the study about the effects of chemically dense piles on the long wavelength geoid using dynamically self-consistent thermochemical mantle convection models, Chapter 4 presents the study of the geoid modelling based on seismic tomographic models assuming thermochemical convection considering the compensation effect by heavy chemical pile, and Chapter 5 summarizes this thesis.

Chapter 2

Analyses of Marginal Stability, Heat Transfer and Boundary Layer Properties for Thermal Convection in a Compressible Fluid with Infinite Prandtl Number[1]

Abstract: Thermal and dynamical evolution of planets is controlled by thermal convection in planetary mantles. Mantle compressibility, which measures volume change due to pressure change and its associated energetic effects, can have important effects on planetary mantle convection. However, key issues including marginal stability analysis, thermal boundary properties, and heat transfer in compressible mantle convection are not well understood. This paper studies the influence of mantle compressibility on thermal convection in an isoviscous and compressible fluid with infinite Prandtl number, using both marginal stability analysis and numerical modeling. For the marginal stability analysis, a new formulation of the propagator matrix method is implemented to compute the critical Rayleigh number Ra_c and the corresponding eigenfunctions for compressible convection at different wavelengths (i.e., wavenumber k_x) and dissipation number *Di* which measures the compressibility. Ra_c from the analysis is in a good agreement with that determined from the numerical experiment using the eigenfunctions as initial perturbations. Our study suggest that if *Ra* is defined by the surface density, the minimum Ra_c may occur at non-zero *Di*. Finite element models are computed for compressible mantle convection at different *Ra* and *Di*. Heat flux and thermal boundary layer (TBL) properties including boundary layer thickness and temperature difference are quantified and analyzed from the numerical results. Scaling laws of temperature differences

[1] This chapter was published as "Liu, X., and S.J. Zhong, 2013. Analysis of marginal stability, heat transfer and boundary layer propoerties for thermal convection in a compressible fluid, *Geophys. J. Int*, **194**, 125-144"

across TBLs and of the heat flux are derived analytically for compressible mantle convection and are verified by the numerical results. This study shows that while TBL thicknesses and the heat flux are still scaled with Ra to the -1/3 and 1/3 power, respectively, as those for incompressible convection, they also strongly depend on Di. In particular, compressibility breaks the symmetry for the top and bottom TBLs, and the ratios of thickness and temperature difference for the top TBL to those for the bottom TBL are $exp(Di/2)$. These results have important implications for compressible mantle convection.

2.1. Introduction

Thermal convection within planetary mantles controls thermal and dynamic evolution of planets. Most studies on Earth's mantle convection employ a Boussinesq approximation that assumes an incompressible mantle. Classic studies with the Boussinesq approximation provide an important understanding of Earth's mantle convection and interior dynamics (e.g., McKenzie *et al*., 1974). However, by formulating compressible mantle convection models, a number of studies have also examined the non-Boussinesq effects including depth-dependent density, viscous heating, and adiabatic heating (e.g., Jarvis & McKenzie, 1980; Steinbach *et al*., 1989).

In their classic work on compressible mantle convection, Jarvis & McKenzie (1980) formulated a 2D Cartesian model and systematically investigated the marginal stability problem and finite amplitude convection. Other models of compressible convection have been formulated to examine the effects of equations of state (Ita & King, 1994), variable viscosity (Tackley, 1996), spherical geometry (Bercovici *et al*., 1992), and dynamic pressure in the buoyancy term (Leng & Zhong, 2008a). Recently, Tan *et al*. (2011) incorporated variable viscosity and material properties into 3D spherical models of compressible mantle convection. Also, a number of studies showed that mantle compressibility has significant effects on plume dynamics. It has been demonstrated that the number of plumes is reduced in compressible convection since small scale plumes merge to form super-plumes (Balachandar *et al*., 1992; Thompson & Tackley, 1998; Tan & Gurnis, 2005). Leng & Zhong (2008b) reported that the compressibility has a controlling effect on plume excess temperature and plume heat flux. Tan *et al*. (2011) found that in a compressible mantle, the plumes form around the edges of chemical 'domes' at the core mantle boundary.

However, more studies are needed to better understand the marginal stability analysis and scaling laws of convective heat flux for compressible mantle convection. Marginal stability analysis was performed for compressible convection with limited parameters and restricted boundary conditions (Jarvis & McKenzie, 1980; Bercovici *et al*., 1992). While scaling laws of heat flux and thermal boundary layer properties are well understood for Cartesian incompressible thermal convection, they remain poorly understood for compressible convection. Recently, as more exoplanets or super-Earths are detected (e.g., Charbonneau *et al*., 2009), there is a growing interest in understanding the mantle dynamics for these planets (e.g., O'Neill & Lenardic, 2007; Valencia *et al*., 2007; Van Heck & Tackley, 2011; Foley, Bercovici *et al*., 2012). A distinct character of super-Earths' mantles is their very large compressibility and Rayleigh number, due to their sizes and masses. Most of previous studies on compressible mantle convection considered compressibility in a range appropriate to Earth, and now it is necessary to consider larger compressibility.

In this study, we perform marginal linear stability analysis using a new technique based on a propagator matrix method. We also compute finite amplitude compressible models with a wide range of mantle compressibility and Rayleigh number, and derive scaling laws for thermal boundary layer (TBL) properties and convective heat transfer. In the following section, we present model formulation and governing equations. In section 2.3, we show results for the marginal stability analysis of compressible convection. In section 2.4, we present finite amplitude convection calculations and derive scaling laws for TBL properties and heat flux. In sections 2.5 and 2.6, we discuss the implications of our results for compressible convection and make concluding remarks.

2.2. Model formulation

2D Cartesian models are formulated with an anelastic-liquid approximation (ALA) (e.g., Jarvis & McKenzie, 1980; Schubert, Turcotte, & Olson, 2001). ALA uses depth-dependent parameters, notably density $\rho_r(z)$ as reference state in the governing equations. In this study, parameters such as viscosity, thermal conductivity, specific heat, and thermal expansion are assumed constant in our models unless otherwise indicated.

$\rho_r(z)$ is determined by the Adams-Williamson equation of state by Birch (1952):

$$\frac{1}{\rho_r}\frac{\mathrm{d}\rho_r}{\mathrm{dz}} = -\frac{\alpha g}{c_P \Gamma} \ , \tag{2.1}$$

where z is the vertical coordinate pointing upwards, g is gravitational acceleration, α is the coefficient of thermal expansion, c_P is the specific heat at constant hydrostatic pressure, and Γ is the Grüneisen's parameter and is defined as

$$\Gamma = \frac{\alpha \mathrm{K}_S}{\rho c_P} \ , \tag{2.2}$$

where K_S is the isentropic bulk modulus. Notice that in our model with homogeneous composition, isentropic and adiabatic process may be viewed as equivalent. We also assume that Γ is constant.

In ALA, the density anomaly $\Delta\rho$ is determined by both temperature perturbation $T' = T - T_r$ and dynamic pressure p,

$$\Delta\rho = \rho_r[-\alpha(T - T_r) + \mathrm{K}_T^{-1} p] \ , \tag{2.3}$$

where T_r is the reference temperature and K_T is the isothermal bulk modulus. In our models, we make assumption that $\mathrm{K}_T \approx \mathrm{K}_S$, which simplifies the compressible mantle convection problem as discussed in Schubert *et al*. (2001).

With assumption of infinite Prandtl number, the conservation equations of mass, momentum and energy can be written as follows (Jarvis & McKenzie, 1980; Ita & King, 1994; Leng & Zhong, 2008a; King *et al*., 2010):

$$(\rho_r u_i)_{,i} = 0\,, \tag{2.4}$$

$$-p_{,j}\delta_{ij} + \tau_{ij,j} - \Delta\rho g\delta_{iz} = 0\,, \tag{2.5}$$

$$\rho_r c_P \dot{T} + \rho_r c_P u_i T_{,i} + \rho_r g\alpha T u_z = (kT_{,i})_{,i} + \tau_{ij}u_{i,j} + \rho_r H\,, \tag{2.6}$$

where u_i and T are velocity vector and temperature, τ is deviatoric stress tensor, $\dot{T}$ is the derivative of temperature with respect to time t, k is thermal conductivity, H is heat production rate; i and j are spatial indices and z means vertical direction, and δ_{ij} is the Kronecker delta function.

The deviatoric stress tensor τ_{ij} is determined by a rheology equation

$$\tau_{ij} = \eta\left(\frac{\partial u_i}{\partial x_j} + \frac{\partial u_j}{\partial x_i} - \frac{2}{3}\delta_{ij}\frac{\partial u_k}{\partial x_k}\right), \tag{2.7}$$

where η is the viscosity.

Equations (2.4)-(2.6) can be non-dimensionalized with the following characteristic values:

$$x_i = dx_i'\,,\ u_i = \frac{\kappa_0}{d}u_i'\,,\ T = \Delta T T' + T_s\,,\ T_s = \Delta T T_s'\,,\ \rho_r = \rho_0\rho_r'\,,\ t = \frac{d^2}{\kappa_0}t'\,,$$

$$H = \frac{H'\kappa_0\Delta T c_{P0}}{d^2}\,,\ \eta = \eta_0\eta'\,,\ p = \frac{\eta_0\kappa_0}{d^2}p'\,,\ \alpha = \alpha_0\alpha'\,,\ g = g_0 g'\,,\ c_P = c_{P0}c_P'\,,$$

$$\Gamma = \Gamma_0\Gamma'\,,\ k = k_0 k'\,, \tag{2.8}$$

where symbols with primes are dimensionless; symbols with a subscript 0 are surface values of corresponding parameters and are used as the reference to scale the dimensional variables; d is the mantle thickness, ΔT is the total temperature

difference across the layer, and T_s is the surface temperature which is taken as 273K in this study; κ_0 is the reference thermal diffusivity and is defined as $\kappa_0 = k_0/(\rho_0 c_{P0})$.

After dropping the primes, the dimensionless governing equations for ALA are as follows (e.g., Leng & Zhong, 2008a):

$$(\rho_r u_i)_{,i} = 0\,, \tag{2.9}$$

$$-p_{,j}\delta_{ij} + \tau_{ij,j} + [\rho_r \alpha g Ra(T - T_r) - \frac{\alpha g}{c_P \Gamma} p\gamma]\delta_{iz} = 0\,, \tag{2.10}$$

$$\rho_r c_P \dot{T} + \rho_r c_P u_i T_{,i} + \rho_r Di \alpha g u_z (T + T_s) = (kT_{,i})_{,i} + \frac{Di}{Ra}\tau_{ij}u_{i,j} + \rho_r H\,, \tag{2.11}$$

where *Ra* is the Rayleigh number, *Di* is the dissipation number, and γ is the mantle compressibility. They are defined as:

$$Ra = \frac{{\rho_0}^2 c_{P0}\alpha_0 g_0 \Delta T d^3}{k_0 \eta_0}\,, \tag{2.12}$$

$$Di = \frac{\alpha_0 g_0 d}{c_{P0}}\,, \tag{2.13}$$

$$\gamma = \frac{Di}{\Gamma_0}\,. \tag{2.14}$$

In our model, Γ_0 is taken as 1, therefore, $Di = \gamma$. The dimensionless surface temperature T_s is fixed as 0.091 and the heat production rate *H* in equation (2.11) is zero. The non-dimensional values of Γ, α, *k*, *g*, and c_P are all 1 in equations (2.9)-(2.11) unless otherwise indicated.

The dimensionless Adams-Williamson equation is

$$\frac{1}{\rho_r}\frac{\mathrm{d}\rho_r}{\mathrm{dz}} = -\frac{\alpha g}{c_p \Gamma}\gamma\,. \tag{2.15}$$

With $\alpha g/(c_P\Gamma) = 1$ and $Di = \gamma$, the dimensionless reference density profile is

$$\rho_r(\mathrm{z}) = \rho_0 e^{Di(1-z)}\,. \tag{2.16}$$

We consider 2D Cartesian models within a box of non-dimensional height of 1 and length L. The top and bottom boundaries are set as $z = 1$ and $z = 0$, respectively. We use free-slip boundaries with zero normal velocities and tangential stresses at the four boundaries of the box. The non-dimensional temperature is fixed at 0 and 1 on the top and bottom boundaries, respectively, and the sidewalls are thermally insulated.

Two different analyses are presented in this study: the marginal stability analysis and the finite amplitude convection calculations. We use the finite element code developed by Leng & Zhong (2008a) for numerical experiments of compressible mantle convection. This code is based on incompressible mantle convection code Citcom (Moresi *et al*., 1996) and has been benchmarked (Leng & Zhong, 2008a; King *et al*., 2010).

2.3. Marginal Linear Stability Analysis Using Propagator Matrix Method

Rayleigh number, *Ra*, is an important non-dimensional number that determines the vigor of convection. Convection occurs when *Ra* exceeds a critical value Ra_c. Marginal linear stability analysis can be used to study the onset of mantle convection and to determine Ra_c (e.g., Jeffreys, 1930; Turcotte & Schubert, 2002). Classic analyses using a stream-function formulation have been used to determine Ra_c for incompressible fluid with uniform thermodynamic parameters and the same boundary conditions as our models (e.g., Turcotte & Schubert, 2002) and Ra_c is:

$$Ra_c = \frac{(\pi^2 + k_x^2)^3}{k_x^2}, \tag{2.17}$$

where k_x is the wave-number of horizontal perturbation.

For compressible convection with depth-dependent density and possibly other depth-dependent thermodynamic properties, propagator matrix method is more effective. The propagator matrix method has been used to obtain analytic solution of the Stokes flow problem for incompressible (Hager & O'Connell, 1981) and compressible (Leng & Zhong, 2008a) models. With a stream-function and vorticity formulation, Jarvis & McKenzie (1980) employed the propagator matrix method for marginal stability analysis with heat flux boundary conditions. Buffett, Gable, & O'Connell (1994) used the propagator matrix method for marginal stability analysis for incompressible flows with depth-dependent viscosity. In this study we develop a new implementation of propagator matrix method for marginal stability analysis for both incompressible and compressible flows with free-slip and isothermal boundary conditions. Our implementation is based on a stress-velocity formulation which is similar to that in Leng & Zhong (2008a), but we also incorporate the linearized energy equation. The set-up of propagator matrix and the solution procedure are discussed in Appendix A. In the following sections we will outline the basic principles of marginal stability analysis and present the critical Rayleigh number of compressible convection as well as the corresponding eigenfunctions solved by the propagator matrix method.

2.3.1. Linearized Governing Equations

Marginal linear stability analysis is performed in the limit of weak convection, in which the governing equations can be linearized around a background state (Turcotte & Shubert, 2002). For basal heating convection with a fixed temperature of 1 at the bottom and 0 at the top, and with constant thermal conductivity, the reference temperature is set to be $T_r = 1 - z$, i.e., purely conductive temperature. Introduce a small perturbation T' into reference temperature, such that $T = T_r + T'$, and the

perturbed temperature leads to non-zero horizontal and vertical velocities u' and v', as well as non-zero shear and normal stresses τ' and σ'.

Since T', u', v', τ' and σ' are all of small magnitude, the governing equations (2.9)-(2.11) can be linearized as follows:

$$\left(\rho_r u_i'\right)_{,i} = 0\,, \tag{2.18}$$

$$-p_{,j}\delta_{ij} + \tau'_{ij,j} + (\rho_r \alpha g Ra T' - \frac{\alpha g}{c_P \Gamma} pDi)\delta_{i3} = 0\,, \tag{2.19}$$

$$\rho_r c_P \dot{T}' - \rho_r c_P v' + \rho_r \alpha g v' Di(1 - z + T_s) = k\nabla^2 T'\,. \tag{2.20}$$

The dependences of the perturbations on *x* and *z* are separable. The horizontal and vertical components of the perturbations are represented by sinusoidal functions and arbitrary functions, respectively. Take the temperature perturbation T' as an example, T' can be expressed in Fourier transform as

$$T' = \int T_0(z)\sin(\mathrm{k}_x x)e^{\alpha' t}\mathrm{d}\mathrm{k}_x\,, \tag{2.21}$$

where k_x is the wave-number of the horizontal component of temperature perturbation, $T_0(z)$ is the vertical dependence of the temperature perturbation, and α' is the growth rate and is taken as a real number. Notice that both $T_0(z)$ and α' in equation (2.21) are corresponding to k_x. Perturbations should satisfy the boundary conditions. The isothermal boundary condition in our model requires that $T'(z=0) = T'(z=1) = 0$ and $T_0(z)$ in equation (2.21) should be 0 at z=0 and z=1. The critical Rayleigh number, Ra_c, is determined as the value of Ra at $\alpha' = 0$. $T_0(z)$ at $\alpha' = 0$ is the eigenfunction of temperature perturbation for corresponding Ra_c, i.e., the corresponding k_x and Di.

The other four perturbations, u', v', τ' and σ', are expressed in similar forms to that of T' in Appendix A. The vertical dependences of u', v', τ' and σ' are denoted as $U(z)$, $V(z)$, $Y_{xz}(z)$ and $S_{zz}(z)$, respectively.

In Appendix A, we discuss that with a stress-velocity formulation, the linearized governing equations (2.18) - (2.20) for a compressible fluid can be written as a vector linear differential equation:

$$\frac{\mathrm{dW}}{\mathrm{dz}} = \mathrm{AW}\,, \tag{2.22}$$

where A is a 6×6 matrix consisting of *Ra*, *Di*, k_x, and other parameters, and W is a 6×1 vector:

$$\mathrm{W} = \left(V, U, \frac{S_{zz}}{2\mathrm{k}_x}, \frac{Y_{xz}}{2\mathrm{k}_x}, T_0, \frac{\mathrm{d}T_0}{\mathrm{dz}} \right)^{\mathrm{T}}\,, \tag{2.23}$$

where superscript T denotes matrix transpose.

The solution approach to equation (2.22) using the propagator matrix method and calculations of critical Rayleigh number and the corresponding eigenfunctions are described in Appendix A.

This implementation of propagator matrix method is general and can be used for marginal stability analysis for both incompressible and compressible media with either homogeneous or depth-dependent thermodynamic and material properties such as thermal conductivity or viscosity.

2.3.2. Results for Ra_c and eigenfunctions

We first show calculations of Ra_c for incompressible (Di=0) and homogeneous fluid at fundamental mode n=0 from our method. Here mode n represents the number of internal nodes of the vertical velocity eigenfunction, $V(z)$ (i.e., the first mode or n=1 mode has one $V(z)$=0 node, and thus two cells in the vertical direction). We use

129 uniform grid points in *z* direction to compute propagator matrix for all the results shown in this study. Figure 2.1a shows Ra_c for different wave-numbers k_x and the results are identical to those from classic analysis given by equation (2.17).

For compressible fluid, Ra_c at fundamental mode n=0 and first mode n=1 are determined and given in Table 2.1 and Figures 2.1b and 2.1c. We determined Ra_c at n=0 mode for *Di*=0, 0.5, 1, and 1.5, and k_x from 0.1π to 3π. We found that n=0 mode does not exist for large *Di*. For example, for $k_x=0.5\pi$, π, and 2π, the maximum *Di* with which n=0 mode exists is 1.9, 1.8, and 1.7, respectively. We also determined Ra_c at n=1 mode for *Di* = 0, 0.5, 1, and 2, and k_x varying from 0.5π to 2π. Ra_c for n=1 mode is much larger than that for n=0 mode. It is expected that *n*=1 mode does not exist for even larger *Di* (e.g., Jarvis and McKenzie, 1981), but we did not explore this topic further.

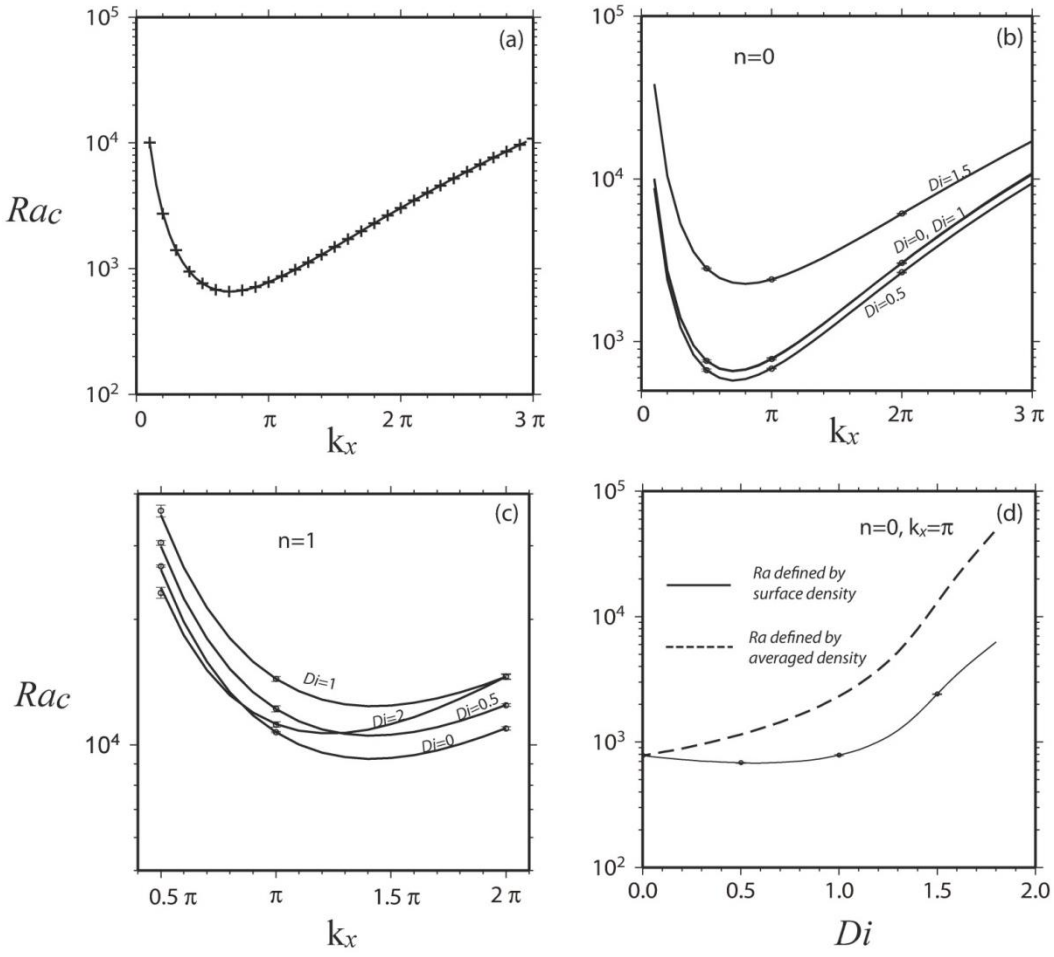

Figure 2.1. (a) critical Rayleigh number Ra_c versus wave-number k_x for incompressible fluid with uniform thermodynamic parameters and fixed temperature boundary conditions. The '+' symbols represent Ra_c from propagator matrix method and the line represents Ra_c from equation (2.17). (b) and (c): Ra_c versus k_x for compressible fluid with uniform thermodynamic parameters at (b) fundamental mode n=0 and for different *Di*; (c) first higher mode n=1 and for different *Di*. (d) Ra_c versus *Di* at $k_x = \pi$ for n=0. In (b),(c), and (d), the lines are Ra_c (defined by surface density) from the marginal stability analysis, and the circles are those from numerical experiments with error bars (Table 2.1). In (d), the dashed line represents Ra_c defined by depth-averaged density.

Table 2.1. Critical Rayleigh number computed by propagator matrix method (analytical) and finite element modeling (numerical).

Mode n	Wave number k_x (π)	*Di*	Ra_c (analytical)	averaged Ra_c (numerical)	Error
0	0.5	0	761	760	± 0.8%
0	0.5	0.5	667	667	± 0.7%
0	0.5	1	761	760	± 0.8%
0	0.5	1.5	2812	2812	± 0.5%
0	1	0	779	779	± 0.8%
0	1	0.5	683	683	± 0.4%
0	1	1	785	785	± 0.6%
0	1	1.5	2408	2408	± 0.5%
0	2	0	3044	3045	± 0.2%
0	2	0.5	2652	2645	± 0.5%
0	2	1	3035	3035	± 0.3%
0	2	1.5	6101	6100	± 0.3%
1	0.5	0	29910	30500	± 0.7%
1	0.5	0.5	26321	26825	± 0.3%
1	0.5	1	35533	36400	± 1.6%
1	0.5	2	23775	23150	± 1.5%
1	1	0	12176	12200	± 0.8%
1	1	0.5	10714	10725	± 0.2%
1	1	1	14394	14400	± 0.7%
1	1	2	11215	11180	± 0.7%
1	2	0	12468	12450	± 0.4%
1	2	0.5	10963	10950	± 0.5%
1	2	1	14557	14550	± 0.7%
1	2	2	14572	14600	± 0.7%

Ra_c would increase monotonically with *Di* (Figure 2.1d). Ra_c shows similar *Di* dependences for wave-numbers $k_x=0.5\pi$ and $k_x=2\pi$ at fundamental mode (Table 2.1). For n=1 mode, Ra_c increases with *Di* for *Di* varying from 0 to 1 (Figure 2.1c). While for n=0 mode, the wave-number k_x at which Ra_c is minimum is about $\sqrt{2}\pi/2$ for $Di \le 1$, this critical wave-number increases with *Di* (Figure 2.1b), suggesting that smaller convective wavelength is favored for larger *Di*.

The eigenfunctions $T_0(z)$, $U(z)$ and $V(z)$ are shown in Figure 2.2. It is found that compressibility, or *Di*, has a significant effect on these eigenfunctions (Figures 2.2a and 2.2b). For $Di = 0$, $T_0(z)$, $U(z)$ and $V(z)$ are purely sinusoidal functions (Figure 2.2, plotted in dashed lines as references for other cases). For $Di = 1$, $T_0(z)$, $U(z)$ and $V(z)$ are similar to sinusoidal functions, but are distorted to have larger amplitudes at shallow depths (or $z > 0.5$) than sinusoidal functions (Figure 2.2a). For $Di = 2$, the fundamental mode does not exist, and eigenfunctions of n=1 mode is plotted. It can be seen that $T_0(z)$, $U(z)$ and $V(z)$ differ significantly from sinusoidal functions with flow velocity much stronger at the shallow depths (Figure 2b). Eigenfunctions are also influenced by depth-dependent thermodynamic parameters (Figures 2c-2d).

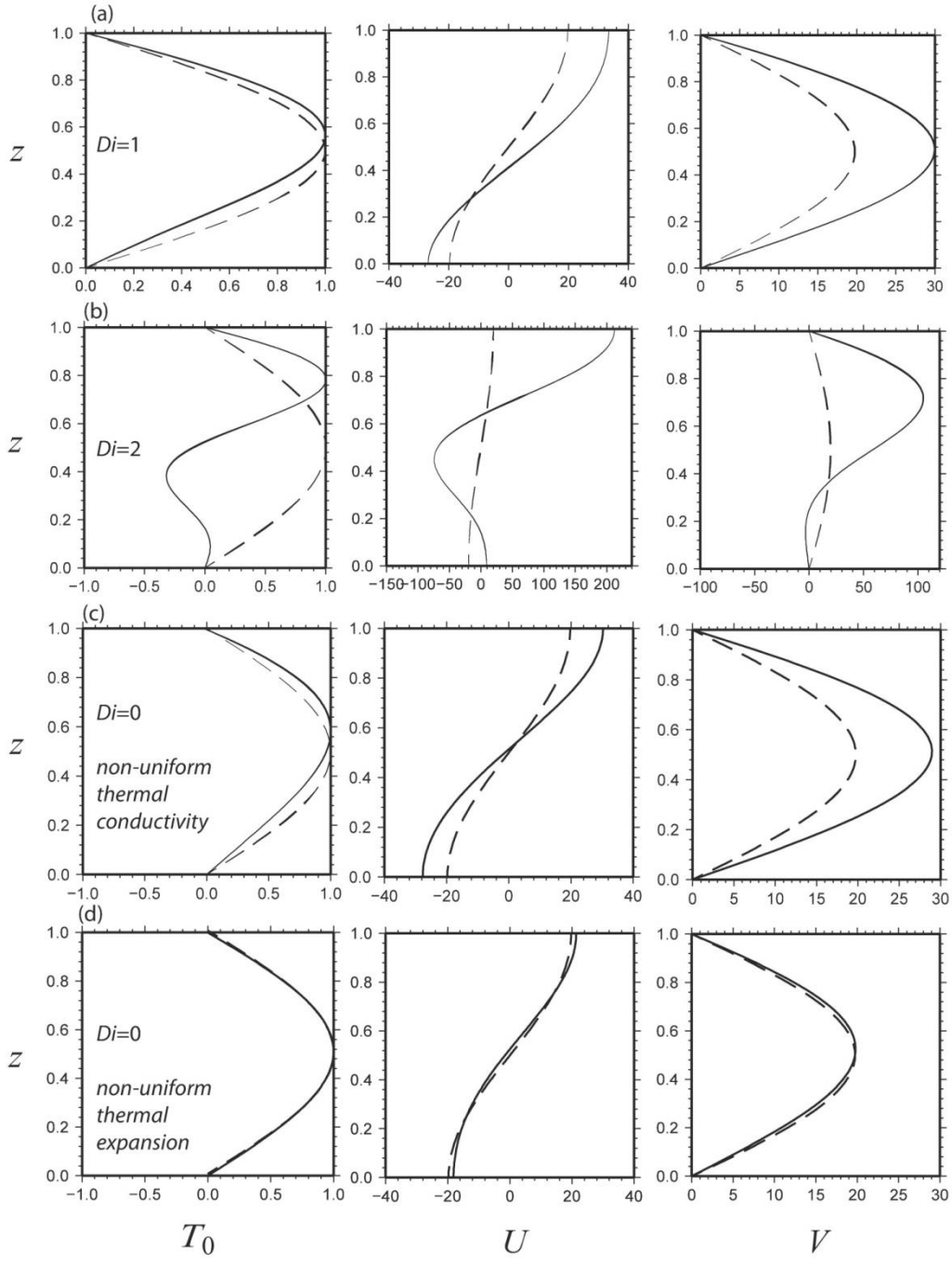

Figure 2.2. The solid lines are eigenfunctions of temperature (left panel), horizontal velocity (middle panel), and vertical velocity (right panel) for models with non-uniform properties: (a) *Di* = 1; (b) *Di* = 2; (c) non-uniform thermal conductivity that increases linearly from 1 at the top to 2 at the bottom, *Di*=0; (d) non-uniform thermal expansion that decreases linearly from 1 at the top to 0.2 at the bottom, *Di*=0. The dashed lines in those figures are the corresponding eigenfunctions for a case with *Di*=0 and homogeneous fluid and are sinusoidal functions.

Ra_c is also determined from numerical experiments for k_x=0.5π, π and 2π, with Di=0, 0.5, 1, 1.5 for the fundamental mode, and Di=0, 0.5, 1, 1.5, and 2 for the first mode, using the finite element code for compressible convection (Leng & Zhong, 2008a). We determine the critical Rayleigh number numerically by searching for a Rayleigh number at which the kinetic energy E_k remains constant with time for a given initial perturbation in temperature (Zhong & Gurnis, 1993). The initial perturbation is given as

$$T' = cT_0(z)\cos(k_x x), \tag{2.24}$$

where c is a small number (e.g., 10^{-2}), and $T_0(z)$ is the corresponding eigenfunction determined from the marginal stability analysis for the given Di and k_x as discussed earlier. The kinetic energy E_k of the flow from the numerical models is defined as:

$$E_k = \int_S (u^2 + v^2) dS, \tag{2.25}$$

where the integration domain S represents the whole flow field in the 2D model. For the given Di and k_x, we calculate E_k for the first 200 time steps and adjust Ra in the model until E_k neither increases nor decays with time (Figure 2.3 for E_k versus time for two example cases). The resulting Ra is the critical Rayleigh number where the growth rate is 0 (e.g., Zhong & Gurnis, 1993).

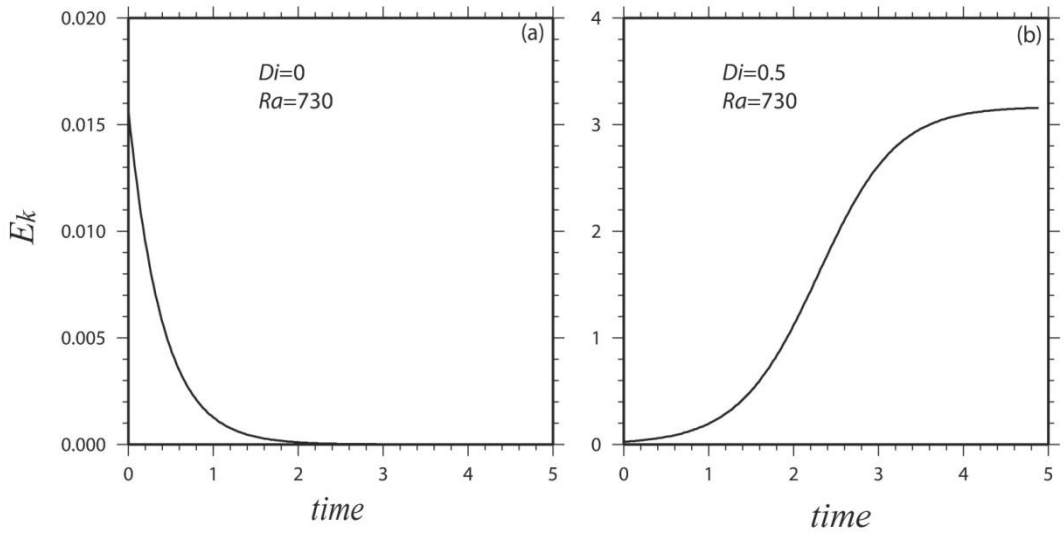

Figure 2.3. Kinetic energy E_k versus time from numerical calculations using Citcom with $k_x=\pi$, Ra = 730 and (a) Di=0; (b) Di=0.5. The critical Rayleigh number Ra_c computed from propagator matrix method for these two cases are 779 and 683, respectively. These two calculations show that E_k increases/decreases with time when Ra is greater/less than Ra_c. These two cases were computed for 40,000 time steps (elapsed time ~ 5) to reach nearly steady states. For calculations numerically determining Ra_c, models are often computed for 200 time steps.

Our finite element models use the same model parameters and boundary conditions as those for linear stability analysis. The models use $n_x \times n_z = 129 \times 129$, and 65×129 grid points for $k_x=0.5\pi$, π, and 2π, respectively (i.e., the aspect ratio of the box is 2, 1 and 0.5, respectively). Such numerically determined Ra_c for different Di and k_x are in excellent agreement with those from our propagator matrix method with relative difference of less than 1% (Figures 2.1b~2.1d, and Table 2.1), providing confirmation for both our propagator matrix method and the finite element method for determining Ra_c.

We make two remarks about the eigenfunctions. First, it is well known that for incompressible (Di=0) and homogeneous fluid, the eigenfunctions are sinusoidal

functions (e.g., Turcotte & Schubert, 2002). We showed that the eigenfunctions are no longer sinusoidal functions for compressible fluid with $Di \neq 0$ and depth-dependent density (Figures 2.2a and 2.2b). Even for incompressible fluid with Di=0, depth-dependent thermal conductivity or thermal expansion also leads to non-sinusoidal forms of eigenfunctions (Figures 2.2c and 2.2d). Second, it is important to use the eigenfunctions of $T_0(z)$ in equation (2.24) to determine Ra_c numerically. Although numerical methods have been used to determine Ra_c (e.g., Zhong & Gurnis, 1993), it has not been explicitly demonstrated that the eigenfunctions of $T_0(z)$ are needed as initial temperature perturbations. We found that for $Di \neq 0$, if $\sin(\pi z)$ rather than eigenfunction of $T_0(z)$ is used for the initial perturbations, the kinetic energy E_k does not vary monotonically with time and Ra_c cannot be determined accurately.

2.4. Finite Amplitude Convection

We computed 2D Cartesian models of compressible mantle convection at different Ra and Di (Table 2.2) using a finite element code (Leng & Zhong, 2008a). In this study of finite amplitude convection, the models are all 1×1 boxes. All the cases are for basal heating convection with no internal heating. The calculations are done with adequate resolution that produces less than 3% discrepancy between top and bottom heat flux for most cases (Table 2.2). For all cases, there are at least three elements across a thermal boundary layer (TBL). For most cases with relatively low Ra, calculations start from initial temperature perturbation as in equation (2.24). But for cases with high Ra, we choose steady state temperature field from calculations with either lower resolution or lower Ra as initial conditions. The calculations are run until steady states, or quasi-steady states are attained when averaged heat flux does not change with time (Figure 2.4). Compressible convection is more time-dependent

in general, as discussed in King *et al*. (2010). In our analysis for cases which reach quasi-steady state, time-averaged values of heat flux and TBL properties are used.

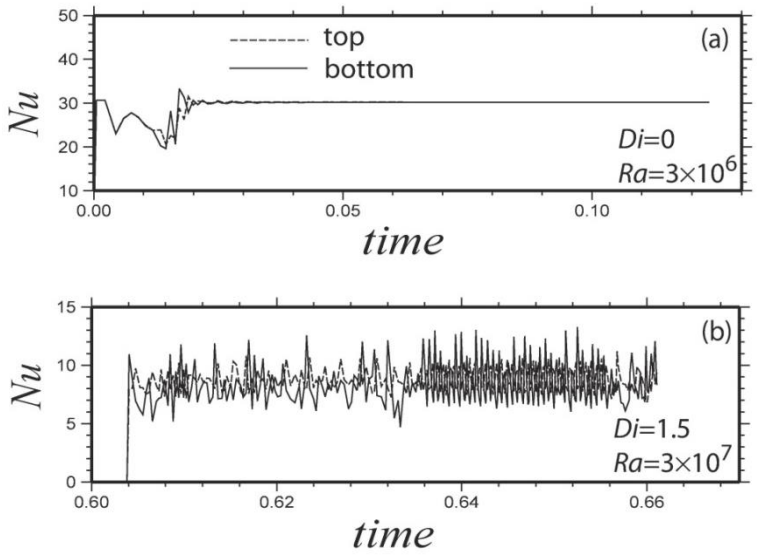

Figure 2.4. Nusselt number *Nu* versus elapsed time *t* for cases (a) AC0036, with *Di*=0, $Ra=3\times10^6$; (b) AC1537, with *Di*=1.5, $Ra=3\times10^7$. AC0036 reaches the steady state at *t*=0.04. AC1537 reaches the quasi-steady state at about *t*=0.64. Solid and dashed lines are Nusselt number at the bottom and top boundaries, respectively.

Table 2.2. Calculations for 2D Cartesian compressible convection.

Case	*Di*	*Ra*	I.C.	Steps (10^4)	Grid	ΔNu(%)	*Nu*	ε_{Nu}	V_t	V_b
NC0013	0	10^3	0	2	65×65	0.002	1.47	0	4.43	4.43
NC0033	0	3×10^3	0	2	65×65	0.001	3.10	0	16.59	16.59
NC0053	0	5×10^3	0	2	65×65	0.001	3.81	0	24.90	24.90
NC0014	0	10^4	0	2	65×65	0.003	4.89	0	41.47	41.47
AC0034	0	3×10^4	0	2	65×65	0.002	7.09	0	88.61	88.62
AC0015	0	10^5	0	4	65×65	0.002	10.5	0	197.8	197.8
AC0035	0	3×10^5	AC0015	6	65×65	0.009	14.9	0	406.3	406.4
AC0016	0	10^6	0	6	65×65	0.003	21.7	0	882.9	882.9
AC0036	0	3×10^6	0	6	65×65	0.007	30.2	0	1789	1788
AC0017	0	10^7	*	12	129×129	0.112	44.7	0	3867	3863
AC0037	0	3×10^7	AC0017	18	257×257	0.938	61.9	0.28	7326	7388
NC0513	0.5	10^3	0	5	65×65	0.035	1.49	0	4.58	4.37
NC0533	0.5	3×10^3	0	2	65×65	0.035	2.58	0	14.31	14.02
NC0553	0.5	5×10^3	0	5	65×65	0.043	3.07	0	21.23	20.83
NC0514	0.5	10^4	0	5	65×65	0.043	3.82	0	35.05	34.37
NC0534	0.5	3×10^4	0	5	65×65	0.015	5.33	0	74.25	72.40
NC0564	0.5	6×10^4	0	4	65×65	0.005	6.54	0	117.0	113.3
NC0515	0.5	10^5	0	3	65×65	0.032	7.55	0	161.5	155.1
AC0535	0.5	3×10^5	0	3	65×65	0.111	9.00	0	252.7	224.8
AC0565	0.5	6×10^5	*	8	129×129	4.534	11.3	1.60	341.1	307.1
AC0516	0.5	10^6	*	8	129×129	0.132	13.0	0.40	444.6	390.1
AC0536	0.5	3×10^6	*	8	129×129	4.789	17.2	1.52	529.9	464.2
AC0517	0.5	10^7	*	10	129×129	1.818	23.9	2.42	1077	864.6
AC0537	0.5	3×10^7	AC0517	10	129×129	3.249	32.6	3.07	2032	1442
NC1013	1	10^3	0	5	65×65	0.075	1.21	0	2.98	2.56
NC1033	1	3×10^3	0	5	65×65	0.072	1.82	0	10.04	9.32
NC1014	1	10^4	0	5	65×65	0.075	2.47	0	24.40	23.0
NC1034	1	3×10^4	0	5	65×65	0.101	3.19	0	50.00	46.7
NC1015	1	1×10^5	0	1	65×65	0.218	3.87	0	88.89	77.47
NC1035	1	3×10^5	*	8	129×129	4.14	4.82	0.82	129.3	111.6
NC1065	1	6×10^5	0	2.8	65×65	0.510	6.37	0	157.6	135.4
AC1016	1	10^6	0	5	65×65	0.078	6.87	0.20	192.4	166.5
AC1036	1	3×10^6	*	3	129×129	1.159	9.44	0.97	387.6	279.3

AC1017	1	10^7	*	10	129×129	2.473	13.7	1.80	798.3	503.1
AC1037	1	3×10^7	AC1037	10	129×129	4.646	18.9	2.14	1533	848.1
NC1533	1.5	3×10^3	0	5	65×65	0.148	1.11	0	3.99	2.08
NC1514	1.5	10^4	0	5	65×65	0.064	1.31	0	10.31	6.52
NC1534	1.5	3×10^4	0	5	65×65	0.038	1.49	0	19.16	12.57
NC1515	1.5	10^5	0	2	65×65	0.443	2.00	0	30.29	24.00
NC1535	1.5	3×10^5	*	2.5	129×129	0.475	2.53	0	61.08	45.84
NC1516	1.5	10^6	*	3.5	129×129	0.713	3.31	0.13	126.5	81.67
AC1536	1.5	3×10^6	*	6	257×257	2.94	4.40	0.41	242.7	143.6
AC1517	1.5	10^7	*	10	257×257	2.12	6.27	0.71	539.0	270.9
AC1537	1.5	3×10^7	*	8	257×257	2.388	8.79	1.0	1075.2	472.6
AC1518	1.5	10^8	AC1537	8	257×257	5.298	12.27	1.52	2108.2	799.1
NC2034	2	3×10^4	0	3	65×65	0.018	1.10	0	9.06	0.51
NC2015	2	10^5	0	3	65×65	0.325	1.23	0	18.73	0.17
NC2035	2	3×10^5	0	5	65×65	0.700	1.33	0	34.63	0.20
NC2016	2	10^6	*	2	129×129	1.084	1.46	0	60.4	0.38
NC2036	2	3×10^6	*	8	257×257	-1.27	1.71	0.13	121.1	7.93
NC2017	2	10^7	*	6	257×257	-1.23	2.16	0.18	242.2	29.46
NC2037	2	3×10^7	*	10	385×385	1.645	2.79	0.33	456.3	92.84
AC2018	2	10^8	*	4	385×385	1.284	3.87	0.38	1020	228.1
AC2038	2	3×10^8	*	8	385×385	-1.72	5.24	0.50	1965	475.8
AC2019	2	10^9	*	7	385×385	5.2613	7.27	0.71	4454	971.5
AC2039	2	3×10^9	AC2019	10	385×385	6.7265	10.14	0.85	7209	1666

The first six columns are for case number, *Di*, *Ra*, initial condition, the number of time steps (in 10^4), and finite element grid, respectively. NC cases do not have vigorous enough convection, while AC cases have vigorous convection and are used in scaling analysis here. For the initial condition column (I.C.), '0' stands for default initial temperature condition (i.e., equation 2.24), '*' for that from its lower resolution case, and 'AC' for that from lower *Ra* case. *Nu* is for surface Nusselt number. ΔNu is the difference between the top and bottom *Nu* in percentage. ε_{Nu} is the standard deviation of surface *Nu* (0 for steady state, while nonzero ε_{Nu} is for quasi-steady state). V_t and V_b are the RMS velocity for the surface and bottom, respectively.

With no internal heating, Cartesian thermal convection for incompressible fluid (Di=0) display symmetric features for the TBLs. Top and bottom TBLs contain equal amount of buoyancy, so are the downwellings and upwellings (Figure 2.5a). Horizontally averaged RMS velocity for the top and bottom TBLs are identical, and the average temperature in the convective core is 0.5 (Figure 2.6a). The compressibility breaks the symmetry between the TBLs. For Di=1 cases, the top TBL has larger temperature difference and larger flow velocity than those for the bottom TBL, and consequently cold downwellings dominate heat transfer (Figures 2.5b and 2.6b). The adiabatic temperature gradient is also evident (Figures 2.6b~2.6d). These features are expected, as have been observed by Jarvis & McKenzie (1980). An increasing compressibility causes reduced flow velocity and larger lateral homogenous temperature, i.e., less vigorous convection (Figures 2.6a~2.6c), which leads to less efficient heat transfer (Figure 7 and Table 2.2). A larger Di also causes upwelling plumes to be much weaker than downwellings (Figure 2.5d). When Di=2, upwelling plumes can hardly be produced, even with a very large Ra (e.g., Figure 2.5d with Ra=3×10^9), because at large Di, the compressibility cools the upwelling plumes rapidly to diminish the plumes (Leng & Zhong, 2008a).

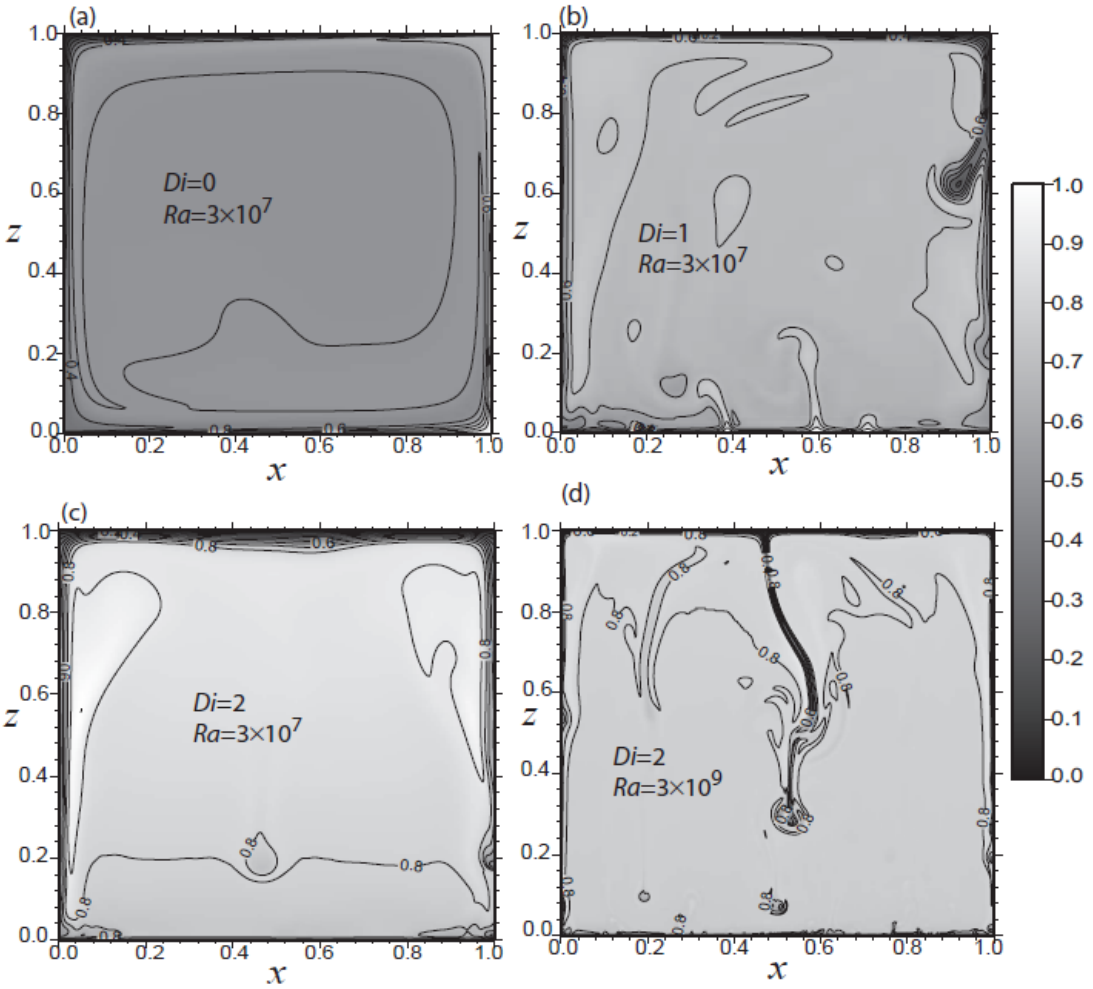

Figure 2.5. Contours and snapshots of representative temperature fields T for cases (a) AC0037, with Di=0, Ra=3×10^7, and normalized super-adiabatic temperature field θ, for cases (b) AC1037, with Di=1, Ra=3×10^7; (c) NC2037, with Di=2, Ra=3×10^7; (d) AC2039, with Di=2, Ra=3×10^9. The super-adiabatic temperature T_{sa} is computed by subtracting adiabatic temperature (for example as shown in Figure (B1)) from original temperature, and normalized super-adiabatic temperature $\theta=(T_{sa}-T_{sa}{}^{\min})/(T_{sa}{}^{\max}-T_{sa}^{\min})$, where $T_{sa}^{\max}$ and $T_{sa}^{\min}$ are the maximum and minimum of super-adiabatic temperature. $(T_{sa}^{\min},T_{sa}^{\max})$ for cases in (b), (c), (d) are (-0.2803, 0.1334), (-0.0713, 0.0127), and (-0.0584, 0.0174), respectively. All the cases have reached quasi-steady states.

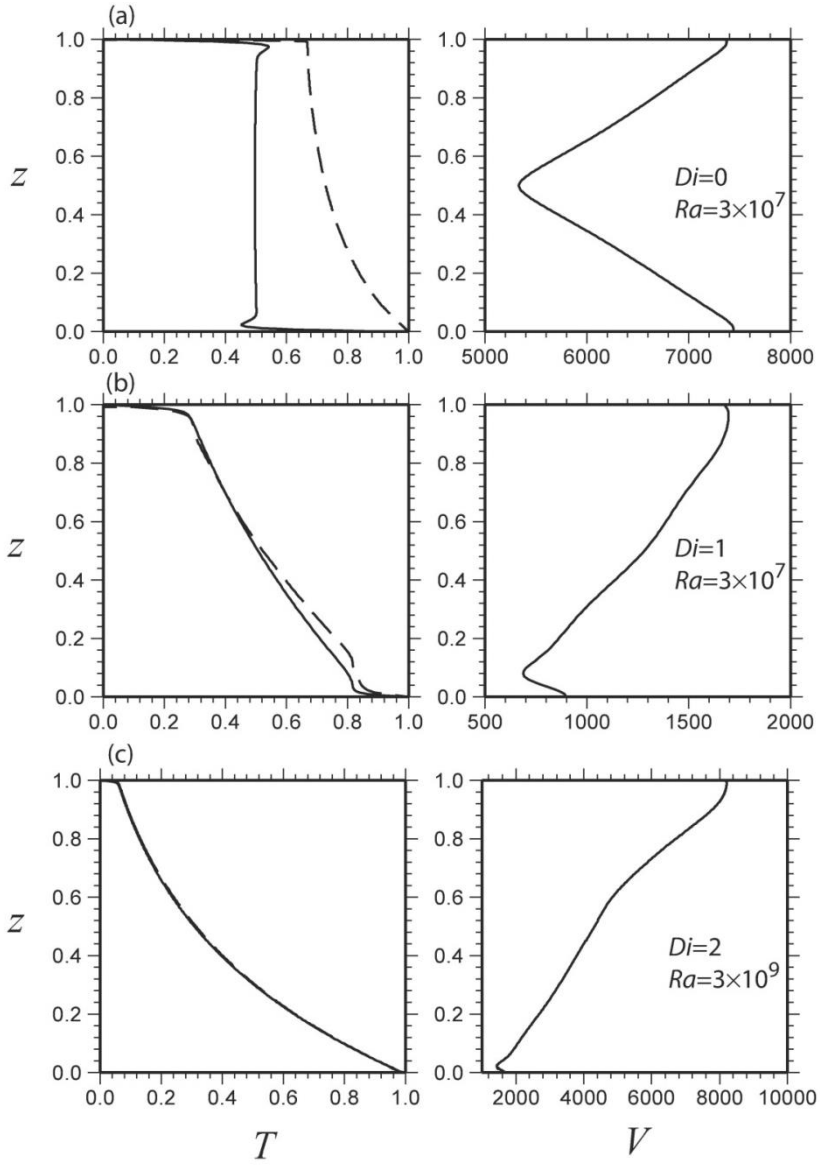

Figure 2.6. The solid lines are the horizontally averaged temperature (left panel) and RMS velocity (right panel) for cases (a) AC0037; (b) AC1037; (c) AC2039. The dashed lines in the temperature plots are the maximum temperature versus depth.

We computed cases with dissipation number Di = 0, 0.5, 1, 1.5, 2 and a large range of Ra (Table 2.2). The smallest Ra for each Di is generally slightly larger than the corresponding Ra_c. In the following subsections, we will first present numerical results, and then develop a scaling theory on how Di and Ra control TBL properties

and heat transfer. We will show that our theoretical analysis is consistent with the numerical results.

2.4.1. Numerical results of *Nu* and TBL properties

The Nusselt number is defined as the ratio of the heat flux through the convection system to the heat flux which would exist in a purely conductive state:

$$Nu = \frac{Q}{k\Delta T / d} = q, \tag{2.26}$$

where Q is the dimensional convective heat flux, $k\Delta T / d$ is dimensional heat flux in a purely conductive state, and q is the dimensionless heat flux, given how the equations are normalized in equation (2.8).

Figure 2.7 shows *Nu* versus *Ra* for all the cases. For a given *Di*, in general, *Nu* does not follow a straight line in the log-log plot at small *Ra*. This is because at relatively small *Ra*, the top and bottom TBLs have not been fully developed and separated. In the following analysis on *Nu* ~ *Ra* scaling, we choose cases with relatively large *Ra* (Table 2.3) that have developed vigorous convection and with *Nu* larger than 4. Those cases follow $Nu \sim Ra^{\alpha}$ and are along straight lines in Figure 2.7.

Table 2.3. TBL properties of finite amplitude convection cases

Cases	Di	Ra	ΔT_t	ΔT_b	δ_t	δ_b	Ra_t	Ra_b
AC0034	0	3×10^4	0.500	0.500	0.112	0.112	5.25	5.24
AC0015	0	10^5	0.495	0.495	0.075	0.075	5.19	5.19
AC0035	0	3×10^5	0.496	0.497	0.054	0.054	5.50	5.50
AC0016	0	10^6	0.497	0.497	0.038	0.038	5.94	5.94
AC0036	0	3×10^6	0.500	0.500	0.028	0.028	6.80	6.79
AC0017	0	10^7	0.497	0.496	0.019	0.019	6.80	6.76
AC0037	0	3×10^7	0.485	0.500	0.014	0.014	7.03	7.95
AC0535	0.5	3×10^5	0.409	0.305	0.072	0.056	11.5	9.16
AC0565	0.5	6×10^5	0.404	0.291	0.059	0.045	11.9	7.33
AC0516	0.5	10^6	0.389	0.296	0.047	0.037	10.4	9.08
AC0536	0.5	3×10^6	0.389	0.291	0.036	0.029	13.4	11.0
AC0517	0.5	10^7	0.381	0.293	0.026	0.021	15.6	14.4
AC0537	0.5	3×10^7	0.378	0.298	0.019	0.016	17.8	18.4
AC1016	1	10^6	0.269	0.168	0.061	0.038	16.1	16.9
AC1036	1	3×10^6	0.262	0.158	0.044	0.026	16.9	15.6
AC1017	1	10^7	0.255	0.156	0.030	0.019	16.7	16.4
AC1037	1	3×10^7	0.251	0.156	0.022	0.014	17.8	19.1
AC1536	1.5	3×10^6	0.154	0.073	0.053	0.023	19.6	19.1
AC1517	1.5	10^7	0.146	0.063	0.036	0.014	18.4	12.5
AC1537	1.5	3×10^7	0.140	0.063	0.025	0.011	17.2	13.5
AC1518	1.5	10^8	0.137	0.062	0.018	0.008	19.1	15.6
AC2018	2	10^8	0.059	0.023	0.023	0.007	21.2	26.6
AC2038	2	3×10^8	0.056	0.024	0.017	0.006	20.8	34.4
AC2019	2	10^9	0.054	0.022	0.012	0.004	22.1	35.3
AC2039	2	3×10^9	0.053	0.020	0.008	0.003	22.6	24.3

ΔT_t and ΔT_b are temperature differences across the top and bottom TBLs, respectively. δ_t and δ_b are thicknesses of the top and bottom TBLs, respectively. Ra_t and Ra_b are local Rayleigh numbers of the top and bottom TBLs, respectively.

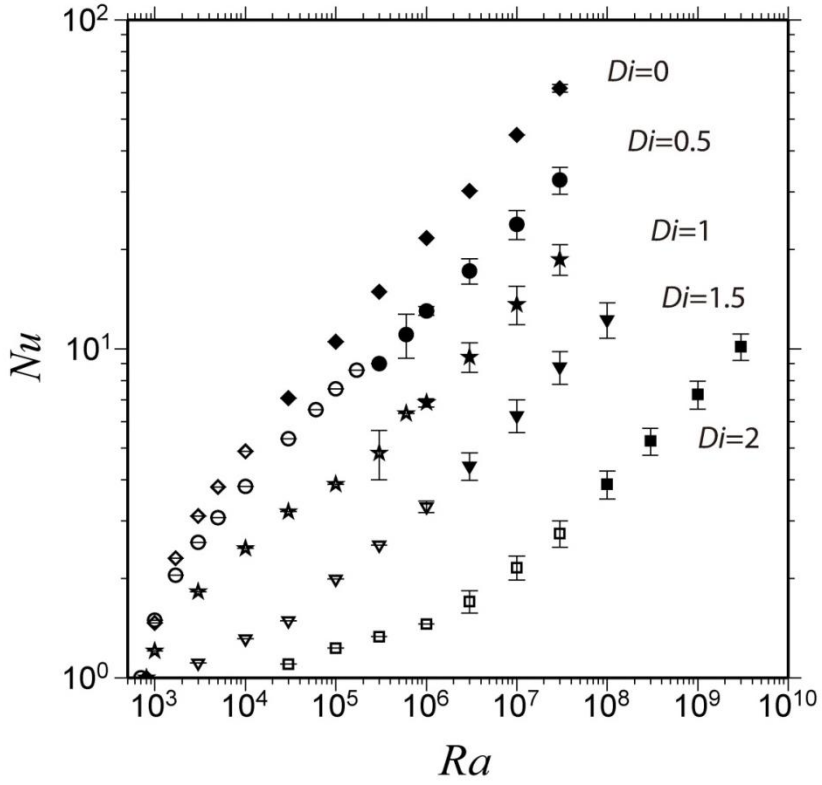

Figure 2.7. *Nu* versus *Ra* in log-log plot for 2D compressible convection with different *Di*. The symbols diamond, circle, star, triangle, and square are for cases with *Di* = 0, 0.5, 1, 1.5, and 2, respectively. The cases along the straight lines with filled symbols have developed vigorous convection and are used in the scaling analyses (Table 2.3). When applicable, error bars represent standard deviations.

Convective heat transfer is controlled by TBL properties. We quantified the thickness δ_l and temperature difference ΔT_l of the top and bottom TBLs from numerical models. The methods for quantifying the TBL properties are described in Appendix B. For a given *Di*, both the top and bottom TBL thicknesses, δ_t and δ_b, decrease with *Ra* (Figure 2.8a). For incompressible convection (*Di*=0), δ_l scales as $\delta_l \sim Ra^{-0.30}$ from fitting our numerical results, which agrees with classic analysis, where $\delta_l \sim Ra^{-1/3}$

(e.g., McKenzie *et al*. 1974). TBL thicknesses δ_l for compressible convection cases show similar scaling with *Ra* to that for incompressible convection (Figure 2.8a). While for incompressible convection (*Di* = 0), δ_t and δ_b are identical, δ_t is larger than δ_b for compressible convection ($Di \neq 0$).

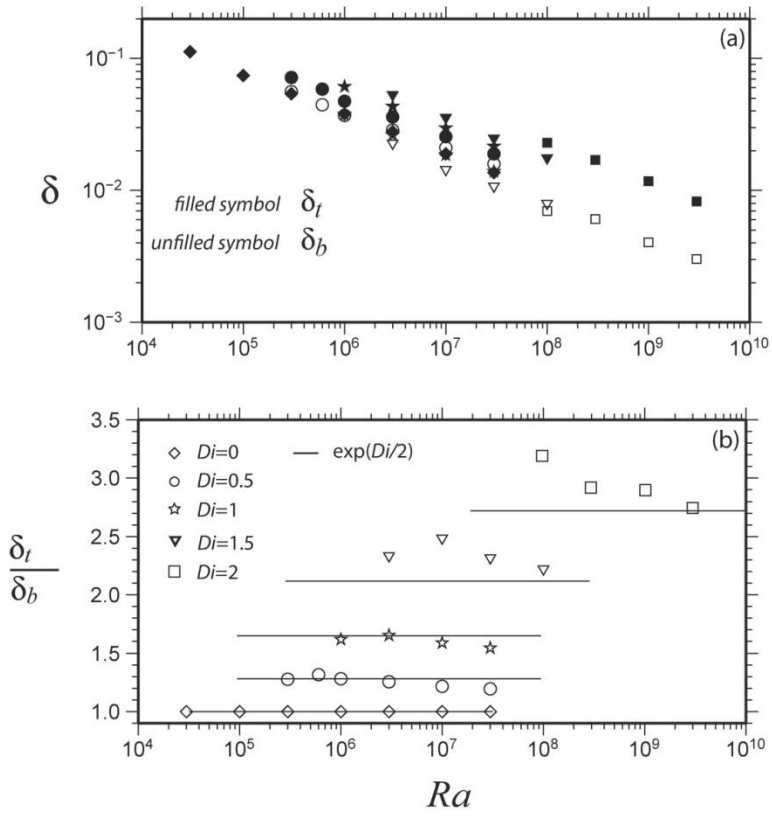

Figure 2.8. (a) Thicknesses of the top and bottom TBLs and (b) the ratio of top TBL thickness to bottom TBL thickness versus *Ra*. In both (a) and (b), the symbols diamond, circle, star, triangle, and square represent cases with *Di* = 0, 0.5, 1, 1.5, and 2, respectively. In (a), the filled symbols are for top TBL thickness and the unfilled ones are for bottom TBL thickness. In (b), the lines mark $e^{Di/2}$.

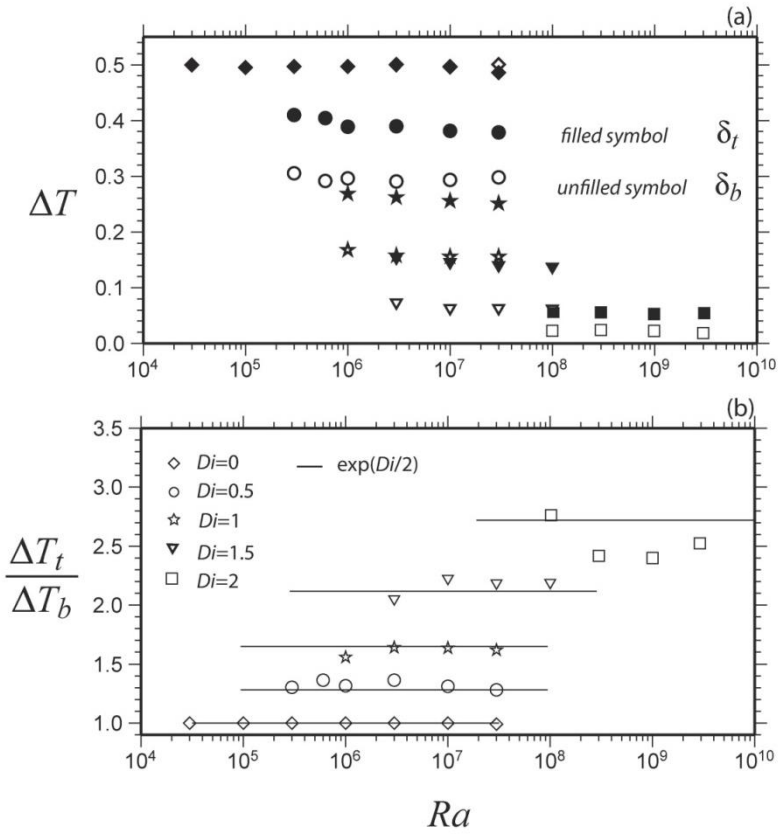

Figure 2.9. (a) Temperature differences across the top and bottom TBLs and (b) the ratio of temperature differences across the top TBL to that of the bottom TBL versus *Ra*. For both (a) and (b), the symbols diamond, circle, star, triangle, and square are for cases with *Di* = 0, 0.5, 1, 1.5, and 2, respectively. In (a), the filled symbols are for top TBL thickness and the unfilled ones are for bottom TBL thickness. In (b), the lines mark $e^{Di/2}$.

For *Di* = 0 cases, temperature difference of the top TBL, ΔT_t, is 0.5 and is identical with that of bottom TBL, ΔT_b (Figure 2.9a). For $Di \neq 0$ cases, ΔT_t is larger than ΔT_b. Both ΔT_t and ΔT_b are mainly controlled by *Di*, and decrease dramatically with *Di*. For a fixed *Di*, both ΔT_t and ΔT_b seem to decrease slightly with *Ra* (Figure 2.9a).

We may define a boundary layer Rayleigh number as

$$Ra_l = \frac{\rho_l^2 c_{Pl} g \alpha_l \Delta T_l \delta_l^3}{\eta_l k_l}, \tag{2.27}$$

where subscript *l* means the local value of corresponding parameters and *l* can be *t* and *b*, which represent the top and bottom TBLs, respectively. Notice that the density for each of the TBLs, ρ_l, is taken as that at the top of the TBL.

Ra_t and Ra_b can be defined and related to *Ra* as:

$$Ra_t = (\frac{\Delta T_t^*}{\Delta T^*})(\frac{\delta_t^*}{d})^3 Ra = \frac{\Delta T_t^4}{Nu^3} Ra, \tag{2.28}$$

$$Ra_b = e^{2Di(1-\delta_b)}(\frac{\Delta T_b^*}{\Delta T^*})(\frac{\delta_b^*}{d})^3 Ra = e^{2Di(1-\delta_b)} \frac{\Delta T_b^4}{Nu^3} Ra, \tag{2.29}$$

where the superscript * denotes dimensional values, and we considered $\rho = \rho_0 e^{Di(1-z)}$ from equation (2.16) and the following relations for pure basal heating convection,

$$Nu = (k\Delta T_t^* / \delta_t^*)/(k\Delta T^* / d) = (\Delta T_t^* / \Delta T^*)/(\delta_t^* / d) = \Delta T_t / \delta_t = \Delta T_b / \delta_b. \tag{2.30}$$

Ra_t and Ra_b calculated by (28) and (29) using numerical results of *Nu*, ΔT_t and ΔT_b are presented in Figure 2.10. Here we use *Nu*, ΔT_t and ΔT_b, but not TBL thicknesses δ_l, to determine TBL local *Ra*, because the latter are more difficult to quantify accurately. The most distinct feature of such determined local *Ra* is that for all the cases (Figure 2.10)

$$Ra_t = Ra_b. \tag{2.31}$$

It should not be noted that there are some scatterings in Figure 2.10 for Ra_t and Ra_b, especially for *Di*=2 cases that may be caused by resolution issues.

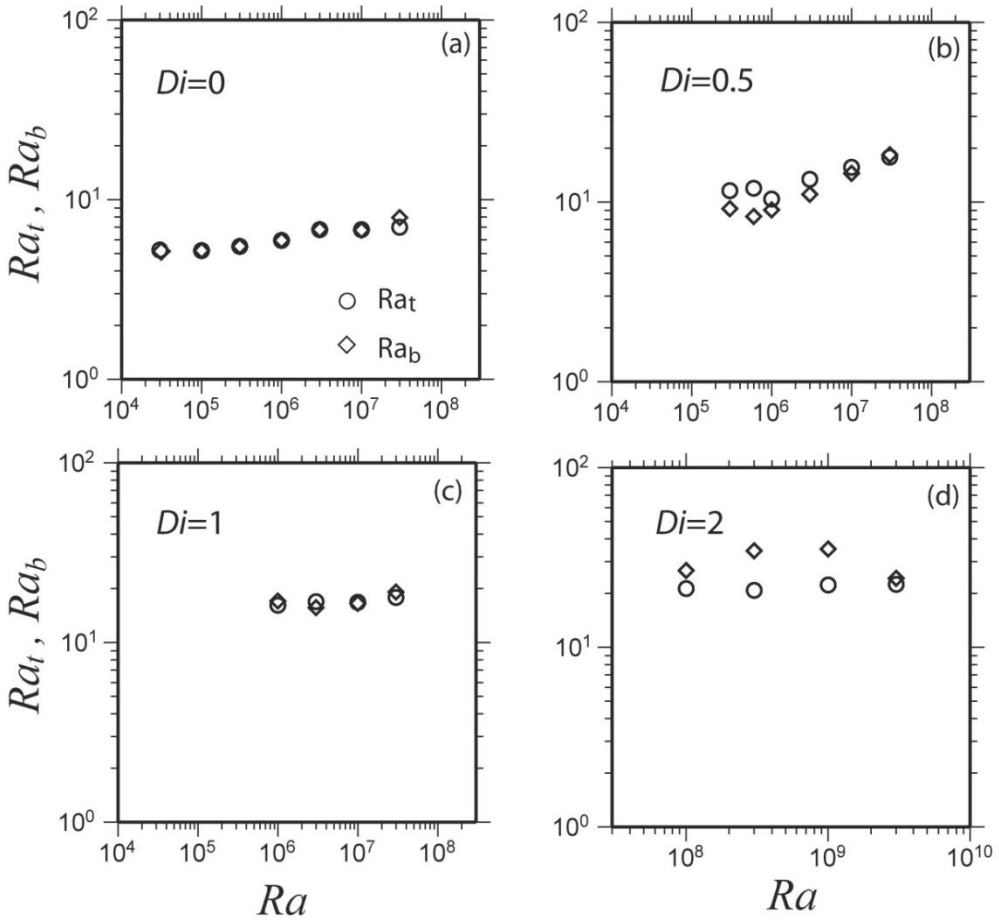

Figure 2.10. Boundary layer Raleigh numbers for the top and bottom TBLs versus *Ra* for cases with (a) *Di*=0; (b) *Di*=0.5; (c) *Di*=1; (d) *Di*=2. The circles and the diamonds represent the top and bottom TBLs, respectively.

2.4.2. Boundary layer analysis of heat transfer

Equation (2.28) can be written as:

$$Nu = (\Delta T_t)^{4/3}(\frac{Ra}{Ra_t})^{1/3}. \qquad (2.32)$$

The scaling $Nu \sim Ra^{1/3}$ is the same as that for isoviscous and incompressible convection (e.g., McKenzie *et al*., 1974; Moresi & Solomatov, 1995; Schubert *et al*.,

2001). While ΔT_t is a constant (e.g., ~0.5) for incompressible convection (*Di*=0), it depends strongly on *Di* for compressible convection ($Di \neq 0$) (Figure 2.9).

We take $Ra_t = Ra_b$ as our basic assumption in the following theoretical analysis. Combining (28) and (29), it is straightforward to obtain:

$$\frac{\Delta T_t}{\Delta T_b} = e^{Di(1-\delta_b)/2} \approx e^{Di/2}. \tag{2.33}$$

Since $Nu = \Delta T_t / \delta_t = \Delta T_b / \delta_b$ (i.e., equation 2.30), equation (2.33) leads to

$$\delta_t / \delta_b \approx e^{Di/2}. \tag{2.34}$$

Numerical results of $\Delta T_t / \Delta T_b$ and δ_t / δ_b for all the cases with different *Ra* and *Di* (Figures 2.8b and 2.9b) confirm equations (2.33) and (2.34).

Our numerical results suggest that ΔT_t and ΔT_b are mainly controlled by *Di*. Next we derive how ΔT_t and ΔT_b are scaled by *Di*. In finite amplitude compressible convection, an isentropic central region is produced (Jarvis & McKenzie, 1980). In the central region, the temperature in a non-dimensional form follows (e.g., Leng & Zhong, 2008a)

$$\frac{\mathrm{d}T_{ad}}{\mathrm{d}z} = -Di(T_{ad} + T_s), \tag{2.35}$$

where T_s is the non-dimensional surface temperature, T_{ad} is the adiabatic temperature, and the negative sign results from *z* pointing upwards. Super-adiabatic temperature, which drives convection, happens in the top and bottom TBLs. We divide the convective domain vertically into three parts: the top and bottom TBLs and the central core, over which temperature differences are represented by ΔT_t, ΔT_b and ΔT_{ad}, respectively. Let ΔT be the temperature across the whole convective system, and non-dimensional $\Delta T = 1$.

$$\Delta T = 1 = \Delta T_t + \Delta T_{ad} + \Delta T_b = \Delta T_t (1 + \frac{\Delta T_{ad}}{\Delta T_t} + \frac{\Delta T_b}{\Delta T_t}). \quad (2.36)$$

From equation (2.35), in the isentropic central area,

$$T_{ad} + T_s = Ae^{Di(1-z)}, \quad (2.37)$$

where *A* is a constant (e.g., Leng and Zhong, 2008a). At the base of the top TBL or $z = 1 - \delta_t$, the temperature is $T_{ad}(z = 1 - \delta_t) = \Delta T_t$, and from equation (2.37),

$$T_{ad}(z = 1 - \delta_t) + T_s = \Delta T_t + T_s = Ae^{Di\delta_t}. \quad (2.38)$$

Likewise, at the top of the bottom TBL or $z = \delta_b$, the temperature is $T_{ad}(z = \delta_b) = 1 - \Delta T_b$, and

$$T_{ad}(z = \delta_b) + T_s = 1 - \Delta T_b + T_s = Ae^{Di(1-\delta_b)}. \quad (2.39)$$

Combining equations (38) and (39) and defining $\Delta T_{ad} = T_{ad}(z = \delta_b) - T_{ad}(z = 1 - \delta_t)$, we get

$$\frac{\Delta T_{ad}}{\Delta T_t + T_s} = \frac{e^{Di(1-\delta_b)} - e^{Di\delta_t}}{e^{Di\delta_t}} = e^{Di(1-\delta_b-\delta_t)} - 1. \quad (2.40)$$

Substituting equations (40) and (33) into equation (36) leads to

$$1 = \Delta T_t [1 + \frac{(e^{Di(1-\delta_t-\delta_b)} - 1)(\Delta T_t + T_s)}{\Delta T_t} + e^{-Di/2}], \quad (2.41)$$

which can be written as

$$\Delta T_t = \frac{1 - T_s(e^{Di(1-\delta_t-\delta_b)} - 1)}{(e^{-Di/2} + e^{Di(1-\delta_t-\delta_b)})}. \quad (2.42)$$

From equation (42), ΔT_t is determined by both *Di* and TBL thickness $(\delta_t + \delta_b)$. As discussed before, TBL thickness δ scales with *Ra* following $\delta \sim Ra^{-1/3}$. Therefore, equation (2.42) suggests that ΔT_t is influenced by both *Di* and *Ra*. From numerical results, $(\delta_t + \delta_b)$ is of a smaller magnitude compared with 1, especially for

large *Ra* (Figure 2.8a), and may be ignored in equation (2.42) without introducing a large error. As a result, equation (2.42) may be approximated as:

$$\Delta T_t \approx \frac{1 - T_s(e^{Di} - 1)}{(e^{-Di/2} + e^{Di})}. \tag{2.43}$$

Equation (2.43) suggests that ΔT_t is mainly controlled by *Di* at large *Ra*, which agrees with numerical results (Figure 2.9a). Combining equations (2.33) and (2.43) leads to an expression for ΔT_b:

$$\Delta T_b \approx \frac{1 - T_s(e^{Di} - 1)}{(1 + e^{3Di/2})}. \tag{2.44}$$

Figure 2.11a shows the comparison between ΔT_t from equation (2.43) and those from numerical models for different *Di* and *Ra*. For a given *Di*, both ΔT_t from the largest *Ra* case and the averaged ΔT_t for all cases (Table 2.3) are plotted. ΔT_t from the numerical models agree well with that predicted from the theoretical analysis (equation 2.43) with <5% discrepancy, especially for cases with the largest *Ra*, and it is expected because equation (2.43) is a better approximation for large *Ra* cases. ΔT_b from numerical models for different *Di* and *Ra* show similarly good agreement with those predicted from equation (2.44) (Figure 2.11b).

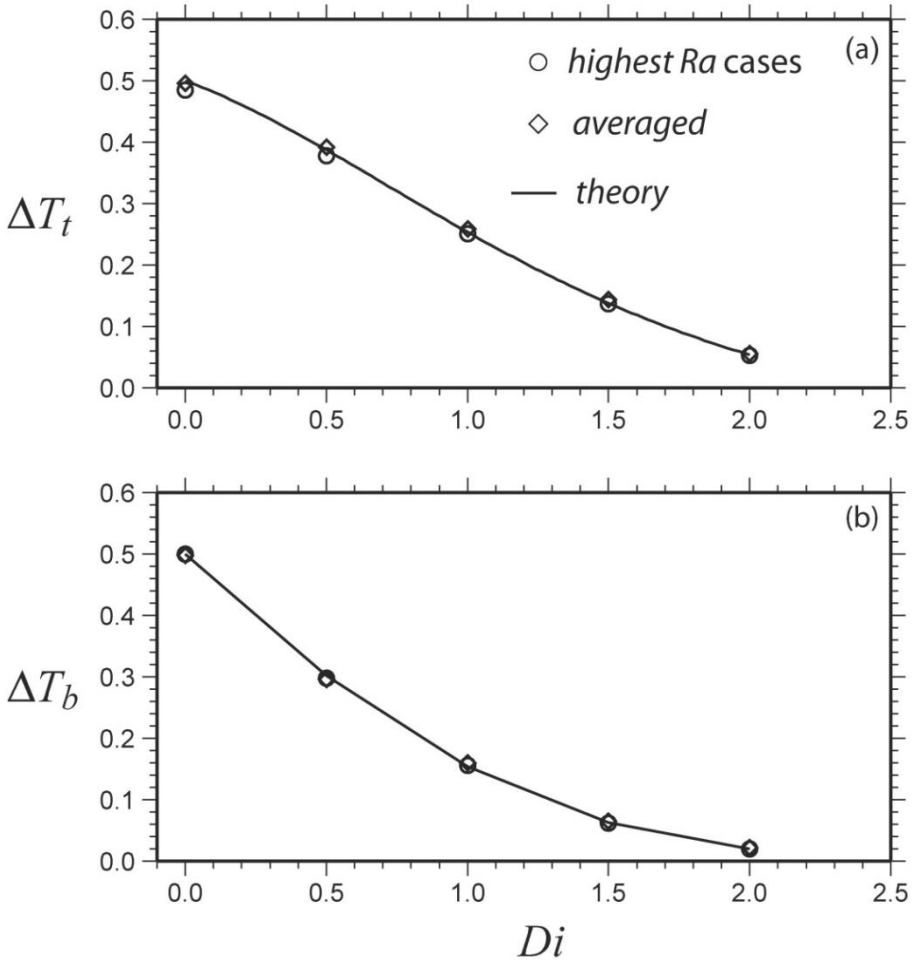

Figure 2.11. Temperature difference for (a) the top and (b) bottom TBLs versus *Di*. In (a) and (b), the lines are computed from equations (2.43) and (2.44), respectively, and the circles and diamonds are from numerical experiments. The circles are from the highest *Ra* case for each *Di* series, while the diamonds are for averaged temperature difference for each *Di* series.

Substituting equation (2.43) into equation (2.32), we find

$$Nu = \left(\frac{1 - T_s(e^{Di} - 1)}{e^{-Di/2} + e^{Di}}\right)^{4/3} \left(\frac{Ra}{Ra_t}\right)^{1/3}. \qquad (2.45)$$

From Figure 2.10, Ra_t is approximately a constant of 18 for $Di \neq 0$ cases. Using Ra_t=18 for $Di \neq 0$ cases and Ra_t=6 for $Di = 0$ in equation (2.45), Figure 2.12 shows

the comparison of *Nu* from equation (2.45) with our numerical results for all the cases with different *Ra* and *Di*. This comparison suggests that our theory as given by equation (2.45) describes the numerical results of heat transfer well.

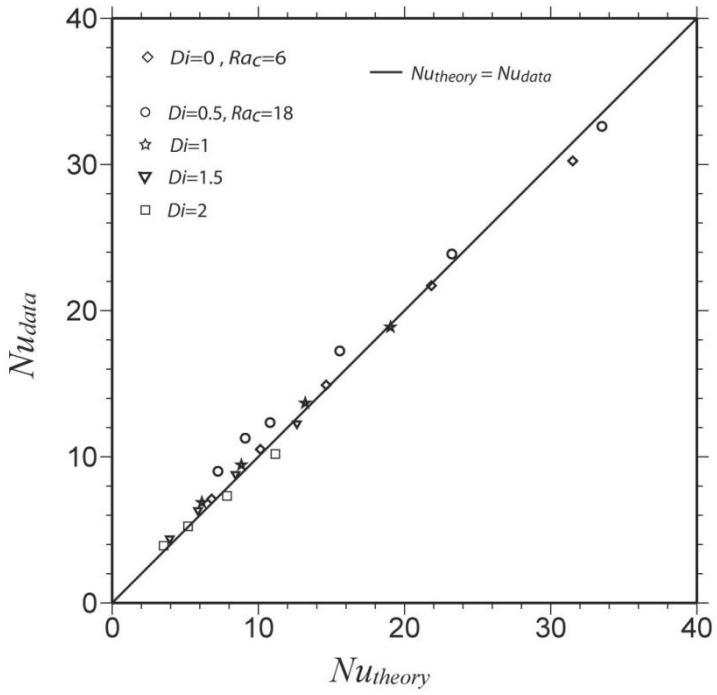

Figure 2.12. *Nu* from numerical results compared with those from equation (2.45) for cases listed in Table 2.3. The line represents $Nu_{data}=Nu_{theory}$. The symbols are for *Nu* from equation (2.45), using Ra_c =18 for *Di*>0 cases and Ra_c =6 for *Di*=0 cases. The symbols diamond, circle, star, triangle and square are for *Di* = 0, 0.5, 1, 1.5 and 2 cases, respectively.

2.5. Discussion

In this study, we formulate a 2D Cartesian compressible convection model to examine the effects of compressibility on thermal convection. We present a new implementation of propagator matrix technique for marginal linear stability analysis and determine critical Rayleigh number for different dissipation numbers *Di* and

wave-numbers k_x. In the regime of finite amplitude convection, we use a finite element code to study the influence of *Di* on thermal boundary layer (TBL) properties and heat flux for models with $k_x=\pi$ and different *Di* and *Ra*. We also develop scaling laws that describe the dependence of TBL properties and heat flux on *Di* and *Ra*.

2.5.1. Marginal linear stability analysis

Using a propagator matrix method, we have determined the critical Rayleigh number, Ra_c, for compressible convection with *Di* varying from 0 to 3. Its agreement with Ra_c determined from numerical experiments proves the robustness of the method and results. Our results indicate that if defined with surface density, Ra_c does not vary monotonically with *Di*. For example, with horizontal perturbation wave-number $k_x=\pi$, Ra_c decreases from 779 for *Di*=0 to 681 for *Di*=0.6, but Ra_c increases rapidly with *Di* for *Di* > 0.6 (Figure 2.1d). To show the robustness of the result, we computed two cases with *Di*=0 and 0.5, respectively, but with the same *Ra*=730 and $k_x=\pi$, using our finite element model. Notice that *Ra*=730 is slightly smaller than Ra_c=779 for *Di*=0.0 but larger than Ra_c=683 for *Di*=0.5. The initial temperature perturbations for these calculations are the same as described in section 2.3.2. Figure 2.3 shows that with same Ra_c=730, the kinetic energy E_k increases with time to a steady state value for *Di*=0.5 case, but decays to nearly zero for *Di*=0 case, confirming that Ra_c is smaller for *Di*=0.5 than for *Di*=0. However, it should be pointed out that if we re-define *Ra* using the averaged density rather than the surface density as in equation (2.12), Ra_c does increase monotonically with *Di* (Figure 2.1d).

Our results appear significantly different from those by Jarvis & McKenzie (1980), where the authors found that Ra_c increases much more rapidly with *Di* for models with heat flux boundary conditions at the bottom. For example, for $k_x=\pi$, Jarvis & McKenzie (1980) reported that Ra_c defined by the average density increased

from 586.8 for Di=0 to 9310 for Di=0.117, and to 2.6×10^5 for Di=0.5. It is interesting that the bottom heat flux boundary may have such a major influence on Ra_c.

Eigenfunctions for the fundamental mode and $k_x=\pi$ (Figure 2.2) show that, as Di increases, the flow in the lower region becomes more sluggish than that in the upper region. For Di=2, there is an internal node in the eigenfunction of vertical velocity, indicating a shear driven flow in the lower region. This is similar to the eigenfunction results by Jarvis & McKenzie (1980). One important conclusion from our study is that the eigenfunctions of temperature $T_0(z)$, horizontal and vertical velocities $U(z)$ and $V(z)$, for compressible convection may differ significantly from sinusoidal functions that are eigenfunctions for a homogeneous and incompressible fluid (e.g., Turcotte & Schubert, 2002). We also found that even for incompressible convection, depth-dependent thermodynamic parameters such as thermal conductivity or thermal expansion can also cause $T_0(z)$, $U(z)$ and $V(z)$ to deviate from sinusoidal functions (Figures 2.2c and 2.2d). For example, for incompressible convection with thermal conductivity increasing linearly from 1 at the top to 2 at the bottom, our analysis revealed that Ra_c = 1166 for $k_x=\pi$ and the corresponding eigenfunctions are given in Figure 2.2c. Notice that for this calculation the background conductive temperature T_r needs to be determined for the variable thermal conductivity, and dT_r/dz in the propagator matrix should be modified accordingly. We also considered a case with thermal expansion decreasing linearly from 1 at the top to 0.2 at the bottom, and for this case, Ra_c is 1295 for $k_x=\pi$ and eigenfunctions are given in Figure 2.2d. These results of Ra_c are in agreement with those determined from numerical experiments, provided that the corresponding eigenfunctions $T_0(z)$ are used as initial temperature in the calculations. Compared with Ra_c = 779 for thermal convection in

an incompressible and homogenous fluid, our results show that the depth-dependence of the thermodynamic parameters considered here stabilize the convection.

A final remark on the marginal stability analysis is on ignoring the imaginary part of the growth rate in our analysis (i.e., we only considered real number for the growth rate), while Jarvis and McKenzie (1980) considered both imaginary and real numbers for the growth rate. The growth rate with imaginary number implies oscillatory behavior. Although it is of some interest for future studies to examine the physical significance of imaginary part of the growth rate, we would like to point out that the independent verification of our marginal stability analysis from our finite element modeling (Figures 2.1b-2.1d) suggests that our analysis is robust.

2.5.2. Finite amplitude compressible convection

We have quantified convective heat flux and thermal boundary layer (TBL) properties for compressible convection at different *Ra* and *Di*. It is well known that for isoviscous and incompressible convection, the top and bottom TBLs are symmetric with both TBL thickness and temperature difference in TBL identical for the top and bottom TBLs. Compressibility breaks the symmetry. Equations (2.33) and (2.34) show that the ratios of thickness and temperature drop of the top TBL to those of the bottom TBL increase with *Di* but are insensitive to *Ra*, especially at large *Ra*, and these two equations describe the numerical results reasonably well (Figures 2.8b and 2.9b).

We also developed theoretical expressions for temperature differences across the top and bottom TBLs, ΔT_t and ΔT_b. We found that ΔT_t and ΔT_b, given by equations (2.43) and (2.44), respectively, are controlled by *Di* and insensitive to *Ra*, especially when *Ra* is large and boundary layer thicknesses are significantly smaller

than the depth of the fluid (see equation 2.42). ΔT_t and ΔT_b from equations (2.43) and (2.44) are consistent with numerical results (Figure 2.11).

Note that equations (2.43) and (2.44) for ΔT_t and ΔT_b may pose an upper bound on dissipation number *Di*, $Di_{\max}$, for which these equations are applicable. That temperature differences ΔT_t and ΔT_b must be greater than zero requires that

$$1 - T_s(e^{Di} - 1) > 0 . \tag{2.46}$$

In our models, the dimensional surface temperature T_s is set as 0.091 and is applicable to the Earth. To satisfy equation (2.46), *Di* must be smaller than ~2.5 or $Di_{\max}$~2.5. This is consistent with the diminished bottom TBLs in cases with very high *Di* (e.g., *Di*=2, $Ra=3\times10^9$, in Fig 2.6c). $Di_{\max}$ is controlled by T_s. The larger T_s is, the smaller ΔT_t and $Di_{\max}$ are. Also notice that T_s does not affect ΔT_t for *Di*=0, because $e^{Di} - 1 = 0$.

Based on our analyses of TBL properties, we developed a scaling relationship of heat flux (i.e., *Nu*) to Rayleigh number *Ra* and dissipation number *Di* for isoviscous and basal heating compressible convection at relatively large *Ra* (equation 2.45). In particular, we found that *Nu* scales with $Ra^{1/3}$, which is similar to that for incompressible thermal convection (e.g., Turcotte & Schubert, 2002), while its dependence on *Di* follows a more complicated expression due to the relationship of ΔT_t to *Di* in equation (2.43). Ra_t is needed to fully determine *Nu* in addition to *Ra* and *Di*, using equation (2.45). From numerical modeling, Ra_t does not vary with *Ra*, but appears to increase moderately with *Di* from Ra_t~6 for *Di*=0 to Ra_t~18 for *Di*=2 (Figure 2.10). For *Di* = 0 cases, Ra_t may be deduced from equation (2.28) together with ΔT_t = 0.5 and numerical results of $Nu=0.2987Ra^{0.31}$, and this leads to Ra_t ~6, which is consistent with Ra_t ~6 in Figure 2.10. Similar value of Ra_t can be obtained if $Nu = 0.294Ra^{1/3}$ from Turcotte and Schubert (2002) is used for incompressible

convection. If we simply take $Ra_t = 6$ for $Di=0$ and $Ra = 18$ for $Di > 0$, Nu predicted from equation (2.45) agree well with numerical results (Figure 2.12).

An interesting question is to understand the dependence of Ra_t on Di. Unfortunately, critical Rayleigh numbers Ra_c from our marginal stability analysis do not seem to be directly applicable to understand the effects of Di on Ra_t, since Ra_c does not vary significantly for Di varying from 0 to 1 (Figure 2.1b). However, Ra_c increases rapidly with decreasing convective wavelength or increasing wave-number k_x for $k_x > \pi$ (Figure 2.1b). We speculate that the dependence of Ra_t on Di (Figure 2.10) may also reflect the effects of decreasing convective wavelengths for cases with increasing Di (Figure 2.5). We will leave this for future studies.

Finally, we wish to point out that the Nu~Ra scaling law (i.e., equation 2.45) does not apply for convection at intermediate Ra (Figure 2.7). We think that this is because at intermediate Ra, thermal boundary layers are not yet fully developed, and the top and bottom TBLs have not been separated yet.

2.6. Conclusion

Thermal convection in an isoviscous, compressible fluid is investigated using both marginal stability analysis and finite element modeling. A technique based on a propagator matrix method is developed for marginal stability analysis of thermal convection with depth-dependent thermodynamic properties, density and viscosity. Scaling laws are developed for heat transfer and thermal boundary layer properties for thermal convection in an isoviscous, compressible fluid. The conclusions can be summarized as follows.

(1) Critical Rayleigh numbers, Ra_c, at the fundamental and higher modes are determined for thermal convection in a compressible fluid. At the fundamental mode,

if *Ra* is defined by the surface density, Ra_c may not show a monotonic variation with dissipation *Di*. The fundamental mode may only exist for relatively small *Di*.

(2) For thermal convection with depth-dependent density or thermodynamics parameters, the eigenfunctions are no longer sinusoidal functions, as they are for thermal convection in a homogeneous, incompressible fluid. For $Di > 0$, the eigenfunctions for temperature $T_0(z)$, horizontal velocity $U(z)$, and vertical velocity $V(z)$ have larger amplitudes at the shallower depth than those at the larger depths, and shear driven convective cell may appear for large *Di*.

(3) Ra_c are also determined from numerical experiments for different *Di* and wavelengths. With the eigenfunctions for temperature $T_0(z)$ as initial perturbations, numerically determined Ra_c agree well with Ra_c computed from marginal stability analysis.

(4) Thermal boundary layer (TBL) properties are quantified in numerical models of thermal convection in a compressible fluid at different *Ra* and *Di*. TBL thicknesses and temperature differences are heavily influenced by *Di*. While temperature differences across the TBLs decrease with *Di*, TBL thicknesses increase with *Di*. The ratios of top TBL thickness and temperature difference to corresponding bottom TBL properties are $e^{Di/2}$. For both incompressible and compressible convection, TBL thicknesses follow $\delta_l \sim Ra^{-1/3}$, while TBL temperature differences are insensitive to *Ra*.

(5) Our numerical modeling shows that the local Rayleigh numbers at the top and bottom TBLs are nearly identical and are insensitive to *Ra* and *Di* for compressible convection.

(6) The scaling laws of the temperature differences across TBLs, ΔT_t and ΔT_b, are derived as $\Delta T_t = [1 - T_s(e^{Di} - 1)]/(e^{-Di/2} + e^{Di})$ and

$\Delta T_b = [1 - T_s(e^{Di} - 1)]/(1 + e^{3Di/2})$. ΔT_t and ΔT_b are found only dependent on *Di*. The scaling laws are verified by numerical results.

(7) The scaling law of heat transfer, Nusselt number *Nu*, for thermal convection in an isoviscous, compressible fluid is derived to be

$Nu = (\frac{1 - T_s(e^{Di} - 1)}{e^{-Di/2} + e^{Di}})^{4/3}(\frac{Ra}{Ra_t})^{1/3}$. *Nu* scales with *Ra* as $Nu \sim Ra^{1/3}$, similar with that for incompressible convection. The scaling law for *Nu* is consistent with numerical modeling results. We think that these results may have important implications for understanding thermal evolution of super-Earths.

Chapter 3

The Long-wavelength Geoid from 3-Dimensional Spherical Models of Thermal and Thermochemical Mantle Convection[2]

Abstract: The Earth's long-wavelength geoid anomalies have long been used to constrain the dynamics and viscosity structure of the mantle in an isochemical, whole-mantle convection model. However, there is strong evidence that the seismically observed large low shear velocity provinces (LLSVPs) in the lower mantle underneath the Pacific and Africa are chemically distinct and likely denser than the ambient mantle. In this study, we have formulated dynamically self-consistent 3D spherical mantle convection models to investigate how chemically distinct and dense piles above the core-mantle boundary (CMB) may influence the geoid. Our dynamic models with realistic mantle viscosity structure produce dominantly spherical harmonic degree-2 convection, similar to that of the present-day Earth. The models produce two broad geoid and topography highs over two major thermochemical piles in the lower mantle, consistent with the positive geoid anomalies over the Pacific and African LLSVPs. Our geoid analysis showed that the bottom layer with dense chemical piles contributes negatively to the total geoid, while the layer immediately above the chemical piles contributes positively to the geoid, cancelling out the effect of the piles. Thus, the bottom part of the mantle, as a compensation layer, has zero net contribution to the total geoid, and the thickness of the compensation layer is ~1000 km or two to three times as thick as the chemical piles. Our results help constrain and interpret the large-scale thermochemical

[2] This chapter was published as "Liu, **X.**, and S.J. Zhong. The long-wavelength geoid from 3-dimensional spherical models of thermal and thermo-chemical mantle convection, *J. Geophys. Res*., **120**, doi:10.1002/2015JB012016"

structure of the mantle using surface observations of the geoid and topography, as well as seismic models of the mantle.

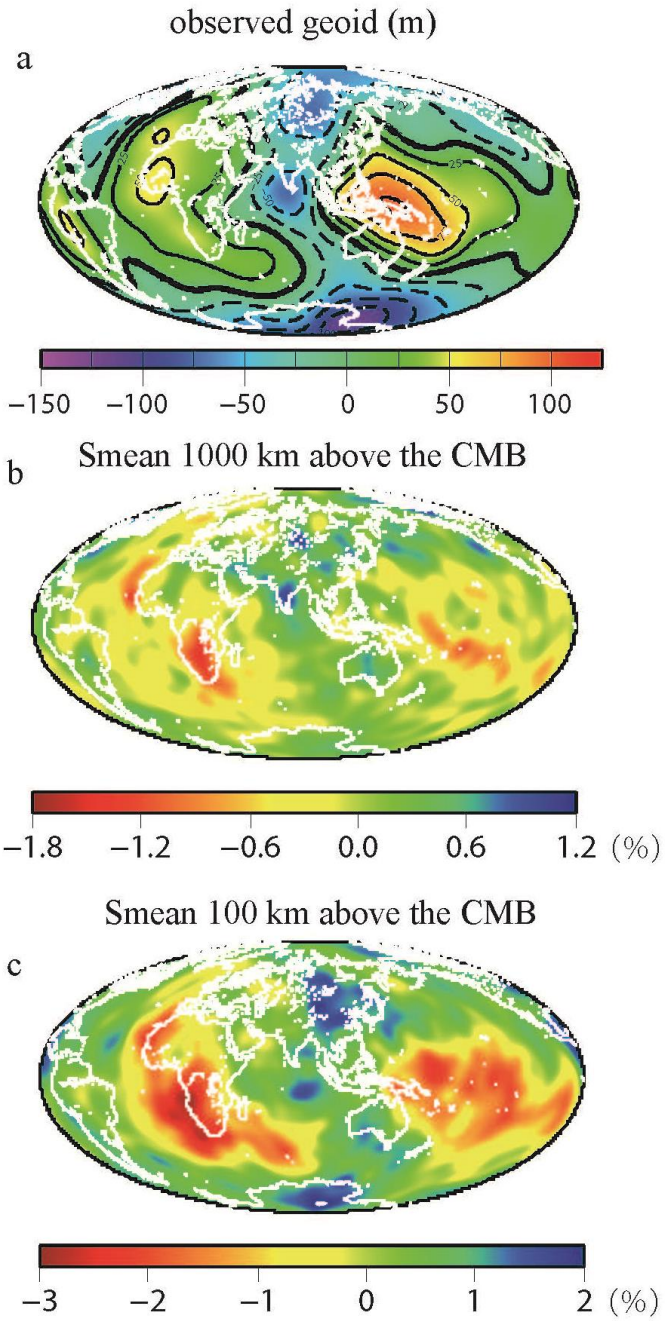

Figure 3.1. (a) The observed geoid up to degrees and orders 12, and seismic S-wave anomalies at (b) 1000 km and (c) 100 km above the CMB from Smean model (Becker and Boschi, 2002), respectively.

3.1 Introduction

The Earth's non-hydrostatic geoid provides important constraints on the structure and dynamics of the mantle (e.g., Hager and Richards, 1989; Ricard *et al.*, 1993). The geoid is controlled by both the interior density variations and the dynamic topography of the surface and core-mantle boundary (CMB) (e.g., Pekeris, 1935; Hager and Richards, 1989). The dynamic topography is caused by mantle flow, and has a strong dependence on, thus can constrain, the mantle viscosity profile (e.g., Hager and Richards, 1989). An important feature of the

geoid is its dominantly degree-2 structure with two geoid highs above Africa and the central Pacific (e.g., Lerch *et al*., 1983) (Figure 3.1a).

Seismic tomographic studies also reveal two large low shear velocity provinces (LLSVPs) in the lower mantle below Africa and the Pacific Ocean surrounded by seismically fast, circum-Pacific anomalies (e.g., Dziewonski, 1984; Tanimoto, 1990; Masters *et al*., 1996; Ritsema *et al*., 1999) (Figures 3.1b and 3.1c), which correlate well with the long wavelength geoid (e.g., Hager *et al*., 1985). The seismic anomalies are often interpreted as purely due to the thermal effect in an isochemical, whole mantle convection framework, and the LLSVPs are thought as hot and buoyant roots of the 'super-plumes' that extend to the upper mantle, form the upwelling part of the global mantle convection, and cause the African and Pacific super-swell topography (e.g., Marty and Cazenave, 1989; Davies and Pribac, 1993; Lithgow-Bertelloni and Silver, 1998; Romanowicz and Gung, 2002). Representing the seismic structures as mantle density and buoyancy structure in the purely thermal, whole mantle convection model, geodynamic studies have not only reproduced the Earth's geoid, but also provided constraints on the mantle viscosity structure (e.g. Hager & Richards, 1989).

In the past 20 years, however, various evidences suggest that the LLSVPs may be chemically distinct (e.g., Su and Dziewonski, 1997; Masters *et al*., 2000; Wen *et al*., 2001; Ni *et al*., 2002; He and Wen, 2009; Houser *et al*., 2008). The anti-correlation between shear wave and bulk sound speeds in the LLSVPs suggests a thermo-chemical origin for the seismic heterogeneities in these regions (e.g., Masters *et al*. 2000). The sharp seismic velocity contrasts at the edges of LLSVPs are better explained as features of chemically distinct piles rather than purely thermal anomalies (Wen *et al*., 2001; Ni *et al*., 2002). The thermochemical characteristics of the LLSVPs

may also reconcile geochemical inferences of chemically distinct “reservoirs” that explain the difference between the oceanic island basalt (OIB) and the mid-ocean ridge basalt (MORB) (e.g., Hofmann, 1997; Kellogg *et al*., 1999; Kunz *et al*., 1998). However, it should be pointed out that a number of recent studies have suggested that these seismic and geochemical observations could be explained as purely thermal and post-perovskite phase change effects (Davies *et al*., 2012; Schuberth *et al*., 2009, 2012; Huang and Davies, 2007), thus questioning the necessity of interpreting the LLSVPs as chemical piles.

The large-scale chemically distinct piles, if they represent the LLSVPs as proposed (e.g., Garnero and McNamara, 2008), may have significant effects on the mantle dynamics. It has been suggested that thermochemical structures in the mantle affect the buoyancy force distribution, mantle flow configuration and convective heat transfer (e.g., Tackley, 1998; Kellogg *et al*., 1999; Davaille, 1999; McNamara and Zhong, 2005a; Zhang *et al*., 2010). However, the effects of thermochemical structures on the geoid are not well understood. Hager & Richards (1989) modeled a layered mantle convection with a compositional interface at a fixed radial location that represents the top surface of the chemically distinct D” layer or the 670 km discontinuity. They showed that while density anomalies at the compositional interface do not produce any geoid anomalies (i.e., they are fully compensated), a density anomaly above the interface has opposite contribution to the geoid, compared to that below the interface. Through a joint inversion of the geoid and seismic data with a parameterization of possible compositional effect on the buoyancy, Forte & Mitrovica (2001) concluded that the LLSVPs are overall positively buoyant. Steinberger & Torsvik (2010) formulated thermochemical mantle flow models for the

geoid and true polar wander (TPW), ignoring the buoyancy in the bottom 300 km thick layer of the mantle to account for possible compositional buoyancy effects.

However, these models have a number of drawbacks and assumptions that may limit their applications. Hager & Richards (1989)'s model assumed that the chemically distinct layer is global and that the topography at the compositional interface is significantly smaller than the layer thickness. This assumption is inconsistent with seismic observations and thermochemical convection models showing that the LLSVPs or chemical piles only exist in isolated regions above the CMB with hundreds of kilometers topography (e.g., Wang and Wen, 2004; He and Wen, 2009; McNamara and Zhong, 2005a). Buoyant LLSVPs or thermochemical piles suggested by Forte & Mitrovica (2001) may be inconsistent with the geochemical evidence for primitive chemical reservoirs or piles that would require the reservoirs to be negatively buoyant to avoid being mixed and recycled. However, this argument may depend on mantle mixing process (Huang and Davies, 2007; van Keken *et al*., 2001). In Steinberger & Torsvik (2010)'s model, the removal of mantle buoyancy from the bottom 300 km thick layer is rather ad hoc.

The goal of this study is to examine the effects of chemical piles (e.g., the LLSVPs) on the geoid as well as whether positive geoid anomalies in largely degree-2 convection as for the present-day Earth can be generated above primitive chemical piles above the CMB in dynamically self-consistent mantle convection models. A key in formulating dynamically self-consistent convection models to investigate the effects of thermochemical piles on the Earth's geoid is to generate long-wavelength convective structure with two major thermochemical piles above the CMB. This is accomplished here by modeling thermochemical convection (e.g., McNamara and Zhong, 2004a) with modestly strong lithosphere and a weak upper mantle (Zhong *et*

al., 2007). Our models represent the first mantle geoid models that include realistic mantle viscosity and dynamically generated degree-2 mantle structure, although semi-dynamic models with imposed surface plate motions could produce the degree-2 mantle structure (e.g., McNamara and Zhong, 2005a). Our models indicate that positive geoid anomalies can be generated over two major thermochemical piles above the CMB in largely degree-2 mantle convection, similar to what is observed for the Earth. We also found that for the degree-2 geoid, the buoyancy from a large fraction of the bottom mantle (~1000 km in thickness) including the chemically dense piles has zero net contribution to the geoid, due to compensation effects. The paper is organized as follows. Next section describes the modeling methods for time-dependent convection models. Section 3.3 presents the modeling results, while discussions and conclusion are given in sections 3.4 and 3.5.

3.2 Model

3.2.1 Governing equations, initial and boundary conditions

The time-dependent, dynamically self-consistent thermochemical convection models are formulated in a 3-D spherical shell geometry to study the effects of thermochemical structures on the geoid. The mantle is assumed to be an incompressible fluid, and under assumptions of the Boussinesq approximation and constant thermodynamic parameters except for the viscosity, the non-dimensional governing equations for the conservation laws of the mass, momentum, energy, and composition are (Tackley, 1998; McNamara and Zhong, 2004b; Zhong *et al*., 2008):

$$\nabla \cdot \boldsymbol{u} = 0, \tag{3.1}$$

$$-\nabla p + \nabla \cdot [\eta(\nabla \boldsymbol{u} + \nabla^T \boldsymbol{u})] + Ra(T - BC)\boldsymbol{e}_r = 0, \tag{3.2}$$

$$\frac{\partial T}{\partial t} + (\boldsymbol{u} \cdot \nabla)T = \nabla^2 T + \gamma, \tag{3.3}$$

$$\frac{\partial C}{\partial t} + (\boldsymbol{u} \cdot \nabla)C = 0, \tag{3.4}$$

where $\boldsymbol{u}$ is the velocity vector; p is the dynamic pressure; η is the viscosity; $\boldsymbol{e}_r$ is the unit vector of the radial direction; *Ra* is the Rayleigh number; T is the temperature; *B* is the buoyancy number; C is the composition field; t is the time; γ is the internal heat production rate. The detailed formulation and non-dimensionalization of the equations can be found in Zhong *et al*. (2008).

The Rayleigh number Ra in equation (3.2) controls convective vigor, and is defined as

$$Ra = \frac{\rho_0 g_0 \alpha_0 R^3 \Delta T}{\eta_0 \kappa_0}, \tag{3.5}$$

where subscript 0 means reference values, ρ is the density, g is the gravitational acceleration, α is the thermal expansion coefficient, *R* is the radius of the Earth, ΔT is the temperature difference across the mantle, and κ is the thermal diffusion. Note that the Earth's radius, instead of mantle thickness, is used as the length scale to non-dimensionalize the governing equations, and our Ra is ~10 times larger than defined by mantle thickness (e.g., Zhong *et al*., 2000).

Our thermochemical models only consider two compositions that differ in intrinsic density. C measures the mantle composition, with C=0 for the regular mantle and C=1 representing the denser component. The buoyancy number *B* measures the relative strength between the compositional and thermal buoyancy, and is defined as

$$B = \frac{\Delta \rho_c}{\alpha_0 \rho_0 \Delta T}, \tag{3.6}$$

where $\Delta \rho_c$ is the intrinsic density difference between the denser and regular mantle materials.

All models are in the 3D spherical shell geometry. The top and bottom boundaries represent the surface and core-mantle boundary (CMB), and have dimensionless outer and inner radii r=1 and r=0.55, respectively. The models use free-slip as well as isothermal boundary conditions at the top and bottom boundaries with fixed temperature of 0 and 1, respectively. For the thermochemical convection, no composition flux is allowed to cross the top and bottom boundaries. The initial temperature field is a largely degree 3 structure. The initial condition for composition, which is only relevant for thermochemical models, is a denser layer with a uniform thickness of 400 km above the CMB. The volume of this dense layer is generally consistent with what is inferred for the LLSVPs (e.g., Hernlund and Houser, 2008; Wang and Wen, 2004). As we are only interested in quasi-steady state solutions, our results are insensitive to initial conditions.

We use a 3-D finite element convection package CitcomS to solve the governing equations for spherical shell mantle convection (Zhong *et al*., 2000, 2008). The particle-ratio method is employed in CitcomS to solve thermochemical convection problems (McNamara & Zhong, 2004a; Tackley and King, 2003). Parallel computing techniques are implemented in CitcomS (Zhong *et al*., 2000). The mantle is divided into 12 caps, and each cap is further divided to be run on multiple CPUs. Calculations presented in this study use 48, 96, or 192 CPUs. Models are typically computed for 20,000-50,000 time steps until heat flux reaches a quasi-steady state with a relatively stable convective structure.

3.2.2 Viscosity structure

The viscosity is both depth- and temperature-dependent, following a non-dimensional rheological equation (Zhong *et al*., 2007)

$$\eta = \eta_0(\mathrm{z}) \exp\big(E(T - T_0)\big)\,, \tag{3.7}$$

where $\eta_0(z)$ is a depth-dependent pre-factor, E is the activation energy, and $T_0 = 0.5$ is the reference temperature, which is approximately the mantle interior temperature in the models. *E* is set at 6.9078 that gives rise to 3 orders of magnitude in viscosity variations due to temperature changes from the surface to the CMB.

Since the Earth's geoid has a strong power at degree-2, our convection models are designed to produce long-wavelength, especially dominantly degree-2 convection. Generation of long-wavelength convective structure in dynamically self-consistent convection models has been an important topic in geodynamics. Bunge *et al*. (1996) reported that a viscosity increase of a factor of 30 from the upper to lower mantles as suggested from the geoid studies (e.g., Hager and Richards, 1989) increases convective wavelength, but only up to a dominantly degree-6 structure. McNamara and Zhong (2005b) found that a moderately strong lithosphere leads to dominantly degree-1 convection (i.e., the longest possible wavelength in a spherical shell) for moderate Rayleigh numbers Ra. Zhong *et al*. (2007) further demonstrated that long-wavelength convection including that of degree-1 can be generated for Earth-like Rayleigh number by considering both moderately strong lithosphere and a viscosity increase at the 670 km depth. Some recent studies produced similar long-wavelength convection, also using modestly strong lithosphere (e.g., Li *et al*., 2014a; Coltice *et al*., 2012). Following Zhong *et al*. (2007), we adjust the viscosity contrast between the lithosphere and the upper mantle to generate convection with different planforms, from dominantly degree-1, -2 to shorter wavelengths. Fixing $\eta_0(\mathrm{z})$ as 1 for the lower mantle and 1/30 for the upper mantle, but varying $\eta_0(\mathrm{z})$ in the lithosphere, denoted as $\eta_{lith0}(\mathrm{z})$, we manage to build dominantly degree-2 convection models for both purely thermal and thermochemical convection. It should be noted that our temperature-

dependent viscosity, while producing mobile-lid convection, does not produce "plate-like" surface motions (e.g., Ratcliff *et al*., 1997). Pseudo-plastic rheology may lead to "plate-like" surface motions in mantle convection (e.g., Moresi and Solomatov, 1998; Coltice *et al*., 2012). However, it remains a significant challenge to reconcile observational, laboratory and theoretical studies on rheological properties of lithosphere (e.g., Zhong and Watts, 2013).

3.2.3 Calculations of the geoid and dynamic topographies

The geoid anomalies represent gravitational potential anomalies at the surface, φ, which can be obtained by solving the Poisson's equation,

$$\nabla^2\varphi = -4\pi \mathrm{G}\delta\rho \,, \tag{3.8}$$

where G is the gravitational constant, and $\delta\rho$ includes both density variations in the interior mantle and those associated with dynamic topographies at the surface and CMB. Here the interior density anomaly $\delta\rho$ is in general given by,

$$\delta\rho = -\alpha\rho_0\delta T + \Delta\rho_c C, \tag{3.9}$$

where δT is the temperature anomaly and C denotes the composition field.

The dynamic topographies at the surface and the CMB, denoted as *s* and *b*, respectively, can be related to the radial stresses at these boundaries as (Zhong *et al*., 2008)

$$s = -\frac{\sigma_{rr\_t}}{\Delta\rho_t g}\,, \tag{3.10}$$

$$b = \frac{\sigma_{rr\_b}+\rho_{core}\varphi_b}{\Delta\rho_b g}\,, \tag{3.11}$$

where σ_{rr_t} and σ_{rr_b} are the radial stresses at the surface and CMB, respectively, which can be calculated by solving the Stokes' flow equations (i.e., equations (3.1) and (3.2)), $\Delta\rho_t$ and $\Delta\rho_b$ are the density contrast across the surface and CMB, respectively, ρ_{core} is the density of the core, and φ_b is the gravitational

potential perturbation at the CMB. The topography computed from equation (3.10) in our study includes contributions from the whole mantle, and is different from the classic definition of dynamic topography that only includes contribution from the sub-lithospheric mantle (e.g., Hager & Richards, 1989).

The geoid calculations incorporate the self-gravitation effects, although the equations presented above did not include this effect for simplicity. With the self-gravitation effect, an additional term $-\rho\delta g\overrightarrow{\boldsymbol{e_r}}$ should be added to the left side of equation (3.2) where $\delta g = -|\nabla\varphi|$ is the perturbation to the radial gravity (e.g., Zhong *et al*., 2008). An efficient approach to solve the momentum equation, dynamic topographies, gravitational potential and geoid with the self-gravitation is to introduce a reduced pressure term (e.g., Zhong *et al*., 2008).

3.3 Results

In this section, we will present the results of convective structure and geoid for the time-dependent and dynamically self-consistent mantle convection models. Numerical models for both purely thermal and thermochemical mantle convection are computed at two different Rayleigh numbers (Ra=5×10^7 and 1.5×10^8). Constant thermodynamic parameters, except the viscosity, are used for all models (Table 3.1). The viscosity is both depth- and temperature- dependent, and the viscosity pre-factor in the lithosphere, $\eta_{litho}(z)$, is explored to achieve a predominantly long-wavelength convective structure (e.g., degree 2). Numerical grids of 12×65^3 are used for the cases with Ra=5×10^7, and grids of 12×97^3 are used for the higher Ra cases. The internal heating γ (equation 3.3) is 50 and 70 for Ra=5×10^7 and 1.5×10^8, respectively, leading to internal heating ratios of approximately 50% for these cases (i.e., the core and

mantle each contributes half of the surface heat flux). For the thermochemical models, the buoyancy number *B* is varied to generate relatively stable chemical piles above the CMB. In general, a small buoyancy number leads to rapid overturn and destruction of a chemical layer, while a large buoyancy number results in a stable chemical layer with a flat surface but no chemical piles (e.g., McNamara and Zhong, 2004b; Oldham and Davies, 2004). Our model calculations show that dominantly degree-2 structure can be generated for thermochemical models with B=0.8 and 0.5 for $Ra=5\times10^{7}$and 1.5×10^{8}, respectively. Because the primary interest of this study is on the geoid, we only present 4 cases that display dominantly degree-2 mantle structures, at two

Table 3.1. The thermodynamic parameters.

Parameters	Value
Earth's radius, R	6370 km
Mantle thickness, h	2870 km
Gravitational acceleration	9.8 ms^{-2}
Mantle density	3300 kgm^{-3}
Thermal diffusivity	1×10^{-6} m^2s^{-1}
Thermal expansion	3×10^{-5} K^{-1}
Temperature difference	2700 K
Specific heat	10^3 $m^2s^{-2}K^{-1}$

different Ra, each with thermal and thermochemical convection models.

3.3.1 A purely thermal convection model at Ra=5×10^7

In Case 1, the viscosity pre-factors, η_0(z), are 1, 1/30, and 0.27 for the lower mantle, upper mantle, and lithosphere, respectively (Table 3.2). Starting from a 3D temperature with a dominantly degree-3 structure, the model quickly reaches a statistically steady state with dimensionless surface heat flux of ~42 (Figure 3.2a). The internal heating ratio is 44%. The power spectra of the temperature structure within the top thermal boundary layer (i.e., at a depth of 100 km) is used to characterize convective structure. For each spherical harmonic degree *l*, the power spectrum of a function f is

$$F_l = \sum_{m=0}^{l}[(f_{cos}^{lm})^2 + (f_{sin}^{lm})^2] \,, \tag{3.12}$$

where f_{cos}^{lm} and f_{sin}^{lm} are the cosine and sine coefficients of spherical expansion of the function *f* at degree *l* and order *m*, respectively. The power spectra as a function of time for degrees 1 to 4 for Case 1 are presented in Figure 3.2b. Although the degree-1 convective structure becomes the strongest at the end, there is a significant time period during which degree-2 structure is significant.

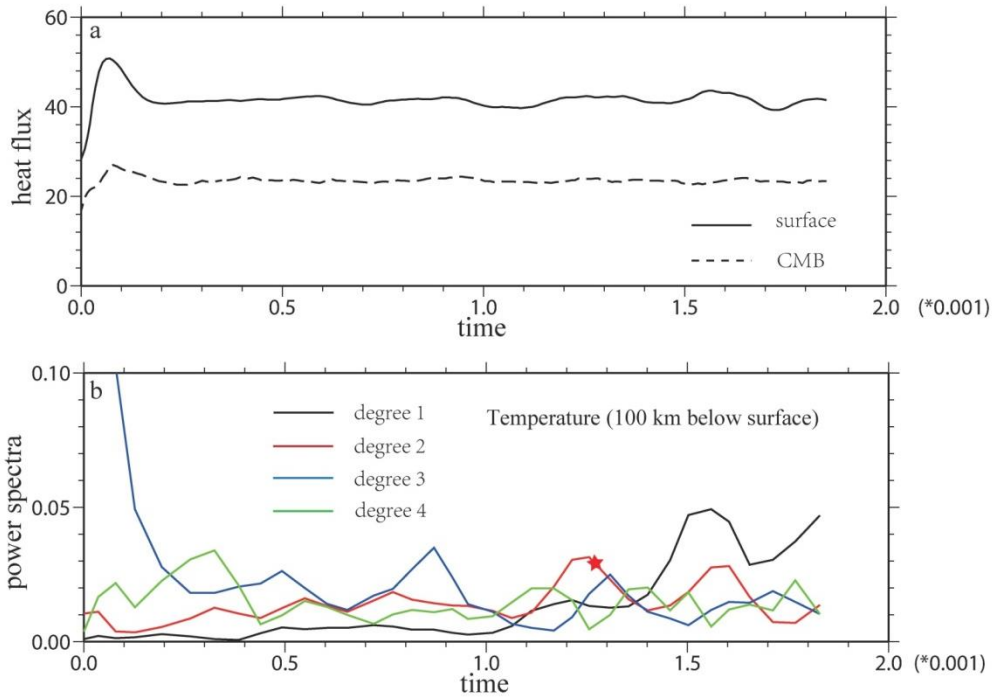

Figure 3.2. Time dependence of (a) the nondimensional surface (solid line) and CMB (dashed line) heat flux, and of (b) the power spectra for temperature structure at 100 km depth for degrees 1 to 4, denoted by black, red, blue, and green lines, respectively, for Case 1. The red star in (b) marks the time with a dominantly degree 2 convective structure that is used for the structure and geoid analyses. In (a), the CMB heat flux is plotted after taking into account of the surface area effect.

A snapshot of a dominantly degree-2 convective structure (time marked in Figure 3.2b) is used for the geoid analysis. A 3D isosurface plot for the temperature anomalies at this time step (Figure 3.3a) shows two clusters of downwellings and upwellings, which are indicative of a dominantly degree-2 structure, as also displayed in 2D plots of temperature structure at a depth of 100 km (Figure 3.4a) and 100 km above the CMB (Figure 3.4b). Figure 3b shows the horizontally averaged temperature, indicating two well-developed thermal boundary layers (TBLs) at the surface and

bottom. The horizontally averaged viscosity shows that the average lithospheric viscosity is ~60 times of the upper mantle viscosity, while the lower mantle viscosity is ~30 times larger than the upper mantle (Figure 3.3c). Scaled by parameters in Table 3.1, $Ra=5\times10^{7}$ indicates a reference viscosity of $\sim1.4\times10^{22}$Pa·s, and the lower mantle viscosity of $\sim3\times10^{22}$ Pa·s, which is comparable to that inferred from post-glacial rebound study (Simons and Hager, 1997; Mitrovica and Forte, 2004). The root-mean-square (RMS) of the horizontal velocity indicates a mobile-lid convection with surface velocity that is comparable to that in the upper mantle (Figure 3.3d).

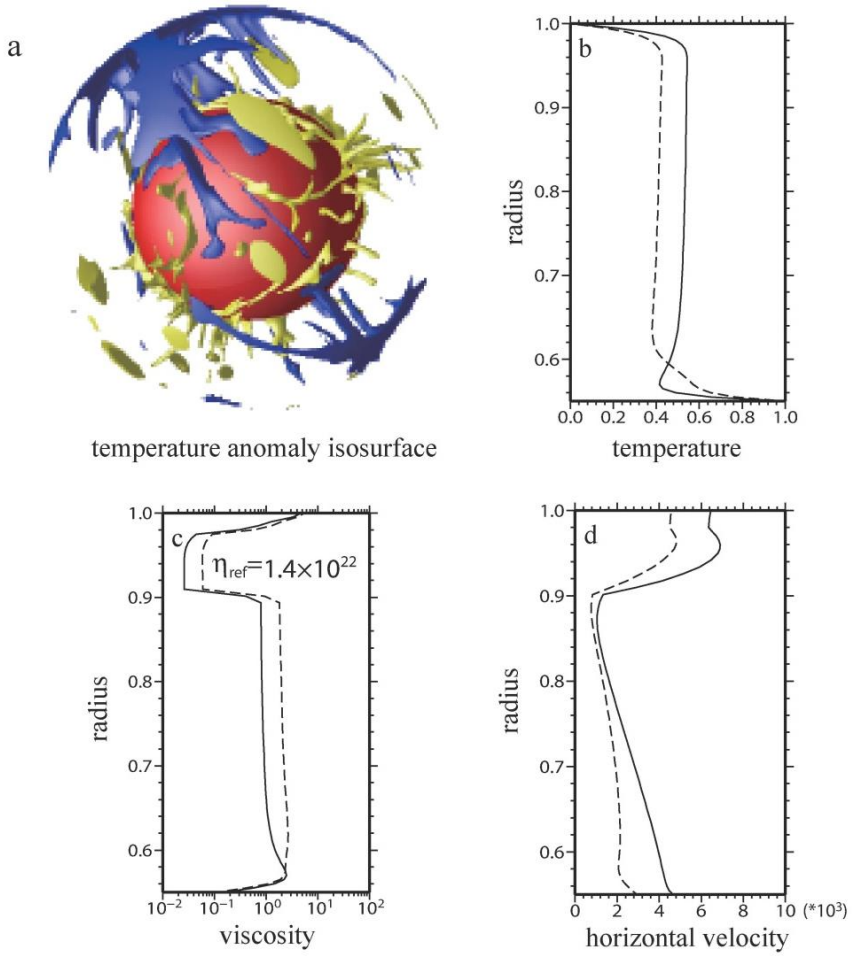

Figure 3.3. (a) The isosurface of temperature anomalies δT=-0.2 and δT=0.2 in blue and yellow, respectively, for a representative snapshot of Case 1, horizontally averaged (b) temperature, (c) viscosity, and (d) horizontal velocity, for representative snapshots of both Case 1 (solid line) and Case 2 (dash line). The reference viscosity is determined to be 1.4×10^{22} Pa·s, using $Ra=5\times10^{7}$ for Cases 1 and 2 and parameters in Table 3.1.

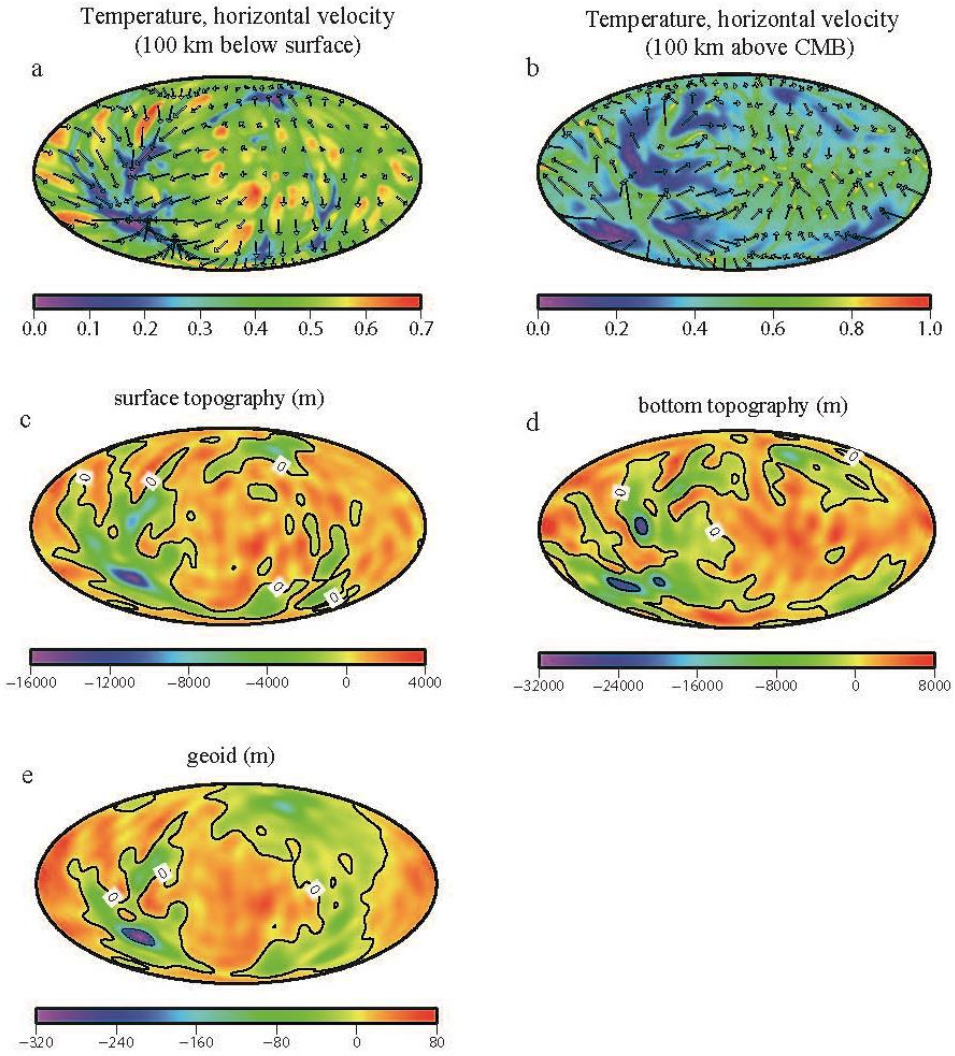

Figure 3.4. Temperature structures at (a) 100 km depth and (b) 100 km above the CMB, (c) the surface and (d) the bottom topographies, and (e) the surface geoid, all for Case 1. Arrows in both (a) and (b) denote the horizontal velocities at corresponding depths. Contour lines of 0 m are plotted on (c)-(e).

Surface and CMB topographies as well as the surface geoid at the corresponding time are computed and scaled to dimensional values using physical parameters in Table 3.1 (Figures 3.4c-3.4e). Notice that the surface topographies presented in this study include contributions from both the top thermal boundary layer and the underlying mantle, while dynamic topography typically excludes the contribution from the lithosphere (i.e., the top thermal boundary layer) (e.g., Hager and Richards, 1989), and the difference is presented in the discussion section. The topographies are well correlated with the convective structure, and are negative in the cold downwelling regions and positive in hot upwelling regions. The negative topographies in downwelling regions have much larger magnitudes than the positive topographies over upwellings, due partly to the high viscosity associated with cold downwellings that tends to increase the coupling of downwellings to the top and bottom boundaries. The geoid is prevailingly at long-wavelengths with a dominantly degree 2 structure (Figures 3.4e and 3.5a). The long-wavelength geoid is positive over the two major upwelling regions, and is negative elsewhere (e.g., major downwelling regions). The largest negative geoid of -320 m is above the center of one major downwelling, and its magnitude is 3 times larger than that of the maximum positive geoid of ~80 m. The general pattern of the positive geoid over two major upwelling systems from the model is consistent with the observed for the present-day Earth (Figure 3.1).

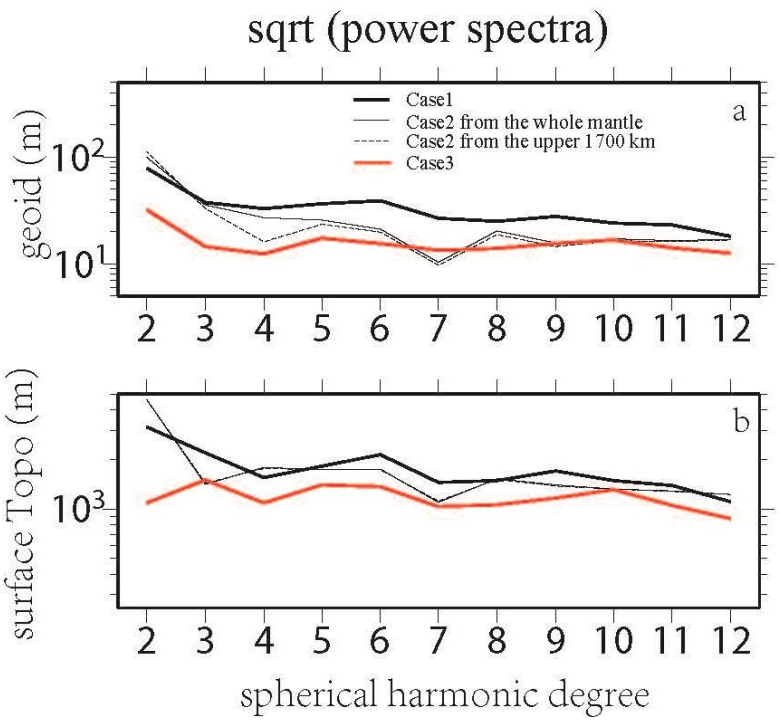

Figure 3.5. Square root of power spectra of (a) geoid and (b) surface topography at degrees 2-12 for Case 1(solid black), Case 2 from the buoyancy of the whole mantle (thin black) and of the upper 1700 km of the mantle (thin dashed black), and Case 3 (red).

We now analyze the contribution of buoyancy at different depths to the surface geoid. Our mantle convection model employs 64 unevenly distributed elements in the radial direction. The geoid contributed from buoyancy at each of these 64 layers can be computed by solving the Stokes' flow equations for the topographies and then the Poisson's equation (equation 3.8), using the buoyancy from that layer but the same 3-D mantle viscosity as in the global calculations. Using the same 3-D viscosity to compute the geoid (and topographies) from each element layer of buoyancy guarantees that the summation of the geoid (and topographies) from all the layers is equal to the total geoid in Figure 3.4e, as the Stokes' flow equations with a

fixed 3-D viscosity are linear. The geoid from each element layer is further divided by the layer thickness to represent the geoid contributed from the layer per unit thickness (i.e., per kilometer). Figures 3.6a, 3.6c, and 3.6e show the geoid from three layers at depths of 200 km and 1400 km, and 200 km above the CMB. The corresponding buoyancy structures for the three layers are given in figures 3.6b, 3.6d, and 3.6f where the buoyancy is defined as $-\delta\rho = \alpha\rho_0\delta T - \Delta\rho_c C$, with a unit of kg/m^3. While the buoyancy is comparable in both wavelengths and magnitude at the top and the bottom TBLs (Figures 3.6b, 3.6f, 3.7d and 3.7e), the geoid from the top TBL is significantly larger than that from the bottom TBL (Figures 3.6a, 3.6e, and 3.7b) due to attenuation effects. Although the buoyancy at the middle mantle has significant short-wavelength structure (Figures 3.6d, 3.7d and 3.7e), its geoid is still dominated by long-wavelengths (Figures 3.6c and 3.7a), again due to attenuation effects that reduce short-wavelength structures. The normalized power spectra of the geoid from each depth (Figure 3.7a) show that degree-2 component is the strongest at nearly all depths except for the mid-mantle where degrees 3 and 4 are the strongest. Figure 3.7b shows the maximum geoid power among all the degrees at different depth that is used to normalize the power spectra as shown in Figure 3.7a. Figure 3.7b indicates that the top 300 km and the bottom 1000 km of the mantle contribute the most to the surface geoid, while the mid-mantle's contribution is small.

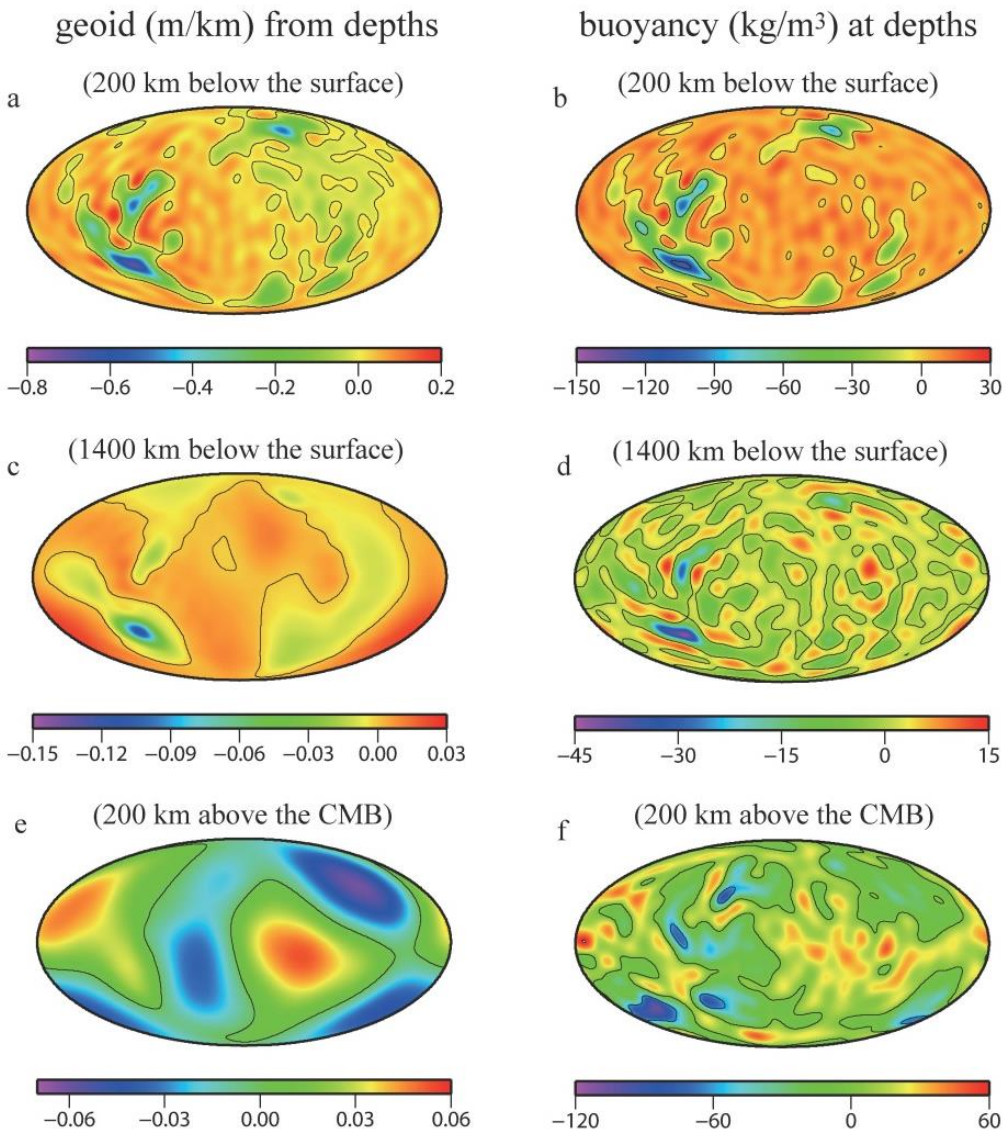

Figure 3.6. (a) The geoid produced by (b) mantle buoyancy at 200 km depth, (c) and (d) for those from 1400 km depth, and (e) and (f) for those at 200 km above the CMB, all for Case 1. The buoyancy and the geoid are all given as per unit thickness (i.e., per kilometer). The contour lines of 0 are plotted on (a)-(f).

The degree-correlation C_l between the geoid from a unit-thickness layer at each depth, h, and the total geoid H is computed for degrees 2-10 (Figure 3.7c), following

$$C_l = \frac{\sum_{m=0}^{l}(H_{sin}^{lm}h_{sin}^{lm}+H_{cos}^{lm}h_{cos}^{lm})}{\sqrt{H_l h_l}}, \quad (3.13)$$

where h_l and H_l represent the power of h and H at degree l, respectively, which are computed by equation (3.12). The degree-2 correlation is mostly positive except for at depth of ~600 km for all the degrees (Figure 3.7c), suggesting that the buoyancy at different depths mostly contributes positively to the surface geoid. Also note that the geoid power at ~600 km depth is small (Figure 3.7b).

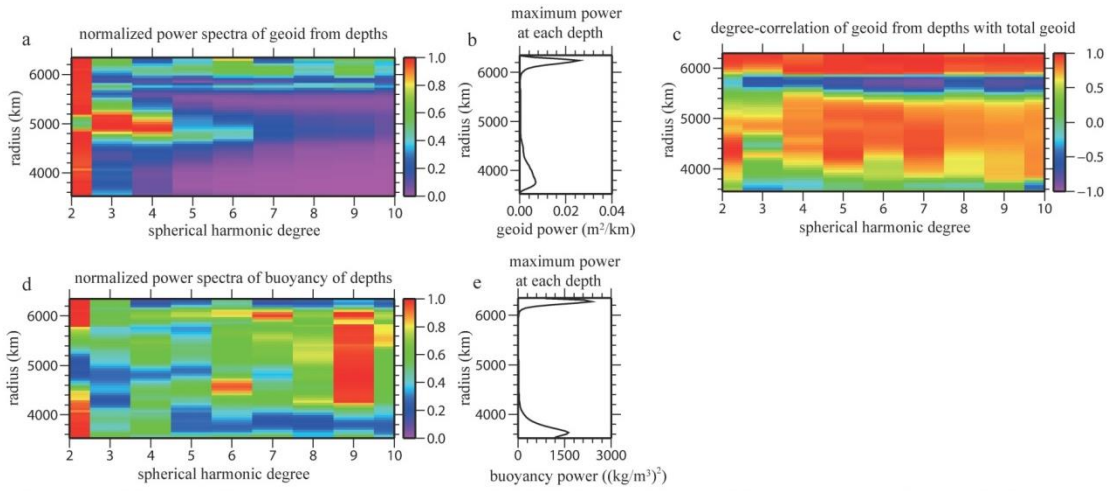

Figure 3.7. (a) The normalized power spectra of the geoid and (b) the maximum geoid power per unit thickness for degrees 2-10 produced from buoyancy at different depths, (c) the degree-correlation for degrees 2-10 between the total geoid and the geoid contributed from each layer, (d) and (c) normalized buoyancy spectra and maximum power at different depths, all for Case 1. Note that the maximum power at different depths in (b) and (e) are used to normalize the power spectra shown in (a) and (d), respectively.

3.3.2 A thermochemical convection model with Ra=5×10^7

Case 2 is identical to Case 1 except for including a compositionally distinct material above the CMB with buoyancy number *B*=0.8 (Table 3.1), which corresponds to an intrinsic density difference of 210 kg/m^3 relative to the normal mantle, using parameters in Table 3.1. The same initial temperature field as in Case 1 is used for Case 2, and initially the compositionally distinct material is uniformly distributed in a 400 km thick layer above the CMB. The model is computed for about 40,000 time steps and reaches a quasi-steady state. The convective structure is dominated by long-wavelengths, similar to Case 1, suggesting that the chemically distinct material plays a relatively minor and passive role in forming convective structure in Case 2.

In Case 2, convective structure with dominantly degree-2 component persists for a long time (>2 Ga) and we choose a time step with a well-developed degree-2 structure for geoid analysis (Figure 3.8). Temperatures are high within and above two chemical piles, indicating that two major upwellings are formed above the piles (Figure 3.8a). The two chemical piles extend to ~400 km above the CMB, but their areal extent shrinks with distance from the CMB (Figures 3.8b and 3.8c). Considering that the chemical layer initially has a uniform thickness of 400 km, the configuration of the chemical piles (Figures 3.8b and 3.8c) suggests that their volume has been reduced significantly due to entrainment after long time integration. The entrained materials are dispersed throughout the mantle but do not seem to form any coherent structure to affect the large-scale mantle dynamics. The horizontally averaged temperature and horizontal velocity, as well as the viscosity contrast between the lithosphere and the upper mantle are smaller than those for the purely thermal model (Figures 3.3b-3.3d).

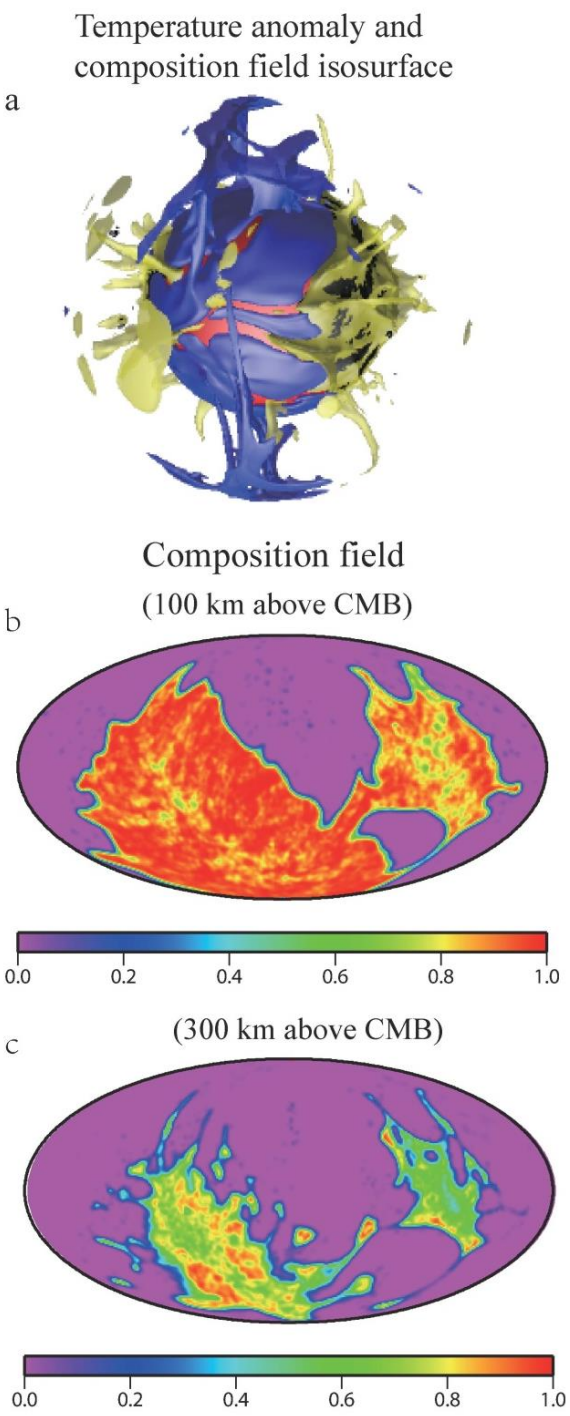

Figure 3.8. (a) The isosurface of temperature anomalies δT=-0.2 and δT=0.2 in blue and yellow, respectively, for a representative snapshot of Case 2, and composition field at (b) 100km and (c) 300 km above the CMB, respectively. In (a), the black isosurface below the upwelling plumes (i.e., yellow isosurfaces) represents chemical piles.

Figures 3.9a and 3.9b show the temperature and horizontal velocity at a depth of 100 km and 100 km above the CMB. Two broad warm regions in the upper mantle occur above the two chemical piles, and the chemical piles above the CMB are separated by cold downwellings (Figures 3.9a and 3.9b). Horizontal velocities above the CMB indicate that there are two separated convective systems inside and outside the chemical piles (Figure 3.9b). Outside of chemical piles, the horizontal flow from downwellings reaches piles' edge and continues along the upper boundary of the piles, introducing counter flow inside of the chemical piles due to shear coupling.

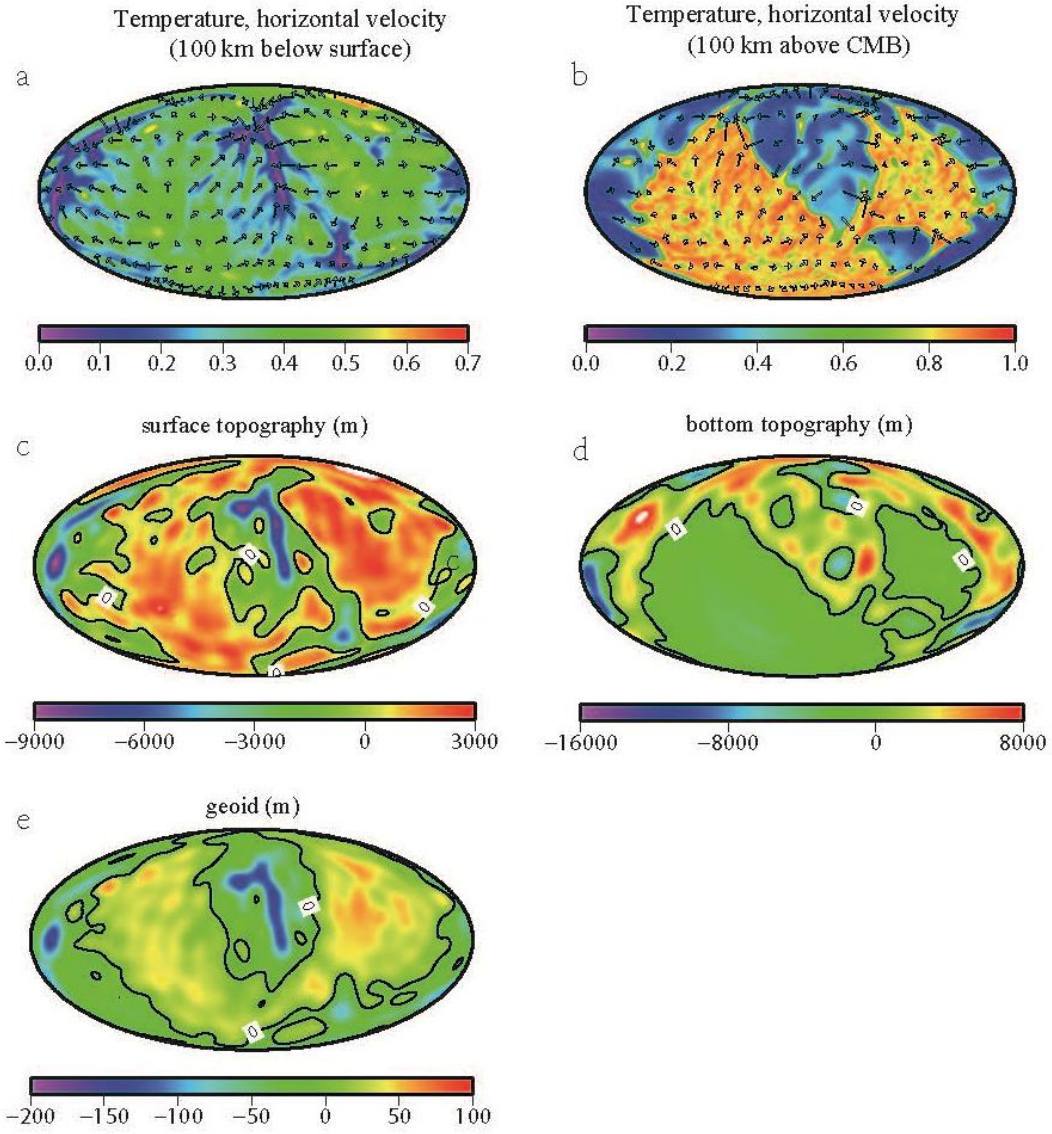

Figure 3.9. Temperature structures at (a) 100 km depth and (b) 100 km above the CMB, (c) the surface and (d) the bottom topographies, and (e) the surface geoid, all for Case 2. Arrows in both (a) and (b) denote the horizontal velocities at corresponding depths. Contour lines of 0 m are plotted on (c)-(e).

The surface topography is positive in two broad regions of upwellings over the chemical piles, and is negative in downwelling regions (Figure 3.9c). The magnitude of the negative topography is up to 3 times that of the positive topography. The range of surface topography of Case 2 is reduced by ~40% compared with that of Case 1. However, the degree 2 topography is stronger in Case 2 than that in Case 1 (Fig 3.5b), due to a stronger degree-2 structure in Case 2. At the large scale (i.e., degrees 2 and 3), the surface topography is in the range of ±3 km. The CMB topography under the chemical piles ranges from zero to slightly negative and is extremely smooth (Figure 3.9d), However, the most negative CMB topography occurs in the central regions of downwellings outside the piles, while the positive CMB topography is also outside the chemical piles (Figure 3.9d). Compared with Case 1, the amplitude of the negative CMB topography in Case 2 is also reduced significantly, as a result of compensation associated with the deformation of the chemical piles.

Two major positive geoid anomalies occur in the regions with positive surface topography above the chemical piles, while the long-wavelength negative geoid is in downwelling regions (Figure 3.9e). The geoid has the strongest power at degree 2 (Figure 3.5a). It is interesting to note that Case 2 resembles the present-day Earth's scenario in which the long-wavelength geoid and topography highs occur above the African and Pacific LLSVPs (or thermochemical piles) that are separated by circum-Pacific subducted slabs. Moreover, the large-scale geoid (degrees 2 and 3) of ~±80m in Case 2 is close to that observed on the Earth. This suggests that the positive long-wavelength geoid anomalies in the Pacific and Africa are consistent with the interpretation of the two LLSVPs as chemically denser, possibly primitive thermochemical piles.

We repeat the geoid analysis for contribution from different depths as done for Case 1. The normalized power spectra of the geoid versus depth reveal that degree 2 is the strongest for almost all depths except at ~400 km above the CMB where degree 3 is the strongest (Figure 3.10a). Notice that at ~400 km above the CMB the chemical piles largely disappear. The maximum power of the geoid is high in the lower mantle and is the largest at ~300 km above the CMB, within the radial extent of the chemical piles (Figure 3.10b), which is different from that in Case 1 of purely thermal convection (Figure 3.7b). This suggests that the chemical piles have an important effect on the geoid.

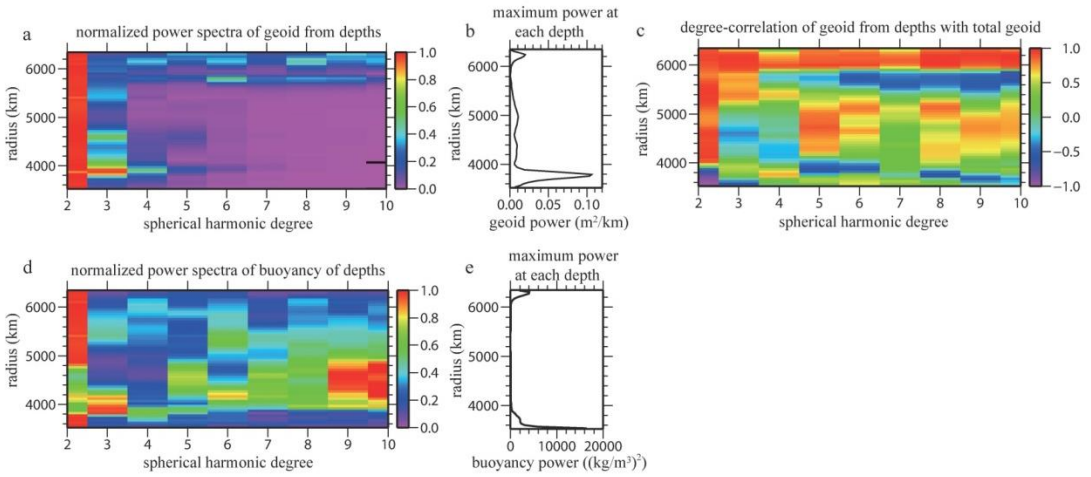

Figure 3.10. (a) The normalized power spectra of the geoid and (b) the maximum geoid power per unit thickness for degrees 2-10 produced from buoyancy at different depths, (c) the degree-correlation for degrees 2-10 between the total geoid and the geoid contributed from each layer, (d) and (c) normalized buoyancy spectra and maximum power at different depths, all for Case 2. Note that the maximum power at different depths in (b) and (e) are used to normalize the power spectra shown in (a) and (d), respectively.

The degree-correlation of the geoid from each depth with the total geoid shows high correlation in the upper mantle for all the degrees (Figure 3.10c), similar to Case 1 (Figure 3.7c). At degree 2, while the correlation is high and positive for the top ~2300 km of the mantle, the correlation is high but negative for the bottom ~400 km of the mantle (Figure 3.10c) which is different from that for Case 1. The negative correlations also exist for degrees 3 for the bottom 200 km of the mantle.

The negative correlation at degrees 2 and 3 between the geoid from buoyancy immediately above the CMB and the total surface geoid occurs where the chemical piles are, suggesting that the chemical piles may contribute negatively to the surface geoid. This is supported by analysis of the geoid from the buoyancy at 300 km (i.e., within the chemical piles) and 600 km (above the piles) above the CMB. At 300 km above the CMB, the buoyancy is negative within the piles and is dominantly degree-2 (Figures 3.11b and 3.10d). The resulting geoid is strongly degree 2 with two negative geoid anomalies over the piles (Figure 3.11a) and is negatively correlated with the total surface geoid at long wavelengths (Figures 3.9e and 3.10c). At 600 km above the CMB, while the buoyancy has significantly shorter wavelengths (Figure 3.10d), it is generally positive above the chemical piles (Figure 3.11d). The resulting geoid is positive over two broad regions approximately above the chemical piles (Figure 3.11c), and is positively correlated with the total surface geoid (Figures 3.9e and 3.10c).

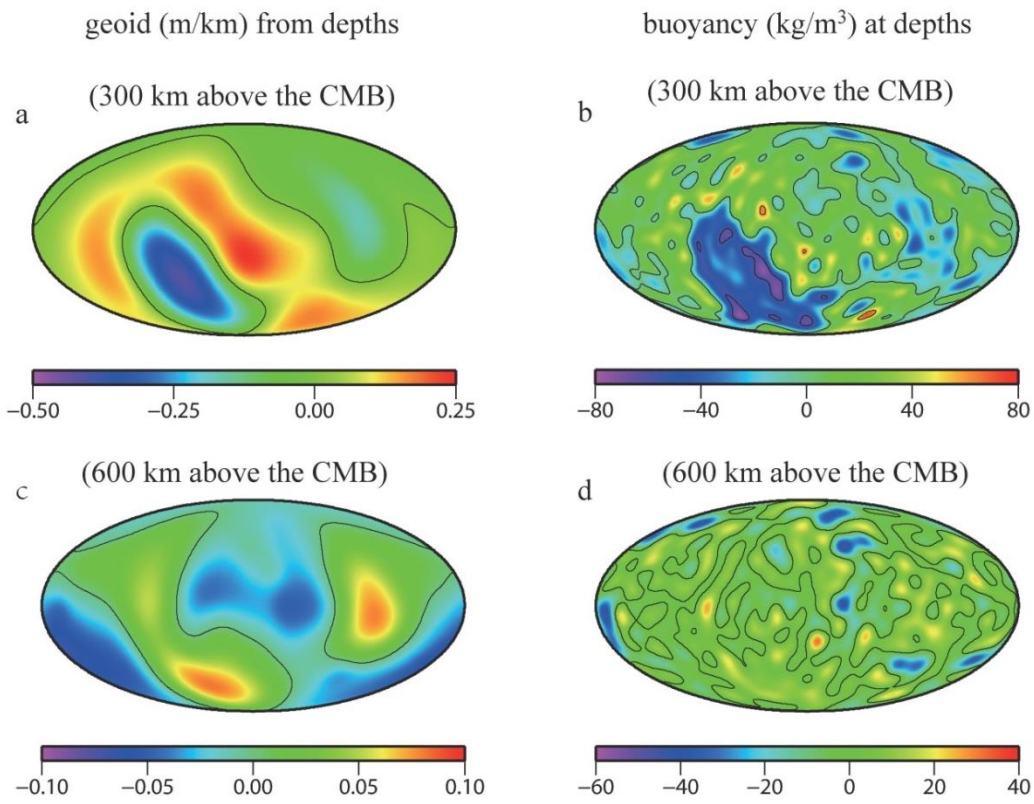

Figure 3.11. (a) The geoid produced by (b) mantle buoyancy at 300 km above the CMB (within the chemical piles), and (c) and (d) for the corresponding geoid and buoyancy from the layer at 600 km above the CMB (above the chemical piles), all for Case 2. The geoid in (a) and (c) are given as per unit thickness (i.e., per kilometer).

The highly negatively correlated geoid from the layers within the chemical piles suggests that the geoid from these regions of the lower mantle may be cancelled or compensated by the geoid from the mantle above the piles. We define the geoid contribution of the buoyancy from a unit-thickness layer at a depth, denoted as *h*, to the total geoid *H* at degree *l*, R_l , as

$$R_l = \frac{\sum_{m=0}^{l}(H_{sin}^{lm}h_{sin}^{lm}+H_{cos}^{lm}h_{cos}^{lm})}{\sqrt{H_l H_l}}, \qquad (3.14)$$

where all the variables are defined following equations (3.12) and (3.13). Equation (3.14) is valid when the magnitude of degree-correlation between h and H at degree l is high, such as degree 2 (Figure 3.10b) in Case 2. The degree contribution R_2 (i.e., for degree-2) is plotted in Figure 3.12a. By integrating R_2 over radius from CMB upwards, it is found that the bottom 400 km of the mantle with the chemical piles contributes ~ -60% to the total geoid at degree-2, and the negative contribution is cancelled by the geoid from a ~ 800 km thick layer right above the chemical piles. As a result, the bottom ~1200 km is fully compensated with no net contribution to the surface geoid at degree-2. The depth contribution to the total geoid for Case 1 is also plotted for comparison (Figure 3.12a), and no similar compensation effect exists for Case 1. Therefore, the compensation effect is unique to thermochemical convection where the gravity anomalies from negatively buoyant chemical piles are offset and cancelled by those from hot, buoyant normal mantle above the piles.

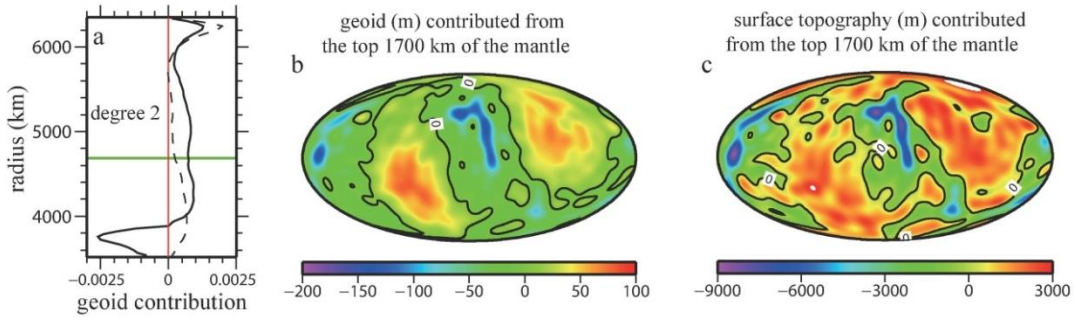

Figure 3.12. (a) The degree 2 contribution to the total geoid from the layer with unit thickness at different depths for both Case 2 (solid black line) and Case 1 (dashed black line), (b) the geoid and (c) the surface topography contributed from the top 1700 km of the mantle of Case 2. In (a), the red line represents the reference value of 0, and the green line denotes the compensation region for Case 2, below which the net contribution to the total geoid is 0. Contour lines of 0 m are plotted in (b) and (c).

To further illustrate the compensation effect, we compute the geoid resulting from the buoyancy of the top ~ 1700 km of the mantle (i.e., ignoring the bottom 1200 km of the mantle), and the resulting geoid (Figure 3.12b) is quite similar to the geoid from using the whole mantle buoyancy (Figures 3.9e and 3.5a). At degree 2, the geoid from the top 1700 km of the mantle buoyancy correlates at ~90% with, but has ~12% larger amplitude than the original degree-2 geoid (Figure 3.5a) The amplitude difference results from both imperfect correlation at degree-2, which implies difference in degree-2 geoid patterns, and finite radial numerical resolution. Although the compensation thickness of 1200 km is determined by considering the degree-2 geoid only (Figure 3.12a), the overall similarity between the geoid with and without the bottom 1200 km of the mantle structure arises because the geoid has the strongest power at degree-2 and also because the deep mantle tends to have small effects on the

geoid at relatively short wavelengths (Figure 3.5a). Surface topography produced by the upper 1700 km of the mantle for Case 2 is nearly identical to that by the entire mantle (Figures 3.9c, 3.12c and 3.5b), and the former has a total degree-correlation of 99.9% with and a contribution of 99.7% to the later for degrees 1-12. Similar layer analysis for the surface topography to that for the geoid shows that the surface topography contributed from the upper part of the mantle have much stronger power than that from the bottom part of the mantle, and thus is insensitive to the lower mantle buoyancy structure.

Finally, it should be pointed out that numerical entrainment is inevitable in thermochemical convection calculations (e.g., van Keken *et al*., 1997) and it often requires special attention such as high resolution using adaptive mesh refinement (e.g., Leng and Zhong, 2011; Davies *et al*., 2007). Compositionally dense material is constantly entrained and mixed with the normal fluid in thermochemical convection. This entrainment would eventually destroy the chemical heterogeneities, and homogenizes the fluids (e.g., Jellinek and Manga, 2002; Davaille, 1999; McNamara and Zhong, 2004a). However, numerical models tend to significantly overestimate the entrainment rates. The large numerical entrainment rate may reduce the size of chemical piles significantly faster than it should. To reduce the impact of numerical entrainment on the dynamics and the geoid analysis, we implement a scheme to re-define compositional field C to maintain the original compositional difference in our modeling. After we identify a certain time window in which the geoid analysis is to be performed, we re-define the compositional field C by assigning C to be either 1 or 0, depending whether or not the original C is larger than a threshold value (e.g., 0.5). Using the newly defined C, we re-compute the models for ~5000 time steps over the time window of interest, and the geoid analysis is then performed for the time frames

with the re-defined compositional field. We found that the geoid results as presented above are insensitive to time steps.

3.3.3 Models with Ra=1.5×10^8

Rayleigh number (Ra) controls the convection vigor, and heat flux as well as surface convective velocity increase with Ra. The dimensionless quasi-steady state averaged surface heat flux of Cases 1 and 2 are ~42 and ~26, respectively, corresponding to a total surface heat flux of 30 TW and 18 TW, based on the parameters in Table 3.1. They both are significantly lower than the Earth's mantle convective heat flux of ~36 TW (e.g., Davies, 1999). The surface RMS velocities for Cases 1 and 2, averaged for the degree 2 dominant quasi-steady state, are 3.2 cm/yr and 1.3 cm/yr, respectively, and are smaller than the averaged present-day plate speed of ~4 cm/yr (Gordon and Jurdy, 1986). The lower mantle viscosities for Cases 1 and 2 are about 10^{22} Pa·s and ~3×10^{22} Pa·s, respectively (Figure 3.3c), which are comparable with but still larger than the estimated from post-glacial rebound (e.g., Simons and Hager, 1997). Therefore, it is important to examine the possible effects of larger Ra on compensation effects seen in thermochemical convection model of Case 2. To test such effects, we formulate both purely thermal and thermochemical convection models with Ra=1.5×10^8. It is found that the main results for models with intermediate Ra, as presented in sections 3.3.1 and 3.3.2, also hold for models with Ra=1.5×10^8. Cases with a higher Ra, however, seem to systematically reduce the dynamic topography and geoid, as presented below.

The initial temperature condition for the purely thermal convection model with Ra=1.5×10^8 (Case 3) is the same as in Case 1. Case 3 has viscosity pre-factors of 0.3, 1/30, and 1 in the lithosphere, the upper mantle, and the lower mantle, respectively, which are also similar to those in Case 1 (Table 3.2). Measured by the temperature in

the bottom TBL (e.g., 100 km above the CMB), a dominantly degree 2 convective structure is reached with two main downwelling systems (Figure 3.13a). However, unlike in Case 1 where the power spectra of the temperature within the top and bottom TBLs are similar, in Case 3 the temperature in the top TBL has stronger short wavelength structures than that in the bottom TBL. Notice that with $_{lith0} \geq 0.4$, the models would reach a stable, dominantly degree-1 structure, measured from both the top and the bottom temperature fields (e.g., Zhong *et al*., 2007). With the increased Ra, Case 3 has an averaged surface heat flux of ~54 (or 39 TW) and a surface RMS velocity of 7060 (or 3.5 cm/yr). The averaged lower mantle viscosity is 5×10^{21} Pa·s.

Table 3.2. Time-dependent, self-consistent numerical models.

Case	*Ra*	*B*	η_{litho}	Steps	Grid	γ	*Nu*	*Vt*
Case1	5×10^7	0	0.27	30000	12×65^3	50	42	6470
Case2	5×10^7	0.8	0.27	40000	12×65^3	50	26	2580
Case3	1.5×10^8	0	0.3	60000	12×97^3	70	54	7060
Case4	1.5×10^8	0.5	0.3	40000	12×97^3	70	45	5150

Ra, *B*, η_{litho}, and γ stand for Rayleigh number, buoyancy number, viscosity pre-factor in the lithosphere, and internal heating, respectively. Column Steps shows the maximum time steps for the case. The numbers 12 in column Grid means 12 caps divided for the spherical shell, and 65 and 97 mean the resolution for the longitude, latitude, and the radial directions, respectively. *Nu*, and *Vt* are the nondimensional surface heat flux, and surface RMS velocity after the model reaches quasi-steady states

Similar to Case 1, the CMB topography is dominantly degree 2, and is negative/positive below the downwelling/upwelling regions (Figure 3.13c). The surface topography shows strong short wavelength components, and is dominantly degree 3 (Figures 3.13b and 3.5b), following the pattern of the shallow depth temperature structure. The magnitude of the surface and CMB topographies is smaller than that of Case 1 due to a smaller mantle viscosity with the higher Ra for Case 3 (Figure 3.5b). The dominantly degree 2 geoid, dictated by the lower mantle structure, is positive in two broad regions approximately above the upwellings and is negative above the two main downwellings revealed in the bottom TBL temperature (Figures 3.13d and 3.5a). The buoyancy at different depths mostly contributes positively to the surface geoid across the mantle (Figure 3.14e). These results are similar to that for Case 1.

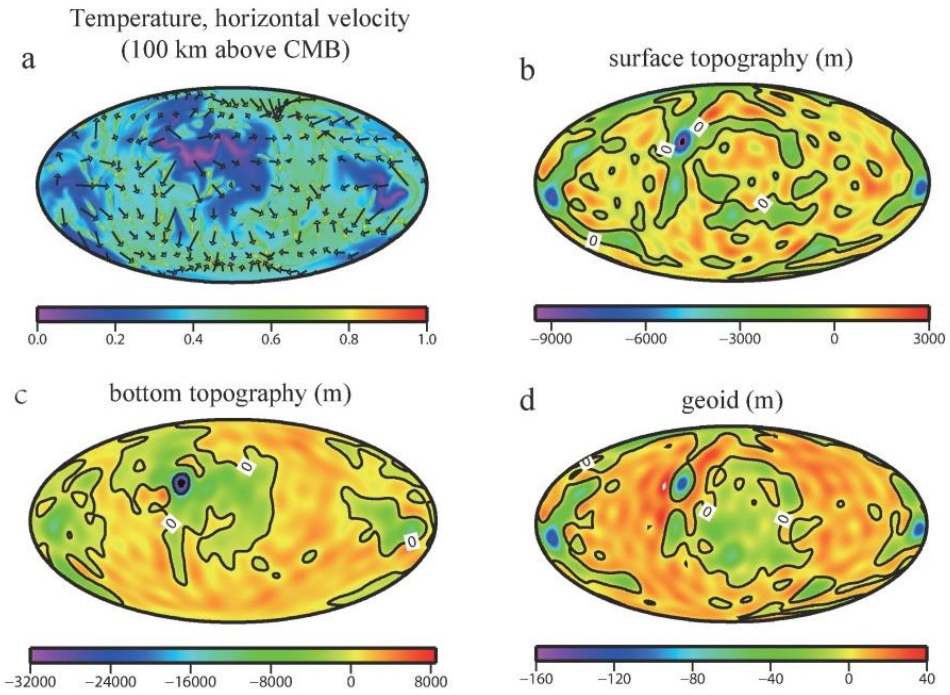

Figure 3.13. (a) The temperature structure at 100 km above the CMB, (b) the surface and (c) the bottom topographies, and (d) the geoid for Case 3. Arrows in (a) denote the horizontal velocities at the corresponding depth. Contour lines of 0 m are plotted in (b)-(d).

The thermochemical model, Case 4, has the same initial temperature and composition conditions as in Case 2, but uses $Ra=1.5\times10^{8}$ and buoyancy number B=0.5. Using the same viscosity pre-factors as Case 3, Case 4 achieves a dominantly degree 2 convective structure. Similar to Case 2, two stable, hot thermochemical piles separated by two cold downwellings are formed (Figure 3.14a) and the piles extend to the height of ~600 km above the CMB. This again suggests that thermochemical piles do not have a significant effect on the dominant convective wavelength that is mainly controlled by viscosity structure. The surface heat flux and RMS velocity of Case 4

are ~32 TW and 2.6 cm/y, respectively. The lower mantle viscosity is 5×10^{21} Pa·s, which is similar with that of Case 3.

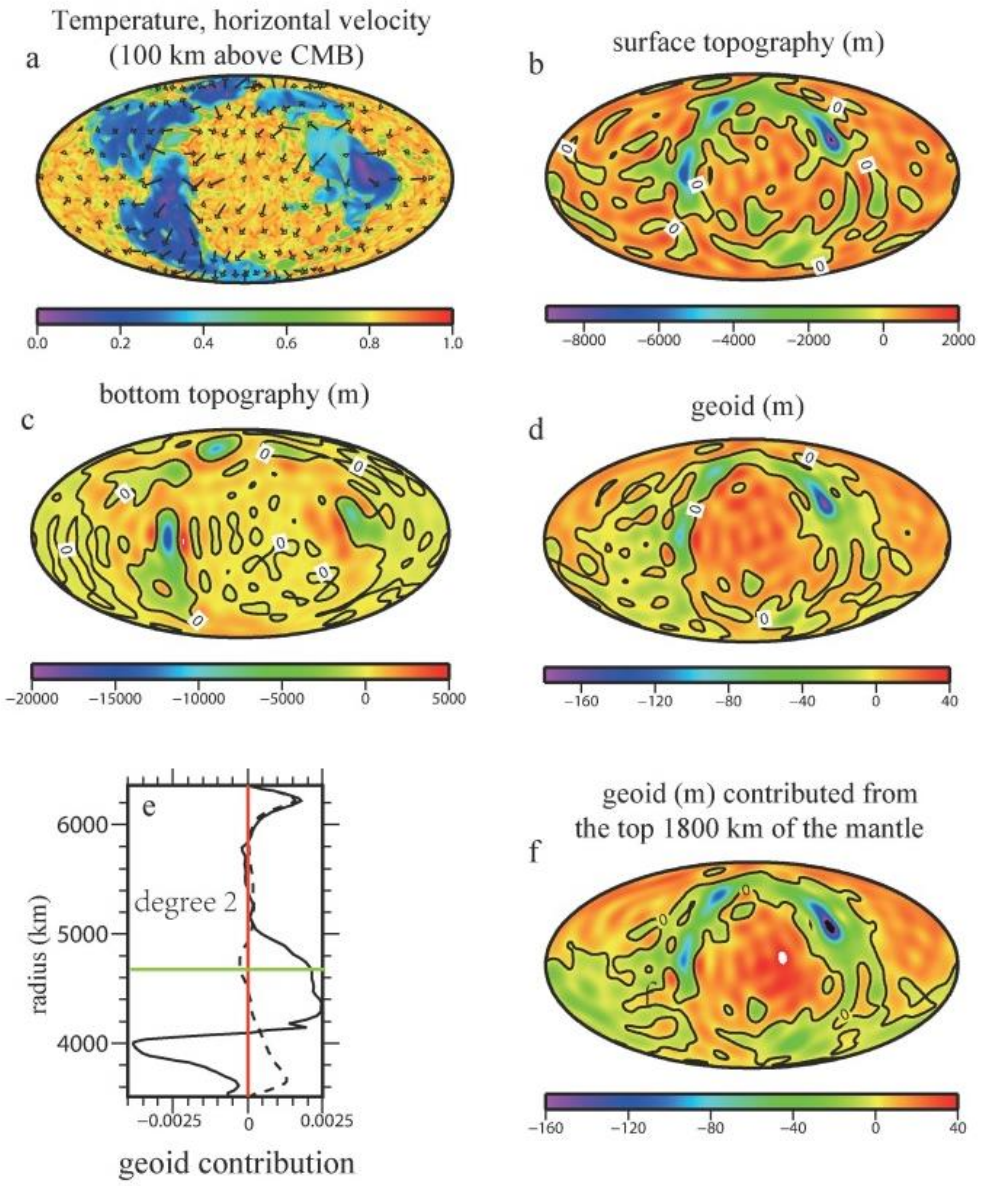

Figure 3.14. (a) The temperature structure at 100 km above the CMB, (b) the surface and (c) the bottom topographies, (d) the geoid, (e) the degree 2 contribution to the total geoid from the layer with unit thickness at different depths, and (f) the geoid from the top 1800 km of the mantle, for Case 4. Arrows in (a) represent the horizontal velocities at the corresponding depth. The black contours in (b)-(d) and (f) are for 0 m contours. In (e), the black dashed line is for degree-2 contribution for Case 3, the red line represents the reference value of 0, and the green line denotes the compensation region for Case 4, below which the net contribution to the total geoid is 0.

The CMB topography for Case 4 (Figure 3.14c) is relatively smooth in the pile regions, with one pile region slightly uplifted and the other one slightly depressed. Similar to Case 2, the lowest CMB topography occurs outside the piles at the center of one downwelling, and the highest topography is also outside the pile regions but near the piles. While the topographies are strongly influenced by the degree 2 convective structure, there are also significant short-wavelength components (Figures 3.14b and 3.14c). The topographies for Case 4 are smaller than those for Case 3 due to the compensation (or buffering) effect by the chemical piles, and are also reduced from Case 2 due to a higher Ra.

The geoid for Case 4 is dominantly degree 2, and is positive in two broad regions approximately over the two chemical piles (Figure 3.14d). The geoid contributed from buoyancy with a unit thickness at different depths, the depth-dependent geoid power spectra and degree-correlations with the total surface geoid are computed, following the same procedures as for Cases 1 and 2. Both the power spectra and degree-correlations are similar to those for Case 2. The layer contribution to the geoid at degree 2 indicates that the bottom ~600 km of the mantle, which is the vertical extent of the chemical piles, contributes negatively to the total geoid, and that the negative contribution is compensated by the positive contribution from the mantle right above the piles (Figure 3.14e). The thickness of the compensation region is ~1100 km at degree 2, similar to that in Case 2. The geoid produced by the top ~1800 km of the mantle resembles the total geoid (Figures 3.14f and 3.14d), and it correlates at 94% and accounts for 114% of the total geoid, summed from degrees 2 to 12. Similar with Case 2, the surface topographies produced before and after removing the bottom part of the mantle are nearly identical (the correlation and contribution for degrees 1-12 are 99.9% and 101.4%, respectively). Based on Cases 2 and 4, we

conclude that for thermochemical convection with heavy thermochemical piles, the bottom layer of the mantle does not have net contribution to the geoid, as well as the surface dynamics topography, and this compensation layer thickness is ~1000 km for the chemical piles extending to ~500 km above the CMB.

3.4 Discussion

3.4.1 The geoid, thermochemical LLSVP, and compensation layer

In this study, we present dynamically self-consistent thermal and thermochemical convection models that generate dominantly degree-2 convective structure at Earth's mantle like Rayleigh number. The degree-2 convective structure from our dynamic models resembles the seismically observed mantle structure and is generated with a depth- and temperature-dependent mantle viscosity structure (e.g., a modestly strong lithosphere) that is consistent with that inferred from post-glacial rebound and geoid studies. These dynamic models allow us to investigate the dynamic effects of thermochemical mantle structure on the long-wavelength geoid and topography anomalies. Our dynamically self-consistent thermochemical convection models show that long-wavelength geoid and topography highs are produced above two chemically distinct and dense piles (Figures 3.9c and 3.9e). This may reconcile the observations of long-wavelength positive geoid and topography anomalies in the Pacific and Africa with the interpretation that the Pacific and Africa LLSVPs are chemically distinct and dense piles (e.g., McNamara and Zhong, 2005b). This also supports the notion that the chemical piles as suggested seismically in the LLSVPs (Masters *et al*., 2000; Wen *et al*., 2001; Ni *et al*., 2002) may represent reservoirs for

primitive mantle materials and also as the source materials for oceanic island basalts (Hofmann, 1997; Boyet and Carlson, 2005).

Our dynamically self-consistent models also show that the thermochemical piles have a compensation effect on the long wavelength geoid, and that the bottom ~1000 km of the mantle (i.e., a compensation layer) has nearly zero net contribution to the total geoid. The relatively thick compensation layer arises because the dense, negatively buoyant chemical piles above the CMB produce negative surface geoid, while the hot, buoyant mantle above the piles generates positive geoid, cancelling the negative geoid from the chemical piles. In our models, the chemical piles reach to 400-500 km height above the CMB, and the thickness of the compensation layer is about 1000-1200 km or 2-3 times of the pile thickness. The compensation thicknesses in our study are determined based on the degree 2 geoid. While degree-2 geoid accounts for >50% of the geoid in both the observation and our models, the degree 3 geoid is also significant. Our dynamic models indicate that similar compensation effect also exists at degree 3 (Figure 3.10c), but the effect is not as evident and robust as that for the degree 2. For example, for Case 2 with $Ra=5\times10^7$, the degree 3 compensation thickness ranges between 250 km and 500 km at different time steps.

It has been a challenge to construct mantle buoyancy structure from the seismic tomographic models for a chemical heterogeneous mantle, because of the uncertainties in mantle seismic, composition and mineral physics models. For example, Forte and Mitrovica (2001) suggested a limited role of composition in affecting seismic and density anomalies of the LLSVPs and concluded that the LLSVPs needed to be overall buoyant to fit the geoid. However, buoyant LLSVPs would not be in dynamic equilibrium with the ambient mantle to stay in the deep mantle as chemically distinct, possibly primitive mantle reservoirs. In their studies on

the geoid and true polar wander, to consider possible chemical effects of the LLSVPs, Steinberger & Torsvik (2010) simply removed the bottom 300 km of the mantle where the LLSVPs are. Clearly, the results on the geoid and compensation thickness from our time-dependent dynamic models differ significantly from these two studies based on instantaneous mantle flow. The compensation effect revealed from our dynamic models may offer an approach to construct mantle buoyancy structure from seismic models for calculating the geoid. That is, we may ignore mantle buoyancy in the compensation layer and only consider the upper part of the mantle (e.g., the top 1800 km). This approach avoids determining the conversion from seismic anomalies to buoyancy structure in the LLSVPs where seismic anomalies have both thermal and chemical origins. It should be pointed out that although reaching to >600 km heights above the CMB, the LLSVPs have the largest seismic anomalies (>5%) only in the bottom ~300 km with a non-uniform structure (e.g., Wang and Wen, 2004; He and Wen, 2012). This suggests that although our dynamic models suggest a reasonable estimate of the compensation thickness of ~1000 km, its exact thickness for the earth's mantle is still somewhat uncertain, possibly ranging from 600 km to 1200 km.

3.4.2 Surface topography, dynamic topography, and the geoid

It is important to point out that surface topography presented in this study (e.g., Figure 3.4c) differs from the classic definition of dynamic topography. Dynamic topography is often defined as the topography caused by the mantle buoyancy excluding that from shallow depths (i.e., the lithosphere), revealing the dynamics of the mantle interiors (e.g., Hager and Richards, 1989). With the classic definition, the subsidence caused by the plate cooling is not considered as dynamic topography. The surface topography in this study, on the contrary, is computed from the buoyancy structure of the whole mantle including the top thermal boundary layer (i.e., TBL or

the lithosphere). Therefore, although the positive surface topography in our models is 3-4 km (e.g., Figures 3.4c and 3.9c), it should not be interpreted as a 3-4 km dynamic topography.

It is of interest to explore the surface dynamic topography of convective models using the classic definition. We will use Case 2 as an example. The top TBL of Case 2, determined from the horizontally averaged temperature (Fig 3.3a), is ~170 km thick. Figures 3.15a and 3.15b present the large-scale (i.e., the degrees 2 and 3) surface topography with and without the contribution from the top TBL, respectively. Note that the surface topography in Figure 3.15a is essentially the long-wavelength components of that in Figure 3.9c, while Figure 3.15b shows the dynamic topography in its classic definition. The dynamic topography is in a range of ±1.5 km, and is only half of the surface topography. That is, the top TBL contributes ~50% of the surface topography. However, the top TBL does not significantly influence the geoid (Figures 3.15c and 3.15d), contributing ~15% of the total geoid at degrees 2 and 3. This reflects the fact that the buoyancy at shallow depths is largely compensated with little effect on the geoid (e.g., Hager and Richards, 1989).

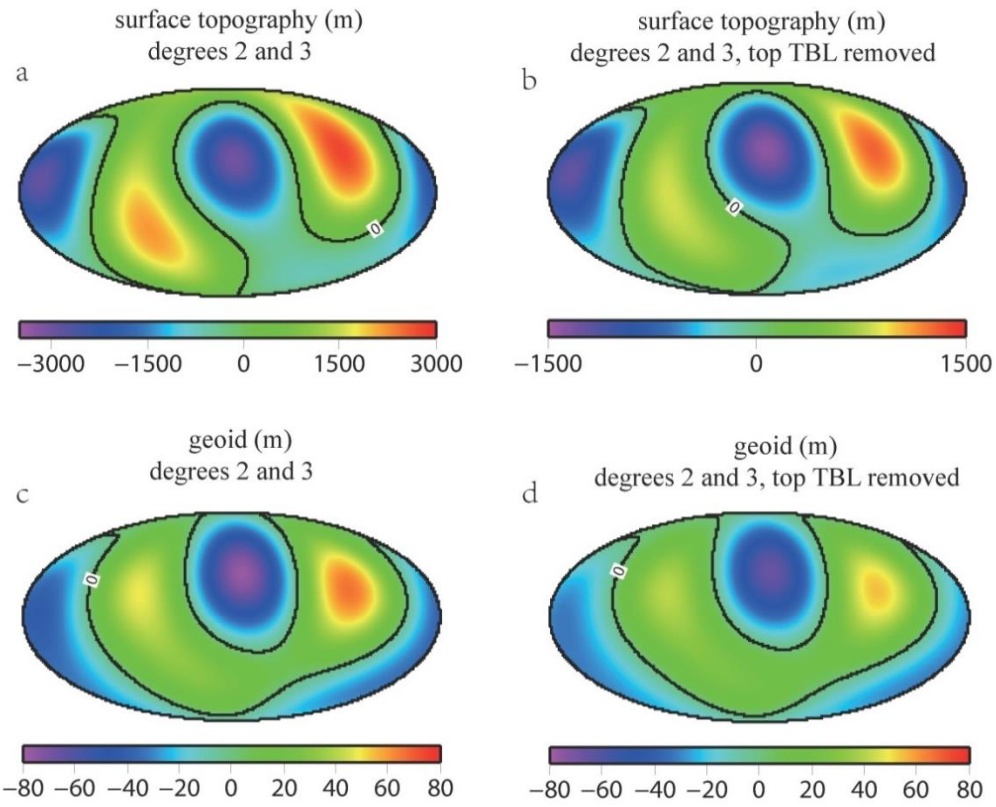

Figure 3.15. The degrees 2 and 3 surface topography for Case 2 (a) with and (b) without the contribution from the top 170 km thick thermal boundary layer, and the geoid (c) with and (d) without the contribution from the top thermal boundary layer. Surface topography in Figure 15b is the dynamic topography in its classic definition. Contour lines of 0 are plotted on (a)-(d).

A similar analysis is done for other cases. For example, for Case 1, the long-wavelength dynamic topography (i.e., degrees 2-3) ranges from -1.5 km to 1 km, and the top 160 km TBL contributes ~60% to the surface topography. The dynamic topography for Case 4 is ~ ±700 m, and its 150 km thick top TBL contributes ~40% at degrees 2 and 3 to the total surface topography. The results further show that the surface topography and the dynamic topography are smaller for models with a larger Ra (i.e., smaller viscosity). It should be pointed out that in its classic definition, the

dynamic topography of both purely thermal and thermochemical cases in our study is in a range of ± 1 km, which is comparable to that inferred from seismic models (e.g., Hager and Richards, 1989; Lithgow-Bertelloni and Silver, 1998), suggesting that our models use reasonable model parameters.

3.4.3 CMB topography

Our dynamic models show that the CMB topography is distinctly different between purely thermal and thermochemical convection models. In purely thermal convection, the CMB topography shows variations at all different scales that correspond directly to mantle convective structure (e.g., Figures 3.4d and 3.13c). For example, in the upwelling regions, short-wavelength positive CMB topography with large amplitude below localized mantle plumes superposes on long-wavelength positive topography. However, for thermochemical convection, CMB topography in the chemical pile (i.e., upwelling) regions is extremely smooth and is nearly zero or slightly depressed/uplifted (Figures 3.9d and 3.14c), although the piles are chemically dense with net negative buoyancy (Figure 3.11b). However, the CMB topography varies significantly and rapidly outside the pile regions where both the largest uplift and the largest depression occur. While the largest uplift occurs at the vicinity of the chemical piles, the largest depression is underneath the coldest downwellings. This is generally consistent with previous modeling studies using a similar mantle viscosity structure but imposed plate motions (Lassak *et al*., 2010). For Case 4 with Earth-like convective vigor, the largest positive and negative CMB topography are about 4 km and -10 km, respectively, and they exist over relatively small length-scales (hundreds of kilometers) (Figure 3.14c). Recent analyses of short period PcP seismic waves suggest up to 6 km depression of the CMB beneath Kenai Peninsula over several hundred kilometer length-scales (Wu *et al*., 2014). Similar future seismic studies on

the short-wavelength CMB topography may provide constraints on mantle dynamic models.

3.4.4 The effects of 3-D viscosity on the geoid

Geoid modeling studies often assume an 1-D viscosity structure (e.g., Hager and Richards, 1989), because the simplified viscosity allows the use of the propagator matrix method to compute the geoid, making it possible for efficiently sampling model parameter space and inversion (e.g., King and Masters, 1992). However, there has been a concern on how the simplified 1-D viscosity structure may introduce errors in the geoid for the mantle with 3-D viscosity (e.g., Richards and Hager, 1989). For 3-D viscosity inferred from seismic tomography models, it seems that the effects from 3-D viscosity or lateral variations in viscosity (i.e., LVV) are only important at wavelengths smaller than those corresponding to spherical harmonic degree 4 (Zhang and Christensen, 1993). This is generally consistent with other similar studies (Moucha *et al*., 2007; Ghosh *et al*., 2010). However, Zhong and Davies (1999) indicated that the effect of LVV is dependent on mantle structure itself. For example, it was found that 3-D viscosity derived from slab models could affect degree-2 geoid (Zhong and Davies, 1999).

It is of interest to examine the effect of 3-D viscosity or LVV on the geoid for dynamically self-consistent convection models such as those in this study. To address this issue, we compute the geoid using the buoyancy structure of our convection models but with a horizontally averaged viscosity (i.e., 1-D) structure (e.g., Figure 3.3c) and compare the resulting geoid with the geoid using 3-D viscosity. We use Case 2 as an example for our analysis, but the results for other cases are similar. The geoid kernels for degrees 2-20 are computed for 1-D viscosity structure for Case 2 (Figure 3.3c) using a propagator matrix method (e.g., Hager and O'Connell, 1981)

(Figure 3.16c). These geoid kernels are similar to those from Hager and Richards (1989), except in the upper mantle. The difference is mainly caused by the lack of a weak asthenosphere from 100 km to 400 km depths in our convection models (Figure 3.3c). The self-gravitational effects and an improved treatment of the boundary conditions at the CMB in our models (see section 3.2.3) also contribute to the difference.

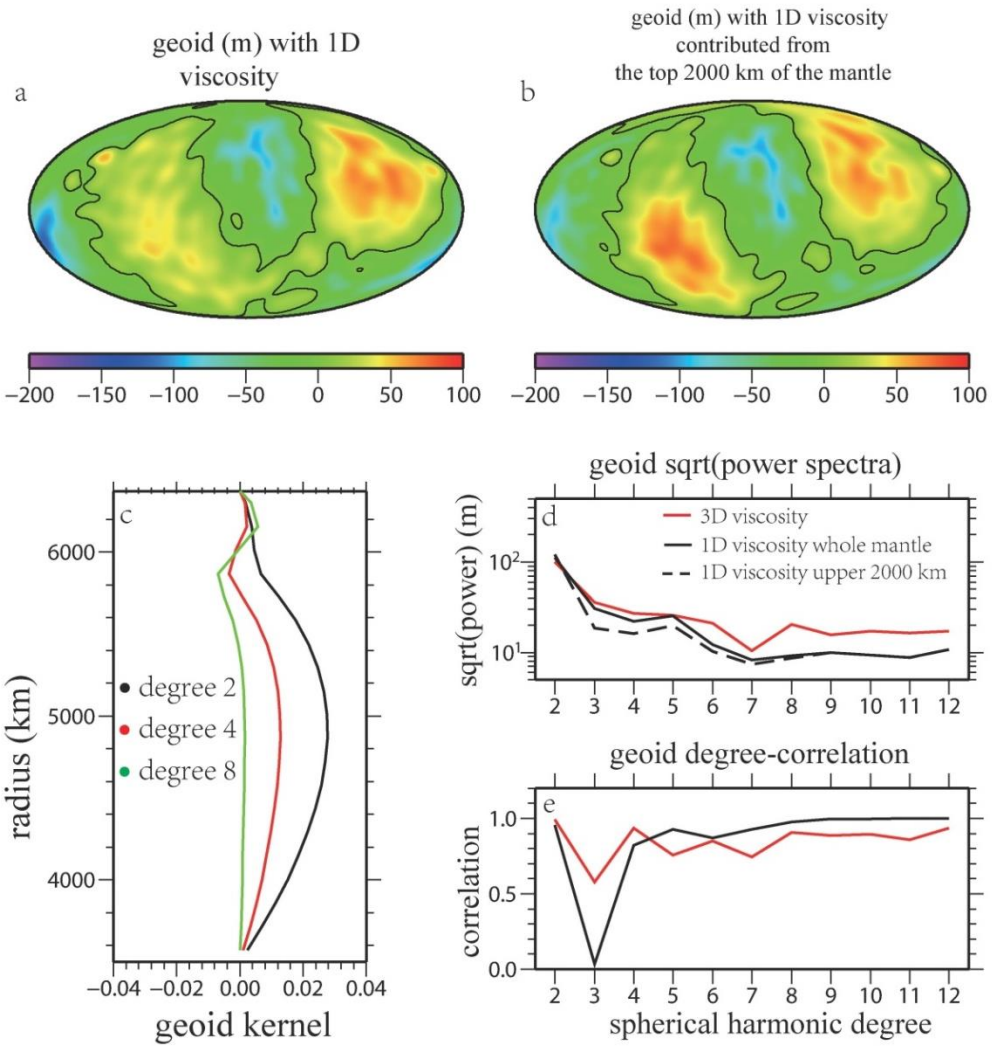

Figure 3.16. The geoid for Case 2 with 1-D viscosity contributed from (a) the whole mantle and (b) the top 2000 km of the mantle (i.e., excluding the bottom 900 km), (c) the geoid kernels for degrees 2 (black), 4 (red), and 8 (green) for the 1-D viscosity profile, (d) the square root of the geoid power spectra for degrees 2-12 for the original geoid with 3-D viscosity (i.e., Figure 3.9e) (red line), the geoid in Fig 3.16a (black solid line), and the geoid in Figure 3.16b (the black dashed line), and (e) the degree-correlation for degrees 2-12 between the original geoid with 3-D viscosity and the geoid in Figure 3.16a (red line), and the correlation between the geoid in Figure 3.16a and the geoid in Figure 3.16b (black line). The 1-D viscosity is the horizontally averaged viscosity of the selected snapshot of Case 2 (Fig 3.3c).

The geoid kernels are convolved with buoyancy for Case 2 (e.g., Figures 3.10d and 3.11) to compute the geoid. The resulting geoid with 1-D viscosity, H_{1D}, (Fig 3.16a) shows a similar degree-2 pattern to the original geoid of Case 2 with 3-D viscosity, H_{3D}, (Figure 3.9e). The power spectra of H_{1D} and H_{3D}, as well as their degree-correlations are shown in Figures 3.16d and 3.16e, respectively. While the two geoids agree very well at degree-2, significant difference exists at short-wavelengths for degrees 6 and up especially for the amplitude. At degrees 3 and 4, the amplitudes of the geoid from H_{1D} are smaller than those from H_{3D} by 14% and 18%, respectively, but the degree-correlation at degree 3 is smaller than 0.6. Because of the degree-2 dominance, the total degree-correlation for degrees 2-12 between H_{1D} and H_{3D} is 92% and the total amplitude of H_{1D} is 90% of H_{3D}. The results suggest that the degree-2 geoid is not affected by LVV, consistent with what has been suggested for seismically based geoid models (e.g., Zhang and Christensen, 1993; Moucha *et al*., 2007; Ghosh *et al*., 2010). However, the effect of LVV may remain significant for shorter wavelengths even for degree-3, further confirming that the effect of LVV is dependent on buoyancy/viscosity structure (Zhong and Davies, 1999).

We now go back to the compensation effect caused by heavy chemical piles for the model with 1-D viscosity. We repeat the geoid analysis for Case 2 using the 1-D viscosity (Figure 3.3c) and the geoid kernel approach, and find that the degree-2 geoid compensation effect still exists but with a compensation layer thickness of 900 km, instead of 1200 km for the original Case 2 with 3-D viscosity. The geoid using the 1-D viscosity but with the bottom 900 km of the buoyancy structure removed (Figure 3.16b), H_{1DR}, agrees with the geoid with the whole mantle buoyancy, H_{1D} (Figure 3.16a), except at degree-3 where the degree-correlation is poor (Figure 3.16e). This suggests that the compensation effect observed in the numerical models with 3-D

viscosity also stands in geoid models with 1-D viscosity, and, to the first order, can be analyzed using 1-D viscosity geoid models.

3.4.5 Some potential drawbacks of the model

Our study represents the first attempt to investigate the geoid for thermochemical mantle convection based on dynamically self-consistent models with a number of important features that are relevant for the present-day's Earth mantle, including degree-2 dominant structure, temperature- and depth-dependent viscosity, and chemically distinct LLSVPs. However, our models also fall short to incorporate some other features that may be potentially important for understanding the geoid. For example, tectonic plates do not emerge from our models (see discussion in section 3.2.2). Therefore, our models, even if they display dominantly degree-2 convective structure, do not have linear plate boundaries with localized deformation nor sheet-like downwellings (i.e., subducted slabs). Future studies are needed to examine the effects of tectonic plates on our results. In spite of recent progress in modeling mantle convection with tectonic plates (e.g., Moresi and Solomatov, 1998; Coltice *et al*., 2012), this type of modeling remains a significant challenge due to our poor understanding of lithospheric rheology (e.g., Zhong and Watts, 2013).

Our models do not produce positive geoid anomalies over cold downwellings. However, the Earth has geoid highs both over Africa and Pacific at degrees 2 and 3 originated from the long-wavelength lower mantle structure, and over subduction slabs, at wavelengths corresponding to degrees 4 to 9 (e.g., Hager & Richards, 1989). In the Pacific, the geoid high over subduction zones is likely influenced by both subduction and lower mantle structures, and radial viscosity profile across the mantle as well as regional rheological structure might play a role. Assuming an 1-D viscosity structure, Hager (1984) showed that the geoid highs over subduction zones and also

on global scale could be reproduced with a viscosity jump of a factor of 30 at the 670 km depth. Moresi and Gurnis (1995) demonstrated that for subducted slabs with higher viscosity than the ambient mantle as expected from temperature-dependent viscosity, a larger viscosity contrast (~60-200) at the 670 km depth would be required to reproduce regional geoid high over subduction zones in the western Pacific. Recently, Hines & Billen (2012) suggested that due to yielding induced lateral variations of viscosity within slabs, the geoid over subduction zones might be only sensitive to local rheological structure (e.g., the mantle wedge). Our models, while produce long-wavelength mantle structure (e.g., degree-2), do not have sheet-like slabs, and this makes it difficult to account for the subduction zone geoid as observed. Future studies should explore models explaining the geoid at both global (i.e., degrees 2-3 for the LLSVPs) and regional scales (i.e., subduction zones) in Earth-like dynamically self-consistent models.

Phase changes are not included in our numerical models. The phase changes in the upper part of the mantle, i.e., the olivine to spinel phase change at 410 km depth and spinel to post-spinel phase change at 660 km depth, may not affect significantly the large scale mantle dynamics, especially in the lower mantle, given that the Clapeyron slope of the post-spinel phase change is only ~ -2.5 MPa/K (e.g., Fukao *et al*., 2009). The post-perovskite (pPv) phase change occurs in the relatively cold slabs several hundred kilometers above the CMB and could potentially affect the lower mantle structure (e.g., Sidorin *et al*., 1999; Murakami *et al*., 2004; Garnero and McNamara, 2008; Tosi *et al*., 2009). The pPv phase change would increase the negative buoyancy of the slabs, and may weaken the slabs. However, its overall dynamic effect on the dynamics of thermochemical piles in the CMB regions is relatively minor (e.g., Li *et al*., 2014b). We think that the effect of the pPv phase

change on our results may be compensated by increasing slightly buoyancy number *B* for thermochemical piles in our models.

Finally, our models do not consider the effects of secular cooling including the cooling of the mantle and core, which leads to time-dependent Ra. However, we think that these effects are likely small on our results. The secular cooling is on a much longer time scale (e.g., at a cooling rate of ~70 K per Ga for the mantle for the last 3 Ga [Jaupart *et al*., 2007]) than that for convective mantle structure change (Figure 3.2b) [Zhong *et al*., 2007].

3.5 Conclusion

We have computed a series of 3-D spherical convection models for both purely thermal and thermochemical convection. These dynamically self-consistent models include temperature- and depth-dependent viscosity. By varying the lithosphere viscosity, these models achieve a stable degree-2 dominant convective structure that is similar to the present-day Earth's mantle. We computed the geoid anomalies and analyzed the geoid contributed from the buoyancy structure at different depths from these models. The results can be summarized as follows:

1. Our dynamically self-consistent thermochemical convection models show that degree-2 positive geoid anomalies can be produced over chemically dense piles, which suggests that the positive long-wavelength geoid anomalies observed in the Pacific and Africa are consistent with the interpretation of the two LLSVPs as chemically dense, possibly primitive thermochemical piles. However, our degree-2 purely thermal convection models also produce positive geoid anomalies over the two

major upwelling systems, consistent with previous studies of the geoid in isochemical, whole-mantle models using buoyancy derived from seismic models.

2. Our dynamic models show that the chemically dense piles have a compensation effect on the surface geoid, resulting in a compensation layer at the bottom of the mantle that is 2 to 3 times as thick as the chemical piles or ~1000 km thick. The buoyancy in the compensation layer has zero net contribution to the surface geoid.

3. Thermochemical piles in our dynamic models have a passive and secondary effect on large-scale convective structure that is controlled by mantle viscosity structure and convection above the thermochemical piles.

4. The CMB topography is smooth and slightly negative in the regions with thermochemical piles, but significant and rapid variations in CMB topography occur outside the chemical pile regions where both the largest depression and uplifts at the CMB are found. The largest CMB depression is always under major downwellings, but the largest uplift at the CMB is near the chemical piles.

5. The 3-D viscosity or lateral variations in viscosity may not affect degree-2 geoid, but may influence shorter wavelength geoid. Our results further confirm that the effects of lateral variations in viscosity are dependent on 3-D buoyancy/viscosity structure themselves.

Chapter 4

Constraining mantle viscosity structure for a thermochemical mantle using the geoid observation[3]

Abstract: Long-wavelength geoid anomalies provide important constraints on mantle dynamics and viscosity structure. Previous studies have successfully reproduced the observed geoid using seismically inferred buoyancy in whole-mantle convection models. However, it has been suggested that large low shear velocity provinces (LLSVPs) underneath Pacific and Africa in the lower mantle are chemically distinct and are likely denser than the ambient mantle. We formulate instantaneous flow models based on seismic tomographic models to compute the geoid and constrain mantle viscosity by assuming both thermochemical and whole-mantle convection. Geoid modelling for the thermochemical model is performed by considering the compensation effect (Liu & Zhong, 2015) of dense thermochemical piles and removing buoyancy structure of the compensation layer in the lower mantle. Thermochemical models well reproduce the observed geoid, thus reconciling the geoid with the interpretation of LLSVPs as dense thermochemical piles. The viscosity structure inverted for thermochemical models is nearly identical to that of whole-mantle models. In the preferred model, the lower mantle viscosity is ~10 times higher than the upper mantle viscosity that is ~10 times higher than the transition zone viscosity. The weak transition zone is consistent with the proposed high water content there. The geoid in thermochemical mantle models is sensitive to seismic structure at mid-mantle depths, suggesting a need to improve seismic

[3] This chapter was published as "Liu, X., and S. J. Zhong, 2016. Constraining mantle viscosity structure for a thermochemical mantle using the geoid observation, *Geochem. Geophys. Geosyst*., **17**, doi:10.1002/ 2015GC006161"

imaging resolution there. The geoid modelling constrains the vertical extent of dense and stable chemical piles to be within ~500 km above CMB. Our results have implications for mineral physics, seismic tomographic studies, and mantle convection modelling.

4.1. Introduction

The geoid modelling using instantaneous mantle flow models based on seismic velocity anomalies can provide a critical constraint on the mantle rheology and buoyancy structure. Classic studies using this approach and assuming a whole-mantle, purely thermal convection model (e.g., Hager & Richards, 1989; Ricard *et al*., 1993; King and Masters, 1992; King, 1995; Mitrovica and Forte, 2004; Ghosh *et al*., 2010) have estimated that the viscosity in the lower mantle is about 30-60 times higher than that in the upper mantle. However, those models may have been over-simplified, because the large-scale lower mantle structures exhibit complex seismic characteristics which may imply compositional heterogeneities (e.g., Su and Dziewonski, 1997; Masters *et al*., 2000; Wen *et al*., 2001; Ni *et al*., 2002; He and Wen, 2009). For example, the large low shear velocity provinces (LLSVPs) in the lower mantle (Figure 4.1a) have been proposed as chemically distinct and stable piles (e.g., Wen *et al*., 2001; Ni *et al*., 2002) that help reconcile both seismic and geochemical observations (e.g., Hofmann, 1997; Kellogg *et al*., 1999; Kunz *et al*., 1998; Boyet and Carlson, 2005; Jackson *et al*., 2014), although some studies suggest that the LLSVPs have a purely thermal origin (e.g., Davies, 2012). Chemical piles alter the lowermost mantle buoyancy structure and have been found to influence the mantle dynamics (e.g., Tackley, 1998; Kellogg *et al*., 1999; Davaille, 1999; McNamara and Zhong, 2005; Zhang *et al*., 2010) as well as their surface manifestation such as the geoid and dynamic topography (Liu & Zhong, 2015). Thus, it is necessary to re-examine the geoid modelling and its constraint on mantle viscosity considering the effects of the thermochemical mantle convection based on seismic tomographic models.

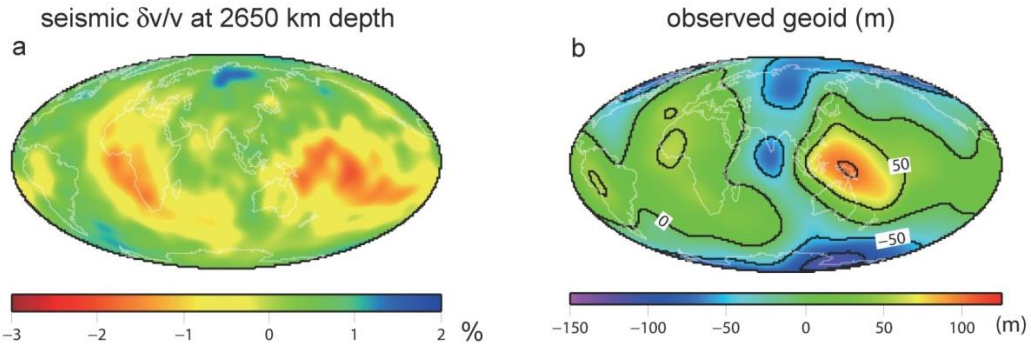

Figure 4.1. (a) Seismic shear wave speed anomaly δv/v (model SAW642ANb) at 2650 km depth, and (b) the observed geoid at degrees 2-12. Contours of 50 m are plotted in (b).

Constructing buoyancy structure from the seismic tomographic models in those chemically heterogeneous regions is difficult due to the mixture of both thermal and compositional effects, and uncertainties in seismic, compositional and mineral physics mantle models. In their geoid modelling study, Steinberger & Torsvik (2010) simply removed the buoyancy structure of the thermochemical layer (i.e., bottom 300 km of the mantle). Another geoid modeling study considering possible chemical effects on mantle buoyancy suggested that the LLSVPs would be overall buoyant in order to fit the geoid (Forte and Mitrovica, 2001), thus raising the question whether the LLSVPs represent stable thermochemical structures over long time scales. In time-dependent, dynamically self-consistent thermochemical mantle convection models, Liu and Zhong (2015) found that the general characteristics of the surface geoid and dynamic topography over stable dense thermochemical piles, after reaching a dynamic equilibrium, resemble the observations. Additionally, Liu & Zhong (2015) showed that dense thermochemical piles have a compensation effect on the geoid such

that the bottom ~1000 km of the mantle (i.e., a compensation layer), or 2 to 3 times of the maximum thickness of the chemical piles, has a zero net contribution to the geoid at long wavelengths. The compensation effect occurs because the geoid anomalies from negatively buoyant chemical piles are offset by those from hot and buoyant normal mantle above the piles. Considering the compensation effect, the geoid modelling for the thermochemical model with stable chemical piles can be done following the same approach as that for whole mantle models (e.g., Hager & Richards, 1989) except that the mantle buoyancy structure in the compensation layer, including the LLSVPs, needs to be removed. The mantle above the compensation layer can be seen as isochemical with buoyancy structure that can be determined from seismic tomographic models with a conversion factor (e.g., Hager & Richards, 1989; Forte & Mitrovica, 2001; Ghosh, *et al.*, 2010).

This study investigates how well the geoid can be explained in instantaneous flow models in which mantle buoyancy structure is derived from seismic tomographic models considering the compensation effect for the thermochemical mantle as reported in Liu & Zhong (2015). This study also re-examines the geoid constraints on mantle viscosity structure for a thermochemical mantle and compares the inverted mantle viscosity with that inferred from previous purely thermal mantle models. The paper is organized as follows. Next section describes the model formulation and procedures, section 3 presents results, and sections 4 and 5 are for discussion and conclusion.

4.2. Models and Procedures

4.2.1. Geoid modelling

The instantaneous flow models are formulated in a 3D spherical geometry. Assuming an incompressible fluid and constant thermodynamic parameters except for the viscosity, the governing equations for the conservation laws of the mass and momentum are:

$$\nabla \cdot \boldsymbol{u} = 0, \tag{4.1}$$

$$-\nabla p + \nabla \cdot [\eta(\nabla \boldsymbol{u} + \nabla^T \boldsymbol{u})] - \delta\rho g \boldsymbol{e}_r = 0\ , \tag{4.2}$$

where $\boldsymbol{u}$ is the velocity vector, p is the dynamic pressure, η is the viscosity, g is the gravitational acceleration, and $\delta\rho$ is the density anomaly.

The density anomaly $\delta\rho$ in equation (4.2) is determined from seismically observed relative shear-velocity anomaly $\frac{\delta v_s}{v_s}$ by:

$$\frac{\delta\rho}{\rho} = c\frac{\delta v_s}{v_s}, \tag{4.3}$$

where ρ is the background mantle density at a given depth from the PREM model (Dziewonski and Anderson, 1981), and *c* is the conversion factor. This study uses three global tomographic models: SAW642ANb (Panning *et al*., 2010), S40RTS (Ritsema *et al*., GJI, 2011), and Smean (Becker and Boschi, 2002). Each seismic model is divided into 20 shells with the identical thickness of 143.5 km, and $\frac{\delta v_s}{v_s}$ is interpolated at the middle depth of each shell with one-degree-by-one-degree grids. Following the previous studies (e.g., Hager and Richards, 1989), we ignore the structure in the top ~280 km of the mantle where large seismic anomalies are significantly affected by compositional or/and anisotropic effects but may not affect the long-wavelength geoid.

The geoid is computed by φ/g, where φ is the surface gravitational potential anomaly and can be solved from the Poisson's equation,

$$\nabla^2\varphi = -4\pi \mathrm{G}\delta\rho \ , \tag{4.4}$$

where G is the gravitational constant, and $\delta\rho$ includes both density variations in the mantle ($\delta\rho$ in equation 4.3) and those associated with dynamic topographies at the surface and CMB. Dynamic topographies are determined from solving equations 4.1 and 4.2 under free-slip boundary conditions at the surface and CMB. The self-gravitation effect is incorporated in this study although the equations presented above did not include this effect for simplicity. With the self-gravitation effect, an additional term, $-\rho\delta g\overrightarrow{\boldsymbol{e_r}}$, should be added to the left side of equation (4.2) where $\delta g = -\nabla\varphi$ is the perturbation to the radial gravity (e.g., Zhong *et al*., 2008). A reduced pressure formulation is used here to solve the momentum equation, dynamic topographies, gravitational potential and geoid with the self-gravitation effect (e.g., Zhang & Christensen, 1993; Zhong *et al*., 2008).

The flow models in this study consider only radially varying viscosity structure, as to be discussed in details later. Consequently, the conservation equations can be solved with a propagator-matrix method (e.g., Hager and Richards, 1989). Details in solving the conservation equations and the Poisson's equation for the geoid and dynamic topographies with the self-gravitation can be found in Zhong *et al*. (2008). In this study the density contrasts at the surface and the CMB are assumed as 3300 kg/m^3 and 4337 kg/m^3, respectively.

The compensation effect revealed from Liu & Zhong (2015) suggests that the long-wavelength geoid is only contributed from the upper part of the mantle above the compensation layer, while the buoyancy structure in the compensation layer can be

ignored. The compensation thickness as inferred from dynamically consistent thermochemical convection models (Liu & Zhong, 2015) varies at different spherical harmonic degrees, and at degree 2 it is estimated to be 2-3 times the thickness of chemical piles. In this study, we assume a uniform compensation thickness at all degrees in thermochemical models based on the estimation at degree 2. This assumption does not affect the overall geoid modeling, given that the geoid is predominantly at degree-2 and the compensation layer resides at the lowermost mantle which has a limited influence on the geoid at shorter wavelengths. The thickness or vertical extent of the LLSVPs is not well constrained, and in particular, there are significant vertical variations in seismic anomalies within the LLSVPs (e.g., Wang & Wen, 2004; He & Wen, 2009). Therefore, a precise knowledge of the compensation thickness is unknown, and in our thermochemical mantle models we consider four possible compensation thicknesses of 430 km, 720 km, 1000 km, and 1500 km.

4.2.2. Constraining the radial viscosity structure and the conversion factor

The instantaneous models use a 1-D, layered viscosity structure. This allows the use of a propagation matrix method to compute velocities, stresses, dynamic topographies and the geoid from kernels (e.g., Hager & O'Connell, 1981), making it possible for efficiently sampling model parameter space. The effects of lateral variations in mantle viscosity on the geoid at long-wavelengths (degrees 2-3) may be secondary to that of vertical variations in viscosity for the present-day mantle structure (Zhang and Christensen, 1993; Moucha *et al*., 2007; Ghosh *et al*., 2010; Liu & Zhong, 2015), although such effects depend on mantle structures (Zhong & Davies, 1999). Geoid modelling studies have utilized various parameterizations for the radial viscosity (e.g., Hager & Richards, 1989; Steinberger & Calderwood, 2006). With a

concern of potential tradeoffs, our models do not employ fine viscosity layering, but only include four viscosity layers that coincide with significant phase transitions and seismic velocity stratifications. The viscosities in the lithosphere (0-100 km depths), the upper mantle (100-410 km depths), the transition zone (410-670 km depths), and the lower mantle (below 670 km) are denoted as η_{lith}, η_{um}, η_{tz}, and η_{lm}, respectively. The geoid is only sensitive to relative viscosity changes between different layers but not to the absolute viscosity (e.g., Hager and Richards, 1989). Since the lithospheric viscosity has a weak impact on the long-wavelength geoid compared with that of mantle viscosities (Thoraval and Richards, 1997), we fix η_{lith} as 20. Recognizing that when assuming an 1D viscosity profile as in this study that cannot include weak plate margins, a weak lithosphere is required in the geoid modelling (e.g., Zhong and Davies, 1999; Ghosh *et al.*, 2010), we treat η_{um}, η_{tz}, and η_{lm} as free parameters while requiring that η_{lm} is larger than η_{lith}, i.e., η_{lm} is larger than 20.

The conversion factor *c* in equation 4.3 can be inferred from mineral physics studies (e.g., Karato, 1993) as well as modeling surface observables (e.g., Forte & Mitrovica, 2001). In this study, *c* is taken as a constant in the whole mantle except for the compensation layer in which *c* is zero, and *c* is treated as the fourth free parameter in our model calculation in addition to the three viscosities.

We have computed the geoid and dynamic topography in a large number of models in which these four free parameters are varied. These four parameters are constrained by fitting the model geoid to the observation. For each group of these four parameters, the model geoid, denoted as *H'*, is computed up to degrees and orders 12, and the fit to the observed geoid, *H*, is measured by the variance reduction (e.g., Ricard *et al.*, 1993):

$$V_{2-12} = 1 - \frac{M_{2-12}}{H_{2-12}}, \tag{4.5}$$

where H_{2-12} is the total power of the observed geoid *H* from degrees 2 to 12 and is computed by

$$H_{2-12} = \sum_{l=2}^{12} \sum_{m=0}^{l} [(H_{cos}^{lm})^2 + (H_{sin}^{lm})^2]. \tag{4.6}$$

M_{2-12} in equation 4.5 is the total power of the difference between the model geoid *H'* and the observed geoid *H* from degrees 2 to 12:

$$M_{2-12} = \sum_{l=2}^{12} \sum_{m=0}^{l} [(H'^{lm}_{cos} - H_{cos}^{lm})^2 + (H'^{lm}_{sin} - H_{sin}^{lm})^2] . \tag{4.7}$$

The degree-correlation $C_{lmin\text{-}lmax}$ between the model and observed geoids is computed by

$$C_{lmin-lmax} = \left[\sum_{l=lmin}^{lmax} \sum_{m=0}^{l} \left(H'^{lm}_{cos} H_{cos}^{lm} + H'^{lm}_{sin} H_{sin}^{lm}\right)\right] / (H'_{lmin-lmax} H_{lmin-lmax})^{1/2}, \tag{4.8}$$

where $H'_{lmin-lmax}$ and $H_{lmin-lmax}$ are the total power of the model and observed geoids, respectively, from degrees *lmin* to *lmax*, and are computed by equation 4.6. Degree-correlation reveals the similarity between the patterns of the model and observed geoids at certain wavelengths.

In our geoid modeling calculations, these four free parameters, i.e., η_{um}, η_{tz}, η_{lm}, and the conversion parameter *c*, are firstly searched in a large parameter space with relatively coarse parameter grids. Guided by the fitting to the observed geoid, i.e., the variance reduction $V_{2\text{-}12}$, the search space is then narrowed down with refined parameter grids to the parameter space for models with large variance reductions, as to be discussed later.

4.3. Results

4.3.1. Results of the geoid models and inverted viscosities

4.3.1.1. Models with restriction $\eta_{tz} \geq \eta_{um}$

Following Hager & Richards (1989), our study starts from models with a strong transition zone, i.e., $\eta_{tz} \geq \eta_{um}$ is pre-constrained in the geoid modelling. The original search space is η_{um} between 0.01 and 10, η_{tz} between 0.1 and 20, and η_{lm} between 1 and 100, respectively. Ten different values with equal spacing in a logarithmic scale are searched for each viscosity parameter. Notice that we require that $\eta_{lm} \geq \eta_{tz} \geq \eta_{um}$. The conversion factor *c* is searched between 0.1 and 0.5 with a uniform spacing of 0.02. For each zoom-in procedure, the 'best-fit' model with the largest variance reduction, $V_{2\text{-}12(max)}$, is identified, and models with variance reduction that is larger than $V_{2\text{-}12(max)}$-5% are considered as acceptable. Two seismic models, SAW642ANb and S40RTS, are used in the zoom-in procedure, and both the whole mantle convection and the thermochemical convection with a 720 km compensation thickness are assumed and tested. The parameter space of those acceptable models defines a starting search space for the next zoom-in procedure.

The zoom-in procedure is done twice, and the parameter space is narrowed down to be η_{um} between 0.1 and 1, η_{tz} between 0.1 and 2.5, and η_{lm} between 10 and 80, with refined intervals of 0.1, 0.1, and 5, respectively. The conversion factor *c* is between 0.22 and 0.34 for the whole mantle models, and 0.30 to 0.42 for the thermochemical models, both with an interval of 0.02. Thousands of models are computed within this parameter space, and their geoid outputs are analyzed. We mostly describe results based on seismic model SAW642ANb as it leads to slightly better geoid fits, but the results including the inverted parameters and the analyses

shown in the following sections for S40RTS and Smean are quite similar (Tables 4.1 and 4.2).

Table 4.1. The best-fit geoid models with restriction $\eta_{tz} \geq \eta_{um}$

		SAW642ANb				S40RTS				SMEAN			
		WM	TC1	TC2	TC3	WM	TC1	TC2	TC3	WM	TC1	TC2	TC3
$V_{2\text{-}12}$ (%)		77.9	75.1	68.7	55.8	69.3	68.2	63.6	55.2	70.1	67.3	62.0	50.5
C (%)	2-12	88.3	86.6	82.9	74.7	83.3	82.6	79.7	74.3	83.8	82.1	78.7	71.1
	2	96.7	96.1	96.4	94.3	93.3	93.1	91.1	84.6	93.3	94.5	91.4	87.4
	3	92.7	94.3	93.8	92.4	90.3	90.5	91.2	92.9	84.9	83.7	84.8	81.9
η	*um*	0.7	0.5	0.7	0.6	0.6	0.5	0.4	0.5	0.5	0.4	0.6	0.5
	tz	0.7	0.5	0.7	0.6	0.6	0.5	0.4	0.5	0.5	0.4	0.6	0.5
	lm	40	30	35	30	35	30	25	25	35	30	35	30
C		0.28	0.32	0.36	0.4	0.26	0.28	0.32	0.38	0.24	0.28	0.32	0.36

WM denotes whole mantle model, and TC1, TC2, and TC3 represent thermochemical models assuming a compensation thickness of 430 km, 720 km, and 1000 km, respectively. $V_{2\text{-}12}$ is the degrees 2-12 variance reduction of the observed geoid. *C* is the degree-correlation with the observed geoid, 2-12 denotes the total correlation from degree 2 to degree 12, and 2 and 3 denote the correlation at degree 2 and degree 3, respectively. η is the radial viscosity, and *um*, *tz*, and *lm* denote the upper mantle, the transition zone, and the lower mantle, respectively. *c* is the conversion factor from seismic velocity to density anomaly.

For the whole mantle models, the largest variance reduction $V_{2\text{-}12}$ is 78%, and in this best-fit model (Figure 4.2a), η_{um}, η_{tz}, η_{lm}, and c are 0.7, 0.7, 40, and 0.28, respectively. For all the models with $V_{2\text{-}12} > 73\%$, η_{tz} is mostly equal to or slightly larger than η_{um}, and the viscosity ratio between the lower mantle and the upper mantle is 40-200. Similar viscosity profiles are inferred from the thermochemical models, but a larger conversion factor is needed for fitting the geoid. The largest variance reduction for thermochemical models with a 720 km compensation thickness (Figure 4.2b) is 69%, and η_{um}, η_{tz}, η_{lm}, and c for this model are 0.7, 0.7, 35, and 0.36, respectively. Viscosity profiles for models with $V_{2\text{-}12}$ larger than 64% is illustrated in Figure 4.3a. The variance reduction for thermochemical models is generally smaller than that of whole mantle models, and decreases with increasing compensation thickness (Table 4.1).

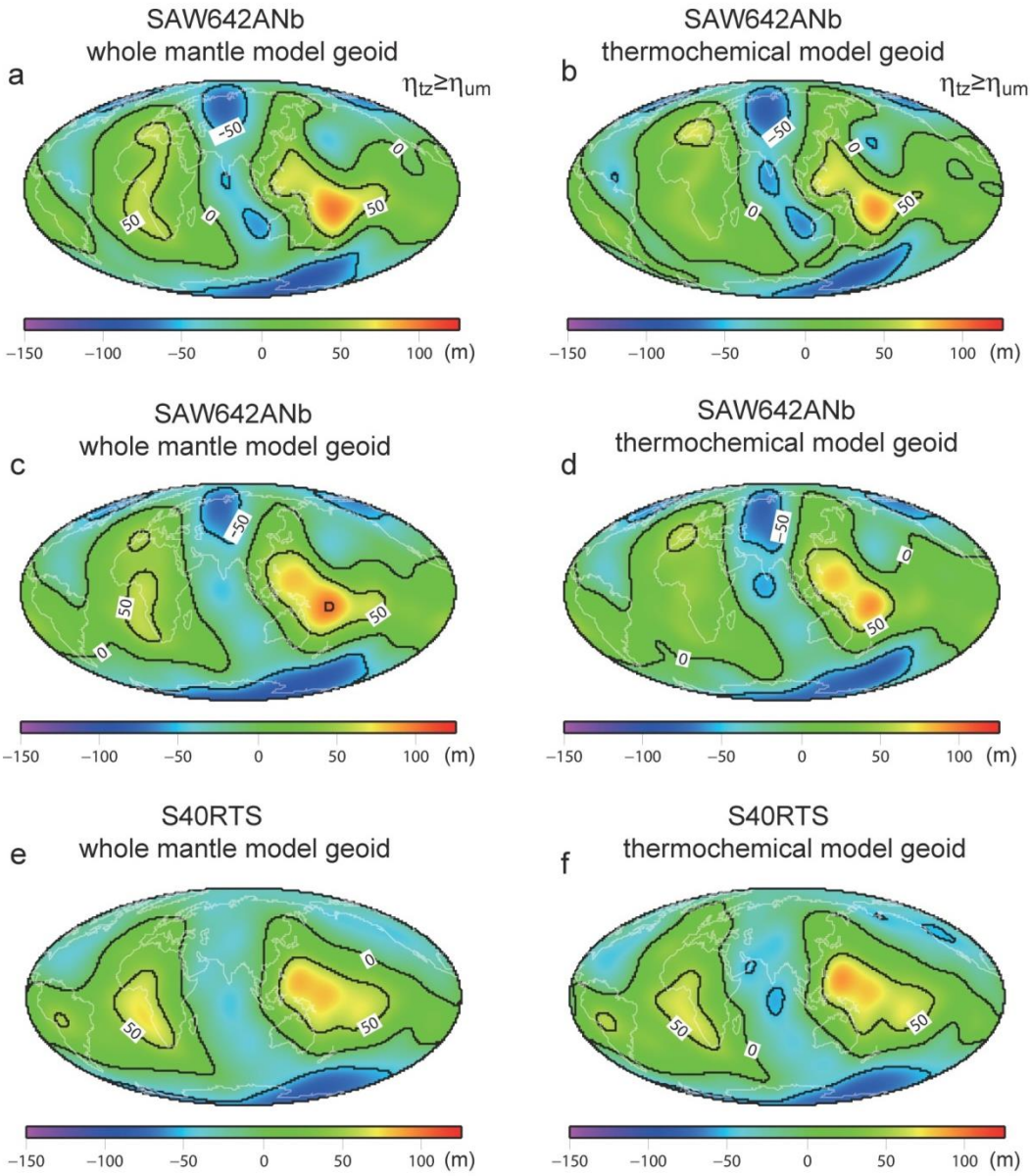

Figure 4.2. The best-fit model geoids computed up to degrees and orders 12 using seismic models (a)-(d) SAW642ANb, and (e)-(f) S40RTS. (a), (c), and (e) are for whole mantle convection models, and (b), (d), and (f) are for thermochemical convection models with a 720 km thick compensation layer. (a) and (b) are for models with restriction $\eta_{tz} \geq \eta_{um}$, while (c)-(f) do not have the restriction. Contours of 50 m are plotted in (a)-(f).

Our inverted viscosity contrast η_{lm}/η_{um}~50 is quite similar to that inferred from geoid studies assuming a single viscosity layer for the upper mantle and transition zone (i.e., $\eta_{tz}=\eta_{um}$) (e.g., Hager *et al*., 1985). However, with the $\eta_{tz} \geq \eta_{um}$ restriction in the inversion, the fact that in models with a large variance reduction η_{tz} is equal or close to η_{um} (Figure 4.3a) suggests that a weak transition zone, i.e., $\eta_{tz}<\eta_{um}$, needs to be considered. Therefore, we conduct an inversion without the restriction between η_{tz} and η_{um}.

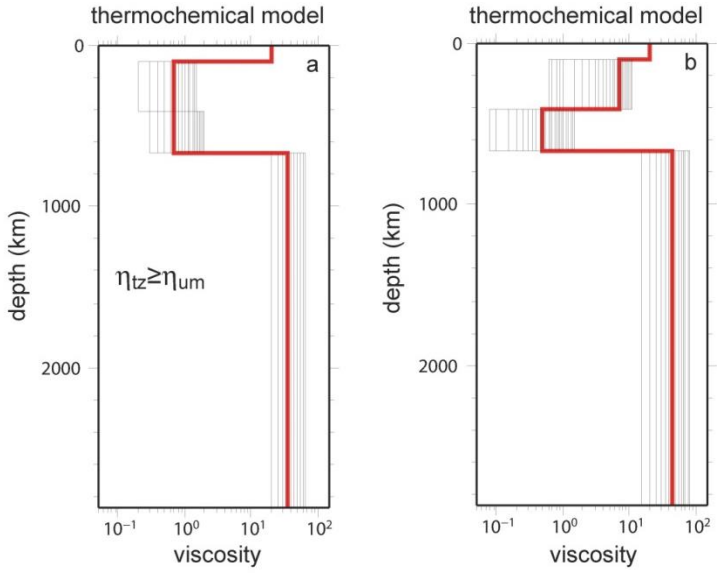

Figure 4.3. Viscosity profiles of thermochemical convection models with a 720 km thick compensation layer. (a) Models with restriction $\eta_{tz} \geq \eta_{um}$ that has a variance reduction larger than 64%, and (b) models without restriction $\eta_{tz} \geq \eta_{um}$ that has a variance reduction larger than 74%. Red lines denote the best-fit models.

4.3.1.2. Models without restriction $\eta_{tz} \geq \eta_{um}$

Without restriction on η_{tz} and η_{um}, the original search space is same as that employed in section 4.3.1.1, except that the space for η_{tz} is expanded as from 0.01 to

20. The zoom-in procedure is done twice, and the final guided search space is 0.1 to 12 for η_{um}, 0.02 to 1.5 for η_{tz}, and 10 to 80 for η_{lm}. The interval for η_{um} is 0.1 between 0.1 to 1, and 0.5 between 1 to 12, respectively, the interval for η_{tz} is 0.02 between 0.02 to 0.1, and 0.05 between 0.1 to 1.5, respectively, and the interval for η_{lm} is uniformly 5. Assuming the whole mantle convection, the best-fit model (Figure 4.2c) has a variance reduction $V_{2\text{-}12}$ of 83% (Table 4.2), with mantle viscosities of 7, 0.45, and 50 for the upper mantle, the transition zone, and the lower mantle, respectively, and a conversion factor of 0.32. Notice that all the models with $V_{2\text{-}12}$ larger than 78% have a weaker transition zone than the upper mantle. The degree-correlations with the observed geoid at degrees 2 and 3 for the best-fit geoid, C_2 and C_3, are 99% and 95%, respectively, implying a nearly perfect reproduction of the long wavelength geoid.

Table 4.2. The best-fit geoid models without restriction $\eta_{tz} \geq \eta_{um}$

		SAW642ANb					S40RTS				SMEAN			
		WM	TC1	TC2	TC3	TC4	WM	TC1	TC2	TC3	WM	TC1	TC2	TC3
$V_{2\text{-}12}$ (%)		83.4	81.3	76.6	64.8	32.8	80.0	80.1	77.3	70.0	80.8	79.7	77.0	69.2
C	2-12	91.3	90.2	87.6	80.5	57.3	89.5	89.5	87.9	83.9	89.9	89.3	87.7	83.7
(%)	2	98.7	98.4	98.2	95.1	53.6	96.2	96	93.8	88.8	97.0	96.4	94.6	90.4
	3	94.5	95.5	95.7	93.7	83.8	93.2	93.6	94.4	95.1	89.3	90.3	91.1	91.3
H	*Um*	7	6.5	7	6	7	6	5	6	2	10	9	4	5
	Tz	0.45	0.45	0.5	0.5	0.5	0.1	0.08	0.08	0.06	0.15	0.15	0.1	0.1
	Lm	50	45	45	40	45	30	25	25	15	45	40	25	25
C		0.32	0.36	0.42	0.5	0.4	0.3	0.36	0.42	0.48	0.3	0.36	0.42	0.48

TC4 represent thermochemical models assuming a compensation thickness of 1500 km. Other symbols and notations are same with those in Table 4.1.

For whole mantle convection models, we identified a large number of models with different viscosity structures that lead to similarly good variance reduction. For models with a very large variance reduction (V_{2-12} > 80%), the viscosities for the upper mantle, η_{um}, and transition zone, η_{tz}, range from 0.5 to 11, and 0.1 to 1.2, respectively, and the lower mantle viscosity η_{lm} is between 20 and 80. For those models, viscosity ratios, η_{tz}/η_{um} and η_{lm}/η_{um}, range from 0.02 to 0.45, and 4.5 to 42, respectively. Viscosity ratios for models with a large variance reduction show a consistent trend and η_{tz}/η_{um} varies proportionally with η_{lm}/η_{um} (Figure 4.4a). The viscosity contrast at the 670 km depth, η_{lm}/η_{tz}, for these models with a large variance reduction falls in a narrow range between 60 and 250. Most of the acceptable models have c=0.32.

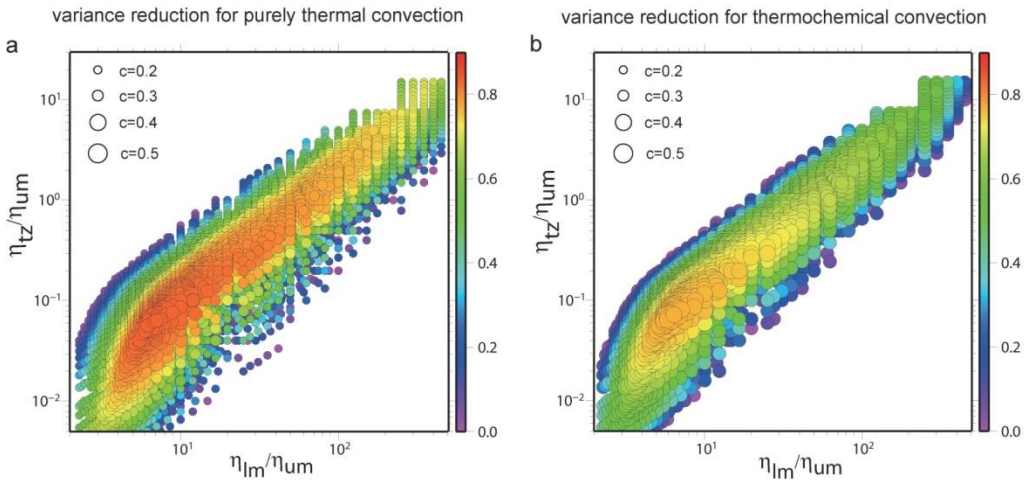

Figure 4.4. The variance reduction of the geoid in the logarithmic scale for (a) the whole mantle model and (b) the thermochemical model assuming a 720 km thick compensation layer, based on the seismic model SAW642ANb. Horizontal and vertical axes are the viscosity ratios of the lower mantle over the upper mantle and of the transition zone over the upper mantle, respectively. The color and size of the circles indicate the variance reduction and the conversion factor, respectively. In (a) and (b), for each radial viscosity profile, only the model with a conversion factor that best reproduces the observed geoid is plotted.

The inversion is performed for thermochemical models considering the compensation effect. Calculations are done with different compensation thicknesses of 430 km, 720 km, 1000 km, and 1500 km. Except for models with a 1500 km thick compensation layer, thermochemical models reproduces the observed geoid well (Figure 4.2d). For models with a 720 km thick compensation layer, the variance reduction $V_{2\text{-}12}$ for the best-fit model is 77% (Table 4.2). $V_{2\text{-}12}$ for the best-fit model decreases with increasing compensation layer thickness (Table 4.2), similar to calculations with restriction $\eta_{tz} \geq \eta_{um}$. For a 1500 km thick compensation layer, the best variance reduction $V_{2\text{-}12}$ is only 33% (Table 4.2), suggesting that the compensation layer cannot be too thick. The viscosity profiles for the best-fit models (Table 4.2) are almost indistinguishable from those for the whole mantle convection. The tradeoffs for the inversion parameters are also analyzed, and for models with relatively large variance reduction, both the viscosity parameters and their ratios fall in very similar ranges to those for the whole mantle convection model (Figures 4.4a and 4.4b). The conversion factor for models with $V_{2\text{-}12}$>72% ranges from 0.38 and 0.44, and the best-fit model has c=0.42.

Without the restriction $\eta_{tz} \geq \eta_{um}$, the geoid constrains that the transition zone is weaker than the upper mantle (Figure 4.3b), and the geoid fit is significantly improved compared with models with that restriction in section 4.3.1.1 (Tables 4.1 and 4.2). In the following sections, the analyses are focused on these models with a weak transition zone.

4.3.2. Power spectrum and degree-correlation of the model geoid contributed from different depths

The Earth's geoid is prevalently at long wavelengths (Lerch *et al*., 1983, Figure 4.1b). The power (equation 4.6) of the geoid at degrees 2 and 3 accounts for 65%

and 21%, respectively, of the total power from degrees 2 to 12 (Figure 4.10d). The long wavelength components of the geoid have a deep source (Hager & Richards, 1989), and are highly correlated with the lower mantle structure such as LLSVPs (Figure 4.1a). The previous section shows that after removing the mantle buoyancy structure in the bottom ~1000 km thick compensation layer as expected for the thermochemical mantle model, those instantaneous models can still reproduce the geoid with a similar viscosity structure to that in whole mantle convection models. It is of interest where the long wavelength geoid (i.e., degrees 2 and 3) in those thermochemical models is originated from, and how the contributions from different depths vary between the two types of mantle models.

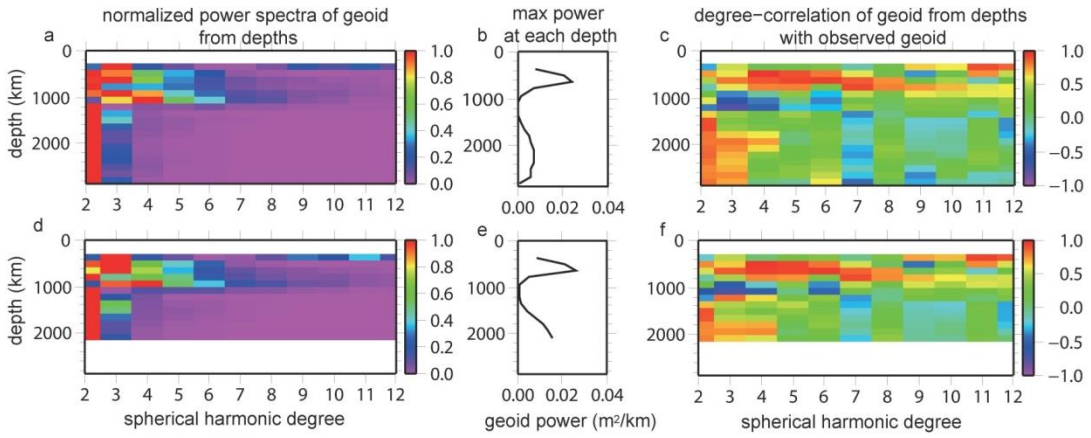

Figure 4.5. (a) the normalized power spectra of the geoid at degrees 2-12 contributed from different depths, (b) the maximum power among degrees 2-12 contributed from the layer with unit thickness at each depth, that is used to normalize the power spectra in (a) at the corresponding depth, and (c) the degree-correlation between the observed geoid and the geoid contributed from a given depth for the whole mantle convection model. (e)-(f) are the counterparts of (a)-(c), respectively, for the thermochemical convection model with a 720 km thick compensation layer. (a)-(f) are for the best-fit geoid models using the seismic model SAW642ANb.

For the best-fit model assuming the whole mantle convection, the geoid contributed from each depth is dominantly at degree-2 across the mantle except for depths of ~1000-1300 km (Figure 4.5a). Between the depths of 1000-1300 km the geoid power is relatively small (Figure 4.5b), and this is mainly because the geoid is insensitive to the buoyancy at these depths where the geoid kernels at long wavelengths (e.g., degree 2) are near 0 (Figure 4.6a). In the top 1000 km of the mantle, although the geoid power at degree 2 from each depth is large with a maximum at ~600 km depth (Figure 4.5b), the effective contribution from this region to the observed geoid is limited due to the poor degree-correlation at long wavelengths (Figure 4.5c). In total, the square root power of the degree 2 geoid contributed from this region is ~ 56 m, with a degree-correlation of 47% with the observed geoid. In contrast, at degree 2, the geoid contributed from below the 1300 km depth, with a total square root power of 96 m, is highly correlated (80%) with the observed geoid. It can be concluded that the degree 2 observed geoid is mainly originated from the lower mantle below the 1300 km depth. Analyses are also done on the degree 3 geoid. Although the geoid from the deep mantle (i.e., below the 1300 km depth) has a very large correlation at degree 3 (Figure 4.5c), the power is too small compared to that from the upper part of the mantle (Figures 4.5a and 4.5b). As a result, the lower and upper parts of the mantle have similar effective contributions to the observed geoid at degree 3. At degree 3, the geoid contributed from the lower mantle below the 1300 km depth has a square root power of 35 m, and a degree-correlation of 70%, while the geoid from the upper region (above the 1000 km depth) has a square root power of 45 m, and a degree-correlation of 79% with the observed geoid. At shorter wavelengths, the geoid is largely originated from the mantle above ~1000 km depth (Figure 4.5a).

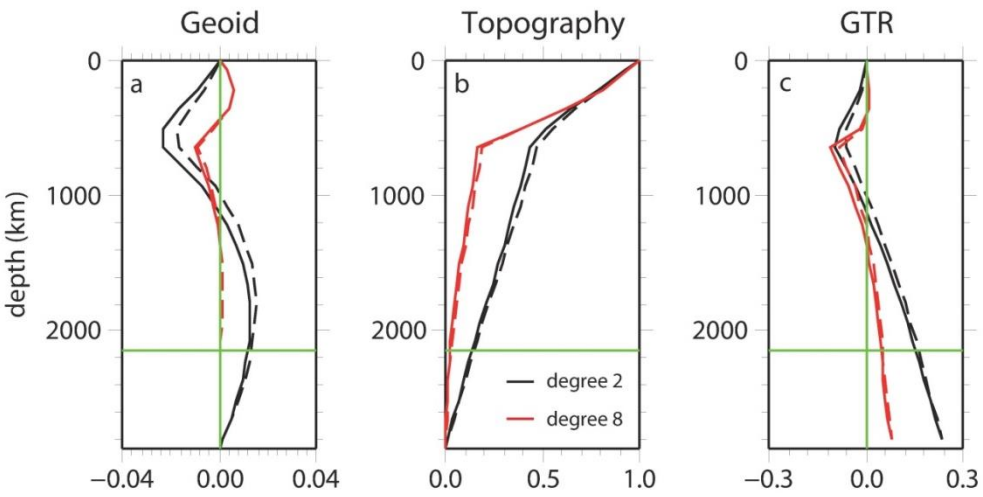

Figure 4.6. Kernels of (a) geoid, (b) surface dynamic topography, and (c) GTR for the best-fit models assuming both the whole mantle convection (solid lines) and the thermochemical convection with a 720 km thick compensation layer (dashed lines) at degrees 2 (black) and 8 (red). The vertical and horizontal green line marks the value of 0 and the compensation depth, respectively.

Analyses are performed for the best-fit model assuming the thermochemical convection with a compensation thickness of 720 km. The difference of the viscosity profiles between this model and the whole mantle model is minimal (Table 4.2). The power spectra and the degree-correlation of the geoid from difference depths (Figures 4.5d-4.5f) share similar patterns to that of the whole mantle model (Figures 4.5a-4.5c). The geoid power from ~1000 km to ~1300 km is nearly zero. At degree 2, the geoid power reaches maximum both at ~600 km depth in the upper mantle and at the depth above the compensation layer, but the degree-correlation is much higher in the lower mantle (Figure 4.5f). The square root power of the degree 2 geoid from below the ~1300 km depth is ~ 74 m, with a degree-correlation of 80% with the observed geoid, while the mantle above the 1000 km depth contributes a square root power of 49 m

with a degree-correlation of 50% with the degree 2 observed geoid. Therefore, the degree 2 geoid is mainly originated from the lower part of the mantle, similar to the whole mantle model as discussed earlier.

It is noticed that even after removing mantle structure in the bottom 720 km thick layer, the geoid power contributed from below 1300 km depth in the thermochemical model is still comparable to that in the whole mantle model (Figures 4.5b and 4.5e). Notice that Figure 4.5c also represents the degree-correlation between the seismic structure and the observed geoid. The seismic structure, hence the buoyancy structure, is continuous from the lowermost mantle to the mid-mantle, and is highly correlated with the observed geoid below the 1300 km depth. The slight difference in the viscosity profile between the whole mantle and thermochemical models causes a noticeable difference in the geoid kernels at degree 2 (Figure 4.6a). In the lower mantle below the 1300 km depth, the positive geoid kernel is larger in the thermochemical model than that in the whole mantle model. Since the buoyancy structure at mid-mantle depths is highly correlated with the observed geoid, the larger geoid kernel, together with an increase of the conversion factor *c*, make it possible for the thermochemical model to fit the degree-2 geoid using mantle buoyancy between the 1300 km depth and the compensation layer.

4.3.3. Surface dynamic topography and geoid-to-topography ratio (GTR)

Surface dynamic topographies are computed for the best-fit models assuming the whole mantle convection and the thermochemical convection with a 720 km thick compensation layer (Figures 4.7a and 4.7b) by convolving topography kernels (Figure 4.6b) with mantle buoyancy. Surface dynamic topography in the thermochemical model shows similar patterns to that in the whole mantle model, but with larger

amplitudes, particularly at relatively short wavelengths (Figures 4.7a and 4.7b). This can be understood from the topography kernels and the geoid-to-topography ratio (GTR).

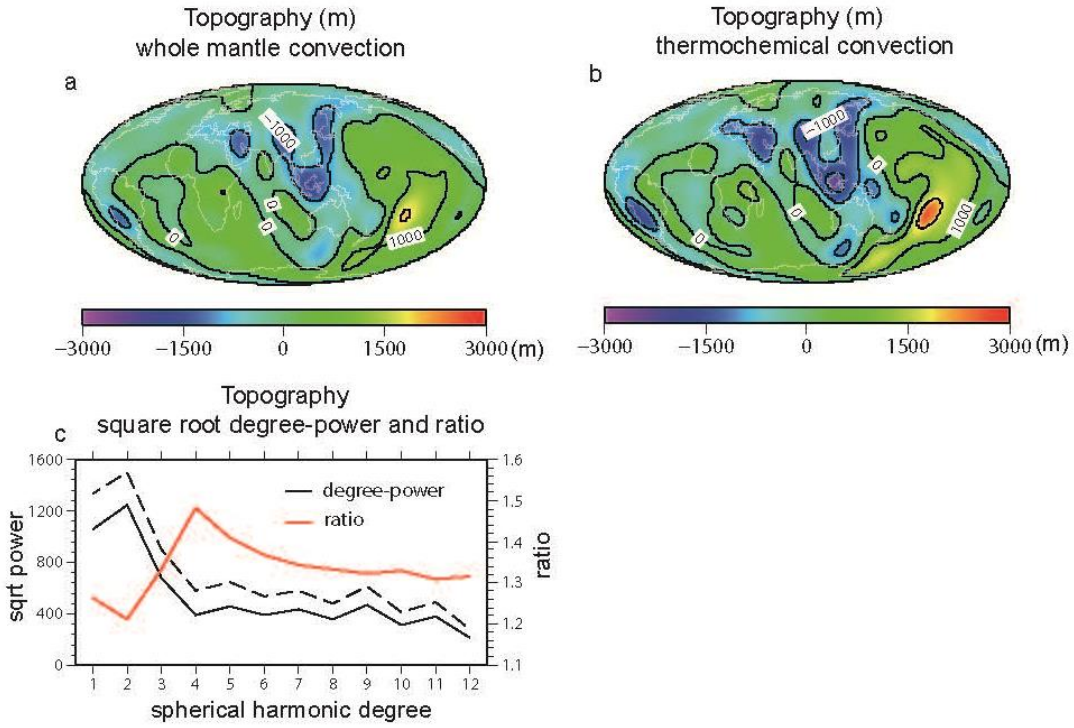

Figure 4.7. The surface dynamic topography for the best-fit models based on SAW642ANb assuming (a) the whole mantle convection, and (b) the thermochemical convection with a 720 km thick compensation layer. Contour lines of 1000 m are plotted in (a) and (b). (c) The square root degree-power of (a) (solid line) and (b) (dashed line), and the ratio of (b) over (a) (red line).

For both thermochemical and whole mantle models, topography kernels are positive across the mantle, and are nearly identical. Notice that when assuming the thermochemical convection, the buoyancy structure in the compensation layer is

removed, and would not contribute to the topography. However, the thermochemical model requires a larger conversion factor compared with that of the whole mantle convection to explain the geoid, implying that the mantle structure above the compensation layer would result in larger buoyancy and produce larger surface dynamic topography. At relatively short wavelengths (e.g., degree 8), the topography kernels for both models are negligibly small at depths of the compensation layer (Figure 4.6b). Consequently, in both models, the relatively short wavelength topography is mainly generated by the buoyancy structure in the upper part of the mantle above the compensation depth. Therefore, the thermochemical model with a larger conversion factor *c* would have a larger topography at these wavelengths compared with that of the whole mantle model. The ratio of the relatively short-wavelength topographies between the two models is approximately the ratio of their conversion factor *c* with the topography of the thermochemical model being ~30% larger (Figure 4.7c).

At long wavelengths (e.g., degree 2), the buoyancy in the compensation layer makes a non-eligible contribution to the surface topography in the whole mantle model (Figure 4.6b). For the thermochemical mantle model, the effect of a larger conversion factor on the topography is partially offset by the effect of removing the buoyancy in the compensation layer. However, the dynamic topography in the thermochemical model would still be larger than that in the whole mantle model, although the difference between these two models is smaller than that at relatively short-wavelengths (Figure 4.7c), and that is because in the lower mantle below ~1200 km depth, the geoid-to-topography ratio (GTR) at degree 2 for both models are positive and increase with depth. Removing the buoyancy in the compensation layer in the thermochemical model would result in a reduced averaged GTR compared with

that of the whole mantle model. A smaller GTR implies that, to produce the same observed geoid, the thermochemical model would produce more topography.

4.4. Discussion

4.4.1. The geoid, thermochemical mantle convection, and structure in the lower mantle

Our study shows that the long-wavelength geoid anomalies can be reproduced in thermochemical mantle models in which the LLSVPs are interpreted as stable, negatively buoyant chemical piles. Therefore, our study helps resolve the dilemma that while the geoid observation appears to support isochemical, whole-mantle model (e.g., Hager and Richards, 1989; Forte and Mitrovica, 2001), seismic and geochemical observations require that the mantle has large-scale, stable chemical heterogeneities including the LLSVPs (e.g., Jackson *et al*., 2014; Boyet and Carlson, 2005). In modeling the geoid from seismic models for a thermochemical mantle, our study considers the compensation effect of stable, negatively buoyant chemical piles on the geoid (Liu and Zhong, 2015) that helps circumvent difficulties in inferring the buoyancy for thermochemical heterogeneities such as the LLSVPs in seismic models.

In the whole mantle convection model, the deep mantle with the LLSVPs plays a critical role in explaining the long wavelength geoid. However, the thermochemical model in our study reproduces the observed geoid, although a significant part of the lower mantle above CMB (i.e., a compensation layer of ~1000 km thick) is removed due to the compensation effect. That the thermochemical model fits the geoid well without the structure in the bottom ~1000 km thick layer of the

mantle is rather surprising, given that the degree-2 buoyancy structure in this layer including the LLSVPs contributes significantly to the geoid in the whole mantle model (Figure 4.5b). The good geoid fitting arises because the degree-2 mantle seismic and hence buoyancy structure is continuous from CMB to the mid-mantle depth (~ 1300 km depth), and is highly correlated with the observed geoid. The buoyancy structure in the mid-mantle effectively contributes to the long wavelength geoid and makes it possible for thermochemical models to reproduce the observed geoid (Figures 4.5d-4.5f), without the buoyancy structure in the compensation layer, as shown in section 4.3.2.

Our results have a number of implications for mineral physics and seismology. First, notice that our thermochemical models considering the compensation effect suggest a larger conversion factor from seismic velocity to density anomalies in the isochemical part of the mantle above the compensation layer. This should have implications for mantle mineral physics. Second, our thermochemical models indicate an important role of mantle structure in the mid-mantle above the compensation layer in explaining the geoid. However, seismic tomographic models often do not have as good resolution at this depth range as that for the bottom of the mantle. Therefore, future seismic studies should seek to further improve the resolution at the mid-mantle depths. Third, our thermochemical models suggest that the vertical extent of chemically dense and stable piles (i.e., LLSVPs) above the CMB may not exceed 300-500 km. Seismic estimates of vertical extent of chemically distinct LLSVPs or superplumes range from several hundreds to over a thousand kilometers, based on the anti-correlation of shear wave and bulk sound speeds (Masters *et al*., 2000) or wave-form modeling (Ni *et al*., 2002; Wen *et al*., 2001; He and Wen, 2009). Ni *et al*. (2002) suggested that the African anomaly, where compositional anomalies are embedded in

thermal plumes, would rise to as high as ~1000 km from the CMB. However, it is unclear how thick the chemically dense and stable portion of LLSVPs is. Our results show that thermochemical models with a compensation layer thinner than 720 km reproduce the observed geoid well, while the geoid fitting decreases rapidly with thicker compensation layer, especially with layers thicker than 1000 km (e.g., the variance reduction decreases from 77% to 65% as the compensation layer thickness increases from 720 km to 1000km, respectively, and it drops to 33% as the layer thickness increases to 1500 km) (Table 4.2), indicating an upper bound of compensation layer thickness of ~1000 km. Considering that, from studies of mantle convection models (Liu and Zhong, 2015), the compensation layer thickness is about twice of the vertical extent of chemically dense piles with uniform density, our results suggest an upper bound of the vertical extent of chemically dense piles of ~ 300-500 km above the CMB. This is consistent with seismic studies of anti-correlation between shear velocities and bulk sound velocities in LLSVPs (Master *et al*., 2002). However, this does not necessarily contradict with the existence of chemically distinct superplume structure rising to shallower depths as suggested in Ni *et al*., (2002), if such a structure is not negatively buoyant. For example, Tan and Gurnis (2005) proposed a compressible thermochemical convection model where metastable superplumes are dynamically maintained while negatively buoyant materials only exist in the upper part of thermochemical piles. We think that the geoid modeling such as that done in Liu and Zhong (2015) could provide an important test for these models.

4.4.2. A weak transition zone

An important outcome of the geoid modeling is to place constraints on mantle viscosity structure (e.g., Hager and Richards, 1989). Our study with the whole mantle

and thermochemical mantle models reveals two important features about mantle viscosity. First, mantle viscosity inferred from the geoid in the thermochemical mantle model is nearly identical to that in the whole mantle model, suggesting that the viscosity inferred from previous whole mantle models (e.g., Hager and Richards, 1989) remains largely valid. Second, with three seismic models considered here (i.e., SAW642ANb, S40RTS and Smean), our study suggests that the transition zone appears to be the weakest, being ~10 times weaker than the upper mantle and ~100 times weaker than the lower mantle (Table 4.2), irrespective of the whole-mantle or the thermochemical mantle models.

Our result that the transition zone is significantly weaker than the upper mantle is different from Hager & Richards (1989) where a stronger transition zone is preferred. We suspect that the difference may be caused by the difference in the mantle buoyancy used in our studies. King (1995) found two groups of viscosity profiles, with either a strong or a weak transition zone that would reproduce the observed geoid. He suggested that a large viscosity contrast between the upper mantle and transition zone would be critical in the geoid modelling. Our study using most recent seismic models seems to remove the ambiguity in preferring a weaker transition zone. That the transition zone is significantly weaker than the upper mantle has implications for mineral physics. Compared with the upper mantle, the transition zone minerals have much higher water solubility (e.g., Williams & Hemley, 2001; Nestola and Smyth, 2015), and the transition zone is estimated to have a water content of 0.2-2 wt% (Bercovici and Karato, 2003). The high water content would weaken the transition zone, and provide a supporting observation for the inferred viscosity profile from our study.

It should be pointed out that if the transition zone is restricted not to be weaker than the upper mantle, i.e., $\eta_{tz} \geq \eta_{um}$, our modeling indicates that η_{tz} would be about the same as η_{um} which is ~50 times smaller than the lower mantle (Table 4.1) for both whole-mantle and thermochemical models. This result is consistent with those inferred for the whole-mantle model in previous studies (e.g., Hager, 1984; Hager *et al*., 1985; Ricard *et al*., 1993). Previous studies also found that an extremely weak and thin layer around ~670 km depth would help fit the geoid (e.g., Panasyuk & Hager, 1998; Forte *et al*., 1993). We do not attempt to divide the mantle into more viscosity layers to further resolve finer viscosity structure, due to our concern on computational costs and potential tradeoffs among a large number of viscosity layers, as seen in viscosity inversions using post-glacial rebound observations (Paulson *et al*, 2007; Paulson and Richards, 2009).

4.4.3. Viscosity structure in the lower mantle

While our models assume a constant lower mantle viscosity, previous studies on modeling gravitational anomalies or the post-glacial rebound have employed viscosity models with significant viscosity increases within the lower mantle (e.g., Steinberger and Calderwood, 2006; Forte & Mitrovica, 2001). Recently, using a Bayesian inversion procedure, Rudolph *et al*. (2015) suggested a viscosity increase at ~ 1000 km depth using geoid modelling for whole mantle convection models.

Following same procedure as described in sections 4.2 and 4.3 and assuming the whole mantle convection, we tested the robustness of the viscosity stratification at 1000 km depth. We employ a 4-layer 1D viscosity profile with contrasts at 100 km, 670 km, and 1000 km depths (the four viscosities are denoted as η_{lith}, η_{um}, η_{up-lm}, η_{bot-lm}, from the surface to the CMB, respectively), with a fixed η_{lith} of 20 as before,

and a presumption that $\eta_{bot-lm} \geq \eta_{up-lm} \geq \eta_{um}$ (i.e., the viscosity monotonically increases with depth). Notice that we now combine the upper mantle and transition zone into one layer as the upper mantle for simplicity and reducing tradeoffs. After several zoom-in procedures, large amounts of models are calculated with η_{um}, η_{up-lm}, and η_{bot-lm} ranging from 0.02 to 7, 1 to 120, and 7 to 400, respectively. The best-fit model ($V_{2\text{-}12}$=77.90%) has a viscosity profile of η_{um} =0.4, η_{bot-lm} =30, and η_{up-lm} =30, respectively. Notice that no viscosity increase exists for this model at 1000 km depth. The model with the second large variance reduction ($V_{2\text{-}12}$=77.86%), however, has a viscosity jump at 1000 km from η_{up-lm}=8 to η_{bot-lm}=35, while its η_{um} is 0.6 which is close to that of the best-fit model. It is found that all the models that well reproduce the observed geoid ($V_{2\text{-}12}$>73%) have viscosity increase at 1000 km depth by a factor of 1 (i.e., no increase) to 10 (Figure 4.8). This significant tradeoff implies that a viscosity increase at 1000 km depth is not required from our geoid modelling study. The viscosity ratio of the upper mantle to the bottom lower mantle (i.e., below 1000 km depth), η_{um}/η_{bot-lm}, however, falls in a very narrow range of 1/30 to 1/100 (Figure 4.8), indicating that this viscosity contrast is a rather robust inference from our geoid modelling. This result is also consistent with our results in section 4.3.1.1 and classic studies where the viscosity in the lower mantle is about 30-60 times that of the upper mantle (e.g., Hager & Richards, 1989). The viscosity inversion with the same viscosity parameterization is also done for thermochemical models with a 720 km thick compensation layer. With viscosity structures similar with those inverted from whole mantle geoid models, thermochemical models can reproduce the observed geoid, although with smaller variance reductions. Thus, the compensation effect from thermochemical models does not affect the inferred viscosity stratification at 1000 km.

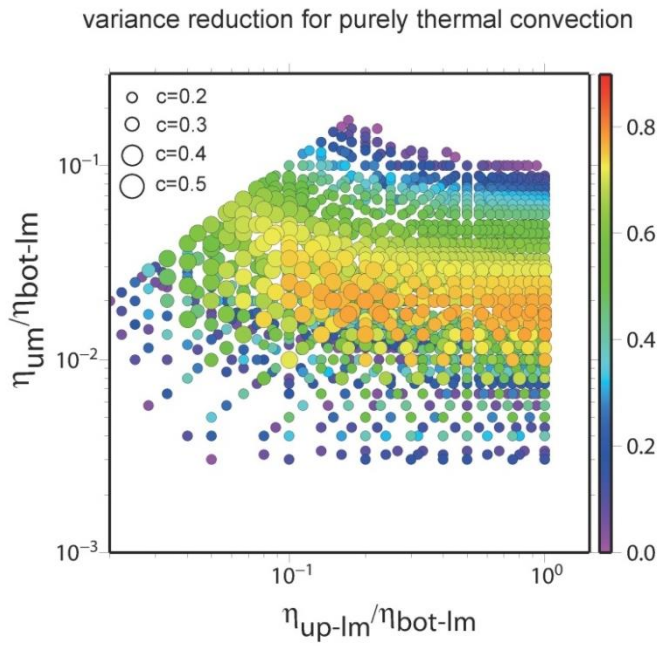

Figure 4.8. The variance reduction of the geoid in the logarithmic scale for whole mantle models with a presumed viscosity stratification at 1000 km depth, based on the seismic model SAW642ANb. Horizontal and vertical axes are the viscosity ratios of the upper part of the lower mantle (from 670 to 1000 km depths) to the bottom part of the lower mantle (below 1000 km depth), and of the upper mantle (from 100 to 670 km depths) to the bottom part of the lower mantle, respectively. The color and size of the circles illustrate the variance reduction and the conversion factor, respectively. For each radial viscosity profile, only the model with a conversion factor that best reproduces the observed geoid is plotted.

Therefore, our geoid modeling suggests that a more robust feature in the inferred mantle viscosity is a general increase of a factor of 30-100 from the upper mantle to the lower mantle, while it is not well constrained how and where the viscosity increases with the depth. A viscosity increase at ~1000 km depth as suggested by Rudolph *et al*. (2015) is possible but not required. Constraints other than

the geoid observation are needed to better understand the fine-layered viscosity structure in the lower mantle. One of the main justifications for the viscosity contrast at ~1000 km depth proposed by Rudolph *et al*. (2015) is the seismic imaging of plumes and slabs that appear to change their morphologies at that depth (Fukao *et al*., 2009; French & Romanowicz, 2014). However, more slab stagnations have been observed at the 670 km depth (e.g., Fukao *et al*., 2009). If the same reasoning is followed, the slab stagnations at ~670 km depth would also suggest a viscosity increase there. Moreover, slab geometries involve complex mechanism. For example, slab stagnations may be heavily influenced by trench roll back (e.g., Zhong & Gurnis, 1995; Christensen, 1996) and subduction history (e.g., Billen, 2008). More seismic and geodynamic studies are in need to further explore the slab structure and dynamics.

4.4.4. Dynamic topography

Dynamic topography for the Earth may be estimated by removing the isostatic compensation effect on the topography and determining the residual topography (e.g., Davies and Pribac, 1993; Lithogow-Bertelloni & Silver, 1998; Panasyuk and Hager, 2000). The residual topography can be estimated more robustly in oceanic regions than in continental regions because of the expected small variations in oceanic crustal structure. In oceanic regions, the residual topography shows topographic highs in central Pacific (i.e., the Pacific super-swell) ranging from ~1-2 km depending on different lithospheric thermal models (Panasyuk and Hager, 2000). Even after removing the effects of seamounts and oceanic islands, sediments, and the lithospheric thermal structure (i.e., the plate model), the central Pacific region still has ~1 km of residual topography (Zhong *et al*., 2007). Over large length-scale (> 6000 km or up to spherical harmonic degree 6), the estimated residual topography is generally in a range of ~ ±1 km (e.g., Panasyuk and Hager, 2000).

In our best-fit geoid model assuming the whole mantle convection, the dynamic topography at degrees 2 and 3 (i.e., long-wavelength) are in the range of ~±800 m and ~±400 m, respectively, with a topographic high of ~1 km in the central Pacific. The dynamic topography from our geoid models is consistent with the estimated residual topography (Panasyuk and Hager, 2000) and the dynamic topography computed from other geoid modelling studies (e.g., Hager & Richards, 1989; Lithogow-Bertelloni & Silver, 1998). It is of interest why the magnitude of the long wavelength dynamic topography is as high as ~1 km. While a recent study based on gravity-topography admittance argument suggested that dynamic topography may not exceed ~300 m at relatively small length-scales (Molnar *et al*., 2015), the admittance, or the geoid to topography ratio (GTR), may provide some insight for the high magnitude of the long wavelength topography in our model. Notice that the degree 2 GTR changes sign at ~1200 km depth, being negative above and positive below the depth (Figure 4.6c). The negative GTR reflects the negative geoid kernel in the upper mantle (Figure 6a), as the topography kernel is positive for the whole mantle (Figure 4.6b). The degree-2 seismic structure is a continuous feature from the upper to lower mantles (i.e., seismically slow below Africa and the central Pacific, Figures 4.9a and 4.9b). This suggests that dynamic topography produced by mantle structure at different depths generally adds to each other and highly correlates with the total surface topography (Figures 4.9e, 4.9f and 4.9h). However, the degree-2 geoid from the upper mantle is largely canceled out by that from the lower mantle due to the opposite signs of the kernel in the two regions (Figures 4.9c and 4.9d). The overall GTR should be the average of the GTR kernel over the whole mantle, weighted by depth distribution of the power (e.g., Figure 4.5b). In our best-fit whole mantle geoid model, the degree 2 GTR kernel ranges from -0.15 at ~600 km depth to

~0.25 above the CMB, and an averaged GTR of less than 0.1 is expected. This explains why to produce the observed degree-2 geoid of ~70 m in the Pacific, the models often produce ~ 800 m degree 2 topographic high there. The argument also applies for thermochemical mantle models, with an even smaller overall GTR.

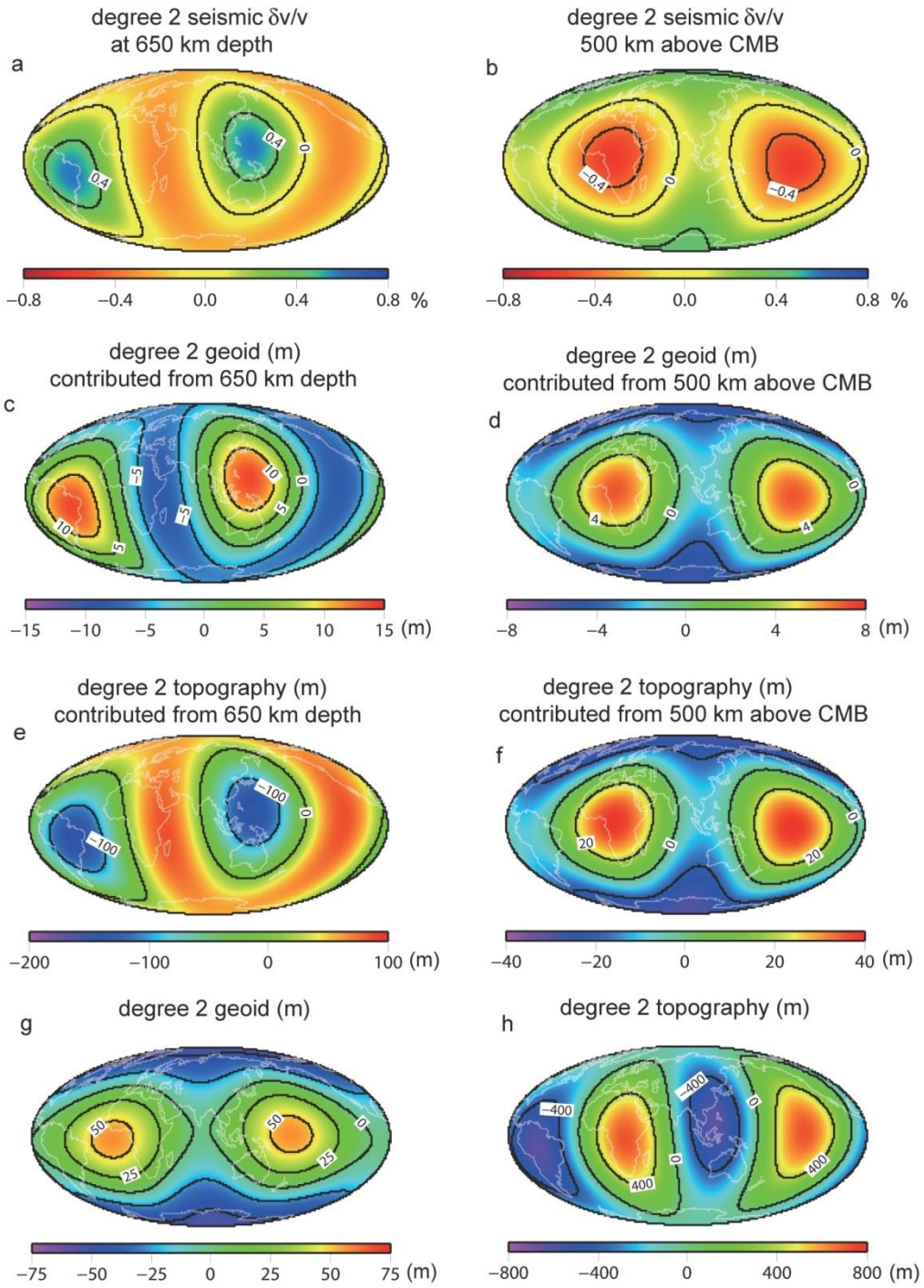

Figure 4.9. Seismic shear wave speed anomaly δv/v (model SAW642ANb) at (a) 650 km depth and (b) 500 km above CMB. Degree 2 geoid contributed from (c) 650 km depth and (d) 500 km above CMB, degree 2 surface dynamic topography contributed from (e) 650 km depth and (f) 500 km above CMB, and total degree 2 (g) geoid and (h) surface dynamic topography, of the best-fit geoid model assuming the whole mantle convection based on model SAW642ANb.

While our whole mantle models for the geoid yield similar dynamic topography to that from previous studies, our thermochemical models with the compensation effect lead to larger amplitude of dynamic topography due to a larger conversion factor, compared with those for the whole mantle model. The difference, however, is not significant (<30% overall), and we suspect that it would be challenging to use the inferred residual topography to distinguish the whole mantle and the thermochemical mantle models. It should be noticed that, in thermochemical models, since the buoyancy structure in the lowermost mantle is removed, the model CMB topography cannot be used to make meaningful geophysical inference for which fully dynamic models are needed.

4.4.5. The free-air gravity anomaly

While the long wavelength structure in the Earth's gravitational field is well represented in the geoid (Figure 4.1b), the small-scale features are more evident in the free-air gravity anomalies (Figure 4.10a, EGM2008 model) (Pavlis *et al.*, 2012). Notice that we have subtracted the free-air gravity anomaly caused by the glacial isostatic adjustment process (A *et al.*, 2013) from the original EGM2008 model. The degree power for the geoid decreases rapidly as the wavelength decreases, while the free-air gravity anomalies have relatively flat power spectra (Figure 4.10d). This is because free-air gravity anomalies, gFA_{lm}, can be simply related to the geoid h_{lm} by $gFA_{lm} = (l-1)h_{lm}g/R$ where l is the spherical harmonic degree, g is the reference gravitational acceleration, and R is the Earth's radius.

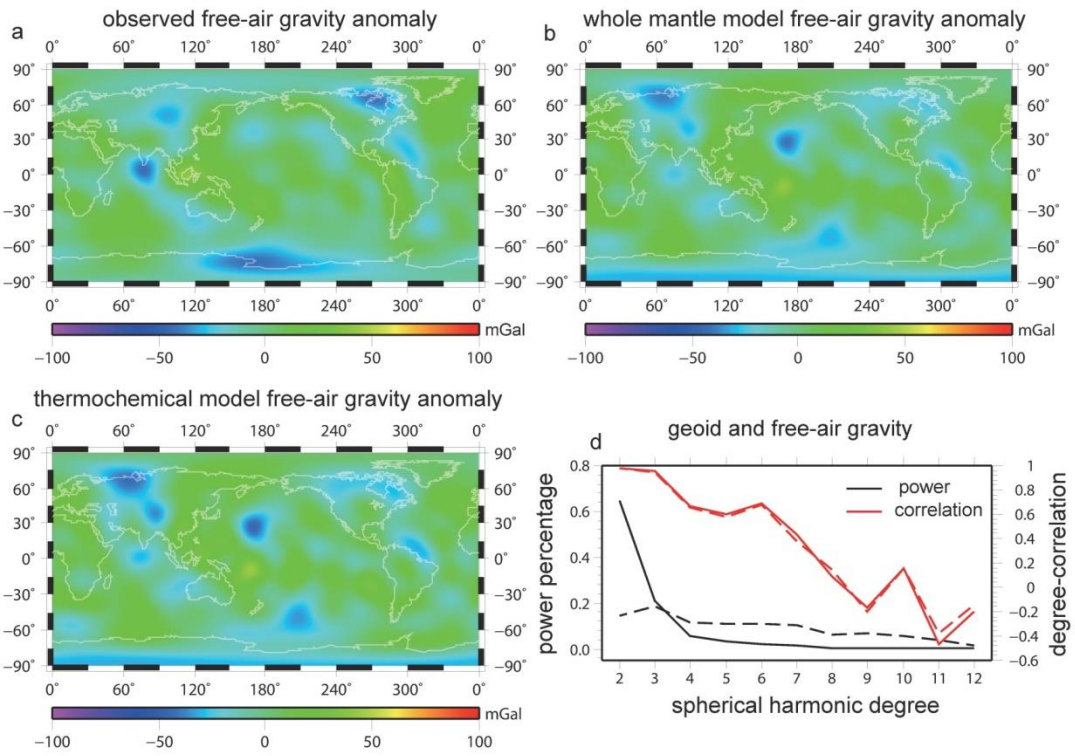

Figure 4.10. (a) Observed free-air gravity anomaly (model EGM2008), and computed free-air gravity anomalies for best-fit models assuming (b) the whole mantle convection, and (c) the thermochemical convection with a 720 km thick compensation layer. (d) Degree power percentages over degrees 2 to 12 (black) for the observed geoid (solid line) and free-air gravity (dashed line), and the degree-correlations (red) of the computed geoid (solid line) and free-air gravity (dashed line) with the observations for the best-fit thermochemical models with a 720 km thick compensation layer.

We have computed *gFA* up to degrees and orders 12 for best-fit geoid models assuming both the whole mantle convection (Figure 4.10b) and the thermochemical convection with the compensation thickness of 720 km (Figure 4.10c), using the similar kernel approach. Both whole mantle and thermochemical models reproduce the long wavelength pattern of the *gFA* (Figures 4.10b and 4.10c). However, the

model *gFA* has significantly lower total degree-correlations with the observation with $C_{2\text{-}12}$ at 58% for the whole mantle model, and 52% for the thermochemical model, compared with the model geoid (e.g., Table 4.2). This is consistent with the findings from previous studies (e.g., Forte *et al*., 2010). A close examination reveals that the degree-correlation is very high at degrees 2 and 3, and it decreases with harmonic degree. At relatively short wavelengths, the correlation is poor, and is smaller than 50% for degrees larger than 6 for both models (Figure 4.10d). It is also found that at each degree the correlation for *gFA* between the model and the observation is nearly identical to that for the geoid (Figure 4.10d). Since the geoid is dominantly at degrees 2 and 3, its total correlation as well as the variance reduction can be high even with poor degree-correlations at short wavelengths (Figure 4.10d).

The difference in spectral content for the geoid and free-air gravity anomalies may have implications for inference of mantle viscosity structure using these observations. For example, the inferred mantle viscosity from the geoid weighs more on long-wavelength mantle structure at the large depths, while free-air gravity based inference may incorporate more small-scale structure at relatively shallow depths. The small-scale structure at shallow depths may be more difficult to resolve seismically and interpret geodynamically due to uncertainties associated with anisotropy and compositional heterogeneities. Consequently, it is important to investigate optimal inversion procedures for mantle viscosity using these observations.

4.4.6. Potential drawback and future work

In this study, the compensation effect of negatively buoyant chemical piles observed in dynamically self-consistent thermochemical convection models (Liu & Zhong, 2015) is utilized in the geoid modeling. This approach avoids the difficulty of

determining the buoyancy structure of the chemical piles from the seismic structure. However, there are several potential drawbacks in this approach. While the dynamically self-consistent thermochemical models suggest that the compensation layer thickness is ~2-3 times of the chemical piles (Liu & Zhong, 2015), a precise knowledge on the compensation thickness for the Earth is unclear. Since the bottom part of the mantle is removed to account for the compensation effect, the CMB topography in our thermochemical models does not reveal the lower mantle dynamics that would be heavily influenced by the thermochemical piles. Our geoid modelling employs an 1-D viscosity, while the low viscosity of the chemical piles due to temperature and compositional effects might be important in the lower mantle dynamics. Nevertheless, the 1-D viscosity inverted from this study has laid a foundation for future studies to formulate instantaneous models based on seismic mantle structure with realistic temperature- and composition-dependent viscosity, and explore the buoyancy structure in the thermochemical piles and the ambient mantle by fitting the geoid and surface and CMB topographies.

4.5. Conclusion

In this study, we formulate instantaneous mantle flow models for the geoid and dynamic topography assuming both thermochemical and whole mantle convection with mantle buoyancy structure derived from seismic tomographic models SAWANb642, S40RTS, and Smean. Our models employ an 1-D viscosity structure and the geoid is calculated using the propagator matrix method. The thermochemical mantle model considers the compensation effect of the stable, negatively buoyant thermochemical piles (i.e., LLSVPs).

Our thermochemical mantle models treating the LLSVPs as negatively buoyant thermochemical piles can well reproduce the Earth's geoid, thus reconciling the geoid observation with the interpretation of the LLSVPs as long-term stable chemical reservoirs. The inferred mantle viscosity structure in the thermochemical model is nearly identical to that for the whole mantle model. Both models prefer a weak transition zone, and in the preferred viscosity model, the lower mantle viscosity is ~10 times higher than the upper mantle viscosity that is ~10 times higher than the transition zone viscosity. A larger conversion factor from seismic velocity to density anomalies is required to fit the geoid in the thermochemical mantle model compared with that of the whole mantle model, resulting in a larger (~30%) surface dynamic topography in the thermochemical model. The amplitude of long-wavelength (degrees 2 and 3) dynamic topography is about ±1.2 km, which is generally consistent with previous whole mantle models. Our geoid modeling studies suggest that the compensation layer is likely to be thinner than ~1000 km, and that the upper bound of the vertical extent of the chemically distinct and negatively buoyant piles or LLSVPs above the CMB is ~300-500 km. Our studies indicate that mantle structure at mid-mantle depths (e.g., between 1300 km and 2100 km depths) controls the geoid for a thermochemical mantle model. This suggests that future seismic models need to further improve resolution at the mid-mantle depths. While it is possible that the lower mantle viscosity may increase significantly with depth (e.g., at ~1000 km depth), the geoid modeling only provides a limited depth resolution, and a more robust conclusion is a general increase in viscosity by a factor of ~100 from the upper mantle to depths below 1000 km.

Chapter 5

Summary

5.1. Summary of the compressible mantle convection study

In Chapter 2, a 2D Cartesian compressible convection model is formulated to examine the effects of compressibility on thermal convection. A new implementation of propagator matrix technique for marginal linear stability analysis is presented and the critical Rayleigh number for different dissipation numbers *Di* and wave-numbers k_x is determined. In the regime of finite amplitude convection, I use a finite element code to study the influence of *Di* on thermal boundary layer (TBL) properties and heat flux for models with $k_x=\pi$ and different *Di* and *Ra*. Scaling laws that describe the dependence of TBL properties and heat flux on *Di* and *Ra* are determined. The conclusions are as follows:

(1) Critical Rayleigh numbers, Ra_c, at the fundamental and higher modes are determined for thermal convection in a compressible fluid. At the fundamental mode, if *Ra* is defined by the surface density, Ra_c may not show a monotonic variation with dissipation *Di*. The fundamental mode may only exist for relatively small *Di*.

(2) For thermal convection with depth-dependent density or thermodynamics parameters, the eigenfunctions are no longer sinusoidal functions, as they are for thermal convection in a homogeneous, incompressible fluid. For $Di > 0$, the

eigenfunctions for temperature $T_0(z)$, horizontal velocity $U(z)$, and vertical velocity $V(z)$ have larger amplitudes at the shallower depth than those at the larger depths, and shear driven convective cell may appear for large *Di*.

(3) Ra_c are also determined from numerical experiments for different *Di* and wavelengths. With the eigenfunctions for temperature $T_0(z)$ as initial perturbations, numerically determined Ra_c agree well with Ra_c computed from marginal stability analysis.

(4) Thermal boundary layer (TBL) properties are quantified in numerical models of thermal convection in a compressible fluid at different *Ra* and *Di*. TBL thicknesses and temperature differences are heavily influenced by *Di*. While temperature differences across the TBLs decrease with *Di*, TBL thicknesses increase with *Di*. The ratios of top TBL thickness and temperature difference to corresponding bottom TBL properties are $e^{Di/2}$. For both incompressible and compressible convection, TBL thicknesses follow $\delta_l \sim Ra^{-1/3}$, while TBL temperature differences are insensitive to *Ra*.

(5) Our numerical modeling shows that the local Rayleigh numbers at the top and bottom TBLs are nearly identical and are insensitive to *Ra* and *Di* for compressible convection.

(6) The scaling laws of the temperature differences across TBLs, ΔT_t and ΔT_b, are derived as $\Delta T_t = [1 - T_s(e^{Di} - 1)]/(e^{-Di/2} + e^{Di})$ and $\Delta T_b = [1 - T_s(e^{Di} - 1)]/(1 + e^{3Di/2})$. ΔT_t and ΔT_b are found only dependent on *Di*. The scaling laws are verified by numerical results.

(7) The scaling law of heat transfer, Nusselt number *Nu*, for thermal convection in an isoviscous, compressible fluid is derived to be $Nu = (\frac{1 - T_s(e^{Di} - 1)}{e^{-Di/2} + e^{Di}})^{4/3} (\frac{Ra}{Ra_t})^{1/3}$. *Nu* scales with *Ra* as $Nu \sim Ra^{1/3}$, similar with that for incompressible convection. The scaling law for *Nu* is consistent with numerical modeling results. We think that these results may have important implications for understanding thermal evolution of super-Earths.

5.2. Summary of the study on the long wavelength geoid in thermochemical mantle convection models

The second part of this thesis (Chapters 3 and 4) studies the effects of two chemically distinct and stable piles in the lowermost mantle (e.g., the LLSVPs) on the Earth's long wavelength geoid. It is shown that the long-wavelength geoid anomalies can be reproduced in dynamically self-consistent thermochemical mantle models in which the LLSVPs are interpreted as stable, negatively buoyant chemical piles. We found that the buoyancy from a large portion of the lower mantle (~1000 km in thickness) including the chemically dense piles has zero net contribution to the geoid due to compensation effects. Considering the compensation effect, we investigated how well the geoid can be explained in instantaneous flow assuming the thermochemical convection based on seismic tomographic models. We also reexamined the geoid constraints on the viscosity and buoyancy structure for a thermochemical mantle. Comparison was done for the inverted viscosity and buoyancy structure between our best-fit models assuming the thermochemical

convection and those from classic studies assuming the purely thermal, whole-mantle convection.

In Chapter 3, I presented a series of 3-D spherical convection models assuming both the purely thermal and the thermochemical convection. These dynamically self-consistent models include temperature- and depth-dependent viscosity. A degree-2 dominant convective structure that is similar to the present-day Earth's mantle can be dynamically maintained with realist lithosphere and mantle viscosity. I computed the geoid anomalies and analyzed how the geoid is contributed from the buoyancy structure at different depths. It is found that positive geoid anomalies can be produced over chemically dense piles, suggesting that the positive long-wavelength geoid anomalies observed in the Pacific and Africa are consistent with the interpretation of the two LLSVPs as chemically dense, possibly primitive thermochemical piles. Moreover, our dynamic models show that the chemically dense piles have a compensation effect on the surface geoid, and the compensation layer at the bottom of the mantle that is 2 to 3 times as thick as the chemical piles (or ~1000 km thick) has zero net contribution to the surface long wavelength geoid.

I also examined how the CMB topography is influenced by the above chemical piles. It is also found that the CMB topography is smooth and slightly negative in the regions with thermochemical piles, but significant and rapid variations in CMB topography occur outside the chemical pile regions where both the largest depression and uplifts at the CMB are found. The largest CMB depression is always under major downwellings, but the largest uplift at the CMB is near the chemical piles.

Finally, it is found that thermochemical piles in the dynamic models have a passive and secondary effect on large-scale convective structure that is controlled by mantle viscosity structure and convection above the thermochemical piles.

In Chapter 4, I formulated instantaneous mantle flow models and solved for the geoid and dynamic topographies assuming both thermochemical and whole mantle convection with mantle buoyancy structure derived from seismic tomographic models SAWANb642, S40RTS, and Smean. The models employ an 1-D viscosity structure and the geoid is calculated using the propagator matrix method. The thermochemical mantle model considers the compensation effect of the stable and negatively buoyant thermochemical piles (i.e., LLSVPs). Our thermochemical mantle models can well reproduce the Earth's geoid, thus can reconcile the geoid observation with the interpretation of LLSVPs as long-term stable chemical reservoirs. The inferred mantle viscosity structure in the thermochemical model is nearly identical to that for the whole mantle model. Both models prefer a weak transition zone, and in the preferred viscosity model, the lower mantle viscosity is ~10 times higher than the upper mantle viscosity that is ~10 times higher than the transition zone viscosity. A larger conversion factor from seismic velocity to density anomalies is required to fit the geoid in the thermochemical mantle model compared with that of the whole mantle model, resulting in a larger (~30%) surface dynamic topography in the thermochemical model. The amplitude of long-wavelength (degrees 2 and 3) dynamic topography is about ±1.2 km, which is generally consistent with previous whole mantle models. Our geoid modeling studies suggest that the compensation layer is likely to be thinner than ~1000 km, and that the upper bound of the vertical extent of the chemically distinct and negatively buoyant piles or LLSVPs above the CMB is ~300-500 km. Our studies indicate that mantle structure at mid-mantle depths (e.g.,

between 1300 km and 2100 km depths) controls the geoid for a thermochemical mantle model. This suggests that future seismic models need to further improve resolution at the mid-mantle depths. While it is possible that the lower mantle viscosity may increase significantly with depth (e.g., at ~1000 km depth), the geoid modeling only provides a limited depth resolution, and a more robust conclusion is a general increase in viscosity by a factor of ~100 from the upper mantle to depths below 1000 km.

Bibliography

Balachandar, S., D. A. Yuen, & D. Reuteler (1992), Time-dependent three-dimensional compressible convection with depth-dependent properties, *Geophys. Res. Lett.*, **19**(22), 2247–2250.

Becker, T.W., L. Boschi (2002), A comparison of tomographic and geodynamic mantle models, *Geochem. Geophys. Geosysts*., doi: 10.1029/2001GC000168.

Bercovici, D., and S. Karato (2003), Whole-mantle convection and the transition-zone water filter, *Nature* 425, 39-44, doi:10.1038/nature01918.

Bercovici, D., G. Schubert and G. Glatzmaier (1992), Three-dimensional convection of an infinite-Prandtl-number compressible fluid in a basally heated spherical-shell, *J. Fluid Mech.*, **239**, 683–719.

Billen, M. I. (2008), Modeling the Dynamics of Subducting Slabs, *Annu. Rev. Earth Planet. Sci*., 36, 325-356, doi:10.1146/annurev.earth36.031207.124129.

Birch, F., (1952), Elasticity and constitution of the earth interior. *J. Geophys. Res.*, **57**(2), 227–286, doi:10.1029/JZ057i002p00227.

Bower, D.J., M. Gurnis, and M. Seton (2013), Lower mantle structure from paleogeographically constrained dynamic Earth models, *Geochem. Geophys. Geosysts.*, 14, 44–63. doi:10.1029/2012GC004267

Boyet, M., and R. W. Carlson (2005), Nd-142 evidence for early (> 4.53 Ga) global differentiation of the silicate Earth, *Science*, 309, 576–581.

Buffet, B.A., C. W. Gable, and O'Connell, R.J., 1994. Linear stability of a layered fluid with mobile surface plates, *J. Geophys. Res.*, **99**(B10), 19885–19900.

Bunge, H.P., M. A. Richards, and J. R. Baumgardner (1996), Effect of depth-dependent viscosity on the planform of mantle convection, *Nature* 379, 436–438.

Charbonneau, D., Z. K. Berta, J. Irwin, C. J. Burke, P. Nutzman, L. A. Buchhave, and C. Lovis *et al*., (2009), A super-Earth transiting a nearby low-mass star, *Nature*, **462**(7275), 891–894.

Christensen, U. R. (1996), The influence of trench migration on slab penetration into the lower mantle, *Earth Planet. Sci. Lett*. 140, 27–39.

Coltice, N., T. Rolf, P. J. Tackley, and S. Labrosse (2012), Dynamic causes of the relation between area and age of the ocean floor, *Science*, 336, 335-338.

Davaille, A. (1999), Simultaneous generation of hotspots and superswells by convection in a heterogenous planetary mantle, *Nature* 402, 756–760.

Davies, G. F. (1999), Dynamic Earth: Plates, Plumes and Mantle Convection, 458 pp., *Cambridge Univ. Press*, New York.

Davies, G.F. and F. Pribac (1993), Mesozoic Seafloor Subsidence and the Darwin Rise, Past and Present, in: The Mesozoic Pacific: Geology, Tectonics, and Volcanism. *Am. Geophys. Un.*, pp. 39–52.

Davies, D. R., J. H. Davies, O. Hassan, K. Morgan, and P. Nithiarasu (2007), Investigations into the applicability of adaptive finite element methods to two-dimensional infinite Prandtl number thermal and thermochemical convection, *Geochem. Geophys. Geosysts*. 8, Q05010. doi:10.1029/2006GC001470

Davies, D.R., S. Goes, J. H. Davies, B. S. A. Schuberth, H.-P. Bunge, J. Ritsema, (2012), Reconciling dynamic and seismic models of Earth's lower mantle: The dominant role of thermal heterogeneity, *Earth Planet. Sci. Lett*., 353, 253–269. doi:10.1016/j.epsl.2012.08.016.

Dziewonski, A. M., and D. L. Anderson (1981), Preliminary Reference Earth Model (PREM), *Phys. Earth Planet. Inter*., 25, 297-356.

Dziewonski, A. (1984), Mapping the lower mantle: Determination of lateral heterogeneity in P-velocity up to degree and order 6. *J. Geophys. Res.*, 89, 5929–5952.

Foley, B.J., D. Bercovici, and W. Landuyt (2012), The conditions for plate tectonics on super-Earths: Inferences from convection models with damage, *Earth Planet. Sci. Lett.*, **331-332** (2012), 281-290.

Forte, A. M., A. Dziewonski, and R. L. Woodward (1993), Aspherical structure of the mantle, tectonic plate motions, nonhydrostatic geoid, and topography of the core-mantle boundary, *Am. geophys. Un., geophys. Mon*., 72, 135–166.

Forte, A.M., J. X. Mitrovica (2001), Deep-mantle high-viscosity flow and thermochemical structure inferred from seismic and geodynamic data, *Nature*, 410, 1049–1056.

Forte, A. M., S. Quéré, R. Moucha, N. A. Simmons, S. P. Grand, J. X. Mitrovica, and D. B. Rowley (2008), Joint seismic–geodynamic-mineral physical modelling of African geodynamics: A reconciliation of deep-mantle convection with surface geophysical constraints, *Earth Planet. Sci. Lett.*, 295, 3-4, 329-341, doi:10.1016/j.epsl.2010.03.017.

French, S. and B. Romanowicz (2014), Whole mantle radially anisotropic shear--velocity structure from spectral-element waveform tomography, *Geophys. J. Int*., 199, 1303-1327.

Fukao, Y., M. Obayashi, M., and T. Nakakuki (2009), Stagnant Slab: A Review, *Annu. Rev. Earth Planet. Sci.*, 37, 19–46. doi:10.1146/annurev.earth.36.031207.124224.

Garnero, E.J., and A. K. McNamara (2008), Structure and dynamics of Earth's lower mantle, *Science,* 320, 626–628. doi:10.1126/science.1148028.

Geruo, A., J. Wahr, and S. J. Zhong (2013), Computations of the viscoelastic response of a 3-D compressible Earth to surface loading: an application to glacial isostatic adjustment in Antartica and Canada, *Geophys. J. Int.*, 192, 557-572.

Ghosh, A., T. W. Becker, S. J. Zhong (2010), Effects of lateral viscosity variations on the geoid, *Geophys. Res. Lett.*, 37, L01301. doi:10.1029/2009GL040426

Gilbert, F., and G. E. Backus (1966), Propagator matrices in elastic wave and vibration problems, *Geophys.*, **31**(2), 326–&.

Gordon, R. and D. Jurdy (1986), Cenozoic Global Plate Motions. *J. Geophys. Res.-Solid Earth Planets*, 91, 2389–2406. doi:10.1029/JB091iB12p12389.

Hager, B. (1984), Subducted Slabs and the Geoid - Constraints on Mantle Rheology and Flow, *J. Geophys. Res*., 89, 6003–6015. doi:10.1029/JB089iB07p06003.

Hager, B., R. Clayton, M. Richards, R. Comer, and A. Dziewonski (1985), Lower mantle heterogeneity, dynamic topography and the geoid, *Nature* 313, 541–546.

Hager, B., and R. O'Connell (1981), A simple global-model of plate dynamics and mantle convection, *J. Geophys. Res*., 86, 4843–4867.

Hager, B., M. Richards (1989), Long-wavelength variations in Earth's geoid: Physical models and dynamical implications, *Philos. Trans. R. Soc. Math. Phys. Sci.*, 328, 309–327.

Hernlund, J.W. and C. Houser (2008), The statistical distribution of seismic velocities in Earth's deep mantle, *Earth Planet. Sci. Lett*., 265, 423–437. doi:10.1016/j.epsl.2007.10.042

He, Y. and L. Wen (2009), Structural features and shear-velocity structure of the "Pacific Anomaly'', *J. Geophys. Res.-Solid Earth,* 114, B02309.

He, Y. and L. Wen (2012), Geographic boundary of the "Pacific Anomaly" and its geometry and transitional structure in the north, *J. Geophys. Res.-Solid Earth,* 117, B09308.

Hines, J.M. and M. I. Billen (2012), Sensitivity of the short- to intermediate-wavelength geoid to rheologic structure in subduction zones, *J. Geophys. Res.-Solid Earth,* 117, B05410. doi:10.1029/2011JB008978.

Hofmann, A.W. (1997), Mantle geochemistry: The message from oceanic volcanism, *Nature*, 385, 219–229.

Hofmann, A. W., K. P. Jochum, M. Seufert, and W. M. White (1986), Nb and Pb in oceanic basalts: new constraints on mantle evolution, *Earth Planet. Sci. Lett*., 79, 33-45.

Houser, C., G. Masters, P. Shearer, and G. Laske (2008), Shear and compressional velocity models of the mantle from cluster analysis of long-period waveforms, *Geophys. J. Int*., 174, 195–212. doi:10.1111/j.1365-246X.2008.03763.x.

Huang, J. and G. F. Davies (2007), Stirring in three-dimensional mantle convection models and implications for geochemistry: Passive tracers, *Geochem. Geophys. Geosysts.*, Q03017. doi:10.1029/2006GC001312.

Ita, J., and S. D. King (1994), Sensitivity of convection with an endothermic phase-change to the form of governing equations, initial conditions, boundary conditions, and equation of state, *J. Geophys. Res-Solid Earth*, **99**(B8), 15919–15938.

Jackson, M. G., S. R. Hart, J. G. Konter, M. D. Kurz, J. Blusztajn, and K. Farley (2014), Helium and lead isotopes reveal the geochemical geometry of the Samoan plume, *Nature*, 514, 355-358.

Jaupart, C., S. Labrosse, and J.-C. Mareschal (2007), Temperatures, heat and energy in the mantle of the Earth, *Treatise Geophys*., vol. 7, 253-303.

Jarvis, G. T., and D. P. McKenzie (1980), Convection in a compressible fluid with infinite Prandtl number. *J. Fluid Mech.*, **96**(03), 515.

Jellinek, A.M. and M. Manga (2002), The influence of a chemical boundary layer on the fixity, spacing and lifetime of mantle plumes, *Nature* 418, 760–763.

Karato, S. (1993), Importance of anelasticity in the interpretation of seismic tomography, *Geophys. Res. Lett*., 20, 1623–1626.

Kellogg, L. H., B. H. Hager, R. D. van der Hilst (1999), Compositional stratification in the deep mantle, *Science,* 283, 1881–1884.

King, S. D. (1995), Radial models of mantle viscosity: results from a genetic algorithm, *Geophys. J. Int*., 122: 725–734, doi: 10.1111/j.1365-246X.1995.tb06831.x.

King, S.D., C. Lee, P. E. van Keken, W. Leng, S. J. Zhong, E. Tan, N. Tosi, and M. C. Kameyama (2010), A community benchmark for 2-D Cartesian compressible convection in the Earth's mantle, *Geophys. J. Int*., 180(1), 73–87.

King, S.D., and G. Masters (1992), An inversion for radial viscosity structure using seismic tomography, *Geophys. Res. Lett*., 19, 1551-1554.

Kunz, J., T. Staudacher, C. J. Allegre (1998), Plutonium-fission xenon found in Earth's mantle, *Science*, 280, 877–880.

Lassak, T. M., A. K. McNamara, E. J. Garnero, S. J. Zhong (2010), Core-mantle boundary topography as a possible constraint on lower mantle chemistry and dynamics, *Earth Planet. Sci. Lett*., 289, 232–241.

Leng, W., and S. J. Zhong (2008a), Viscous heating, adiabatic heating and energetic consistency in compressible mantle convection, *Geophys. J. Int.*, **173**(2), 693–702.

Leng, W., and S. J. Zhong (2008b), Controls on plume heat flux and plume excess temperature, *J. Geophys. Res.-Solid Earth*, **113**, B04408, doi:10.1029/2007JB005155.

Leng, W., S. J. Zhong (2011), Implementation and application of adaptive mesh refinement for thermochemical mantle convection studies, *Geochem. Geophys. Geosysts.*, 12, Q04006.

Lerch, F. J., S. M. Klosko, G. B. Patel (1983), A Refined Gravity Model from Lageos (GEML2), NASA Technical Memorandum 84986, Goddard Space Flight Center, Greenbelt/Maryland.

Lithgow-Bertelloni, C., and P. G. Silver (1998), Dynamic topography, plate driving forces and the African superswell, *Nature,* 395, 269–272. doi:10.1038/26212.

Li, Y., F. Deschamps, and P. J. Tackley (2014a), The stability and structure of primordial reservoirs in the lower mantle: insights from models of thermochemical convection in three-dimensional spherical geometry, *Geophys. J. Int.*, 199, 914–930. doi:10.1093/gji/ggu295.

Li, Y., F. Deschamps, and P. J. Tackley (2014b), Effects of low-viscosity post-perovskite on the stability and structure of primordial reservoirs in the lower mantle, *Geophys. Res. Lett*., 41, 7089–7097. doi:10.1002/2014GL061362.

Liu, X., S. J. Zhong (2015), The long-wavelength geoid from three-dimensional spherical models of thermal and thermochemical mantle convection. *J. Geophys. Res.-Solid Earth*, 120, 6.

Marty, J. and A. Cazenave (1989), Regional variations in subsidence rate of oceanic plates: A global analysis, Earth Planet. Sci. *Lett*., 94, 301–315.

Masters, G., S. Johnson, G. Laske, H. Bolton (1996), A shear-velocity model of the mantle, *Philos. Trans. R. Soc. Math. Phys. Sci*., 354, 1385–1410.

Masters, G., G. Laske, H. Bolton, A. Dziewonski (2000), The relative behavior of shear velocity, bulk sound speed, and compressional velocity in the mantle: Implications for chemical and thermal structure, in: *Earth's Deep Interior: Mineral Physics and Tomography From the Atomic to the Global Scale*. pp. 63–87, AGU, Washington, D.C.

McKenzie, D. P, J. M. Roberts, and N. O. Weiss (1974), Convection in Earth's mantle: towards a numerical-simulation, *J. Fluid Mech.*, **62**(3), 465–538.

McNamara, A. K. and S. J. Zhong (2004a), The influence of thermochemical convection on the fixity of mantle plumes, *Earth Planet. Sci. Lett*., 222, 485–500.

McNamara, A.K. and S. J. Zhong (2004b), Thermochemical structures within a spherical mantle: Superplumes or piles? *J. Geophys. Res.-Solid Earth*, 109, B07402.

McNamara, A. K. and S. J. Zhong (2005a), Thermochemical structures beneath Africa and the Pacific Ocean, *Nature*, 437, 1136–1139.

McNamara, A. K. and S. J. Zhong (2005b), Degree-one mantle convection: Dependence on internal heating and temperature-dependent rheology, *Geophys. Res. Lett*., 32, L01301.

Mitrovica, J. X. and A. M. Forte (2004), A new inference of mantle viscosity based upon joint inversion of convection and glacial isostatic adjustment data, *Earth Planet. Sci. Lett*., 225, 177–189. doi:10.1016/j.epsl.2004.06.005.

Molnar, P., P. C. England, and C. H. Jones (2015), Mantle dynamics, isostasy, and the support of high terrain, *J. Geophys. Res. Solid Earth*, 120, 1932–1957, doi: 10.1002/2014JB011724.

Moresi, L. N., and V. S. Solomatov (1995), Numerical investigation of 2d convection with extremely large viscosity variations, *Physics of Fluids*, **7**(9), 2154–2162, doi:10.1063/1.868465.

Moresi, L. and M. Gurnis (1996), Constraints on the lateral strength of slabs from three-dimensional dynamic flow models, *Earth Planet. Sci. Lett*., 138, 15–28.

Moresi, L., S. J. Zhong, and M. Gurnis (1996), The accuracy of finite element solutions of Stokes' flow with strongly varying viscosity, *Phys. Earth Planet. Inter.*, **97**(1-4), 83–94.

Moresi, L. and V. S. Solomatov (1998), Mantle convection with a brittle lithosphere: thoughts on the global tectonic styles of the Earth and Venus, *Geophys. J. Int*., 133, 669–682.

Moucha, R., A. M. Forte, J. X. Mitrovica, A. Daradich (2007), Lateral variations in mantle rheology: implications for convection related surface observables and inferred viscosity models, *Geophys. J. Int*., 169, 113–135, doi:10.1111/j.1365-246X.2006.03225.x.

Murakami, M., K. Hirose, K. Kawamura, N. Sata, and Y. Ohishi (2004), Post-perovskite phase transition in MgSiO3, *Science*, 304, 855–858, doi:10.1126/science.1095932.

Nestola, F., and J. R. Smyth (2015), Diamonds and water in the deep Earth: New perspectives. *International Geology Reviews*, doi: 10.1080/00206814.2015.1056758.

Ni, S. D., E. Tan, M. Gurnis, and D. Helmberger (2002), Sharp sides to the African superplume, *Science*, 296, 1850–1852.

Oldham, D. and J. H. Davies (2004), Numerical investigation of layered convection in a three-dimensional shell with application to planetary mantles, *Geochem. Geophys. Geosysts.*, 5, Q12C04. doi:10.1029/2003GC000603.

O'Neill, C., and A. Lenardic (2007), Geological consequences of super-sized Earths, *Geophys. Res. Lett.*, **34**, L19204, doi:10.1029/2007GL030598.

Panasyuk, S. V., and B. H. Hager (1998), A model of transformational superplasticity in the upper mantle, *Geophys. J. Int.*, 133 (3), 741-755, doi: 10.1046/j.1365-246X.1998.00539.x.

Panasyuk, S. V., and B. H. Hager (2000), Models of isostatic and dynamic topography, geoid anomalies, and their uncertainties, *J. Geophys. Res*., 105(B12), 28199–28209.

Panning, M. P., V. Lekic, and B. A. Romanowicz (2010), The importance of crustal corrections in the development of a new global model of radial anisotropy, *J. Geophys. Res*., 115, B12325.

Paulson, A., S. J. Zhong, and J. Wahr (2007), Limitations on the inversion for mantle viscosity from postglacial rebound, *Geophys. J. Int*., 168, 1195–1209, doi: 10.1111/j.1365-246X.2006.03222.x.

Paulson, A., and M. A. Richards (2009), On the resolution of radial viscosity structure in modelling long-wavelength postglacial rebound, *Geophys. J. Int*., 179, 1516–1526, doi: 10.1111/j.1365-246X.2009.04362.x.

Pavlis, N. K., S. A. Holmes, S. C. Kenyon, and J. K. Factor (2012), Correction to "The Development and Evaluation of the Earth Gravitational Model 2008 (EGM2008), *J. Geophys. Res.-Solid Earth*, 117, B4.

Pekeris, C. L. (1935), The propagation of Rayleigh waves in heterogeneous media, *Phys. J. Gen. Appl. Phys.*, 6, 133–138.

Ratcliff, J. T., P. J. Tackley, G. Schubert, and A. Zebib (1997), Transitions in thermal convection with strongly variable viscosity, *Phys. Earth Planet. Inter*., 102, 201–212.

Ricard, Y., M. Richards, C. Lithgow-Bertelloni, Y. Lestunff (1993), A geodynamic model of mantle density heterogeneity, *J. Geophys. Res.-Solid Earth*, 98, 21895–21909.

Richards, M. A., and B. H. Hager (1989), Effects of lateral viscosity variations on long-wavelength geoid anomalies and topography, *J. Geophys. Res*., 94, doi: 10.1029/89JB00718, 10299-10313.

Ritsema, J., H. J. van Heijst, and J. H. Woodhouse (1999), Complex shear wave velocity structure imaged beneath Africa and Iceland, *Science*, 286, 1925–1928.

Ritsema, J., A. Deuss, H. J. van Heijst, and J. H. Woodhouse (2011), S40RTS: A Degree-40 Shear-Velocity Model For The Mantle From New Rayleigh Wave Dispersion,

Teleseismic Traveltime And Normal-Mode Splitting Function Measurements, *Geophys. J. Int*. 184 (3):1223-1236.doi: 10.1111/j.1365-246X.2010.04884.x.

Romanowicz, B., Y. C. Gung (2002), Superplumes from the core-mantle boundary to the lithosphere: Implications for heat flux, *Science*, 296, 513–516.

Rudolph, M. L., V. Lekić, and C. Lithgow-Bertelloni (2015), Viscosity jump in Earth's mid-mantle, *Science*, 350 (6266), 1349-1352, doi: 10.1126/science.aad1929.

Schilling, J. -G. (1973), Iceland Mantle Plume: Geochemical Study of Reykjanes Ridge, *Nature*, 242, 565-571, doi: 10.1038/242565a0.

Schubert, G., D. L. Turcotte, and P. Olson (2001), Mantle Convection in the Earth and Planets, *Cambridge University Press*, New York, 940.

Schuberth, B. S. A., H.-P. Bunge, and J. Ritsema (2009), Tomographic filtering of high-resolution mantle circulation models: Can seismic heterogeneity be explained by temperature alone? Geochem. Geophys. Geosysts., 10, Q05W03, doi:10.1029/2009GC002401.

Schuberth, B. S. A., C. Zaroli, G. Nolet (2012), Synthetic seismograms for a synthetic Earth: long-period P- and S-wave travel-time variations can be explained by temperature alone, *Geophys. J. Int*., 188, 1393–1412. doi:10.1111/j.1365-246X.2011.05333.x.

Sidorin, I., M. Gurnis, D. V. Helmberger (1999), Evidence for a ubiquitous seismic discontinuity at the base of the mantle, *Science*, 286, 1326–1331, doi:10.1126/science.286.5443.1326

Simons, M. and Hager, B. H. (1997), Localization of the gravity field and the signature of glacial rebound, *Nature*, 390, 500–504. doi:10.1038/37339.

Steinberger, B. and A. R. Calderwood (2006), Models of large-scale viscous flow in the Earth's mantle with constraints from mineral physics and surface observations, *Geophys. J. Int*., 167: 1461–1481. doi: 10.1111/j.1365-246X.2006.03131.x.

Steinberger, B., T. H. Torsvik (2010), Toward an explanation for the present and past locations of the poles, Geochem. Geophys. Geosyst. 11, Q06W06.

Steinbach, V., U. Hansen, and A. Ebel (1989), Compressible convection in the Earth's mantle - a comparison of different approaches, *Geophys. Res. Lett.*, **16**(7), 633–636.

Su, W. J. and A. M. Dziewonski (1997), Simultaneous inversion for 3-D variations in shear and bulk velocity in the mantle, *Phys. Earth Planet. Inter*., 100, 135–156.

Tackley, P. J. (1996), Effects of strongly variable viscosity on three-dimensional compressible convection in planetary mantles, *J. Geophys. Res.*, **101** (B2), 3311-3332.

Tackley, P. J. (1998), Three-dimensional simulations of mantle convection with a thermochemical CMB boundary layer: D"? in: *The Core-Mantle Boundary Region, Geodynamics Series*. pp. 231–253. AGU, Washington, D.C.

Tan, E., and M. Gurnis (2005), Metastable superplumes and mantle compressibility, *Geophys. Res. Lett*., 32, L20307, doi:10.1029/2005GL024190.

Tan, E., W. Leng, S. J. Zhong, and M. Gurnis (2011), On the location of plumes and lateral movement of thermochemical structures with high bulk modulus in the 3-D compressible mantle, *Geochem. Geophys. Geosyst.*, **12**, Q07005, doi:10.1029/2011GC003665.

Tanimoto, T. (1990), Long-wavelength S-wave velocity structure throughout the mantle, *Geophys. J. Int*., 100, 327–336.

Thompson, P. F., and P. J. Tackley (1998), Generation of mega-plumes from the core-mantle boundary in a compressible mantle with temperature-dependent viscosity, *Geophys. Res. Lett.*, **25**(11), 1999–2002.

Thoraval, C., and M. A. Richards (1997), The geoid constraint in global geodynamics: viscosity structure, mantle heterogeneity models and boundary conditions, *Geophys. J. Int*., 131, 1–8.

Tosi, N., O. Cadek, Z. Martinec, D. A. Yuen, G. Kaufmann (2009), Is the long-wavelength geoid sensitive to the presence of postperovskite above the core-mantle boundary? *Geophys. Res. Lett*., 36, L05303, doi:10.1029/2008GL036902.

Turcotte, D. L., and G. Schubert (2002), In: *Geodynamics*, pp 267-272, *Cambridge University Press*, New York.

Valencia, D., D. D. Sasselov, and R. J., O'Connell (2007), Radius and structure models of the first super-Earth planet, *Astrophys. J.*, **656**(1), 545–551.

van Heck, H. J., and P. J. Tackley (2011), Plate tectonics on super-Earths: Equally or more likely than on Earth, *Earth Planet. Sci. Lett.*, **310**(2011), 252–261.

van Keken, P. E., C. J. Ballentine, and D. Porcelli (2001), A dynamical investigation of the heat and helium imbalance, *Earth Planet. Sci. Lett*., 188 (3-4), 421-434.

van Keken, P. E., S. D. King, H. Schmeling, U. R. Christensen, D. Neumeister, M. P. Doin (1997), A comparison of methods for the modeling of thermochemical convection, *J. Geophys. Res.-Solid Earth*, 102, 22477–22495.

Wang, Y., and L. X. Wen (2004), Mapping the geometry and geographic distribution of a very low velocity province at the base of the Earth's mantle, *J. Geophys. Res.-Solid Earth*, 109, B10305.

Wen, L. X., P. Silver, D. James, R. Kuehnel (2001), Seismic evidence for a thermo-chemical boundary at the base of the Earth's mantle, *Earth Planet. Sci. Lett*., 189, 141–153.

Williams, Q., and R. Hemley (2001), Hydrogen in the deep earth, *Annu. Rev. Earth. Planet. Sci*., 29, 365–418.

Wu, W., S. Ni, Z. Shen (2014), Constraining the short scale core–mantle boundary topography beneath Kenai Peninsula (Alaska) with amplitudes of core-reflected PcP wave, *Phys. Earth Planet. Inter*., 236, 60–68. doi:10.1016/j.pepi.2014.09.001.

Zhang, S. X., and U. Christensen (1993), Some Effects of Lateral Viscosity Variations on Geoid and Surface Velocities Induced by Density Anomalies in the Mantle, *Geophys. J. Int*., 114, 531–547. doi:10.1111/j.1365-246X.1993.tb06985.x.

Zhang, N., S. Zhong, W. Leng, Z. X. Li (2010), A model for the evolution of the Earth's mantle structure since the Early Paleozoic, *J. Geophys. Res.-Solid Earth*, 115, B06401.

Zhong, S. J., G. F. Davies (1999), Effects of plate and slab viscosities on the geoid, *Earth Planet. Sci. Lett*., 170, 487–496. doi:10.1016/S0012-821X(99)00124-7.

Zhong, S. J, and M. Gurnis (1993), Dynamic feedback between a continent-like raft and thermal-convection, *J. Geophys. Res.-Solid Earth*, **98**(B7), 12219–12232.

Zhong, S. J., and M. Gurnis (1995), Mantle convection with plates and mobile, faulted plate margins, *Science*, 267, 838–43.

Zhong, S. J., M. T. Zuber, L. Moresi, M. Gurnis (2000), Role of temperature-dependent viscosity and surface plates in spherical shell models of mantle convection, *J. Geophys. Res.-Solid Earth*, 105, 11063–11082.

Zhong, S. J., A. McNamara, E. Tan, L. Moresi, M. Gurnis (2008), A benchmark study on mantle convection in a 3-D spherical shell using CitcomS, Geochem. Geophys. Geosysts. 9, Q10017.

Zhong, S. J., M. Ritzwoller, N. Shapiro, W. Landuyt, J. Huang, and P. Wessel (2007), Bathymetry of the Pacific Plate and its implications for thermal evolution of lithosphere and mantle dynamics, *J. Geophys. Res*., 112, B06412, doi:10.1029/2006JB004628.

Zhong, S. J., and A. B. Watts (2013), Lithospheric deformation induced by loading of the Hawaiian Islands and its implications for mantle rheology, *J. Geophys. Res.-Solid Earth*, 118, 6025–6048.

Zhong, S., N. Zhang, Z. X. Li, J. H. Roberts (2007), Supercontinent cycles, true polar wander, and very long-wavelength mantle convection, *Earth Planet. Sci. Lett*., 261, 551–564.

Zhong, S. J, A. K. McNamara, E. Tan, L. Moresi, and M. Gurnis (2008), A benchmark study on mantle convection in a 3-D spherical shell using CitcomS, *Geochem. Geophys. Geosyst*., 9, Q10017, doi:10.1029/2008GC002048.

Appendixes[4]

A. Marginal stability analysis using a propagator matrix method

The marginal linear stability problem for compressible flow is governed by equations (2.18)-(2.20). Leng & Zhong (2008a) constructed a propagator matrix for the Stokes' flow problem for a compressible fluid (i.e., equations (2.18) and (2.19)). Based on their method, we add the linearized energy equation (2.20) and set up the propagator matrix for the marginal linear stability problem.

In the linearized governing equations (2.18)-(2.20), the dependences of the velocities, pressure and stresses perturbations on *x* and *z* are separable. Horizontal component of the perturbations is represented by sinusoidal functions, but vertical component of the perturbations is represented by arbitrary functions. The time-dependence of the perturbations is expressed by an exponential function of time with a growth rate α'.

The perturbations should satisfy boundary conditions. The free-slip boundary condition requires that $\tau'_{xz} = u' = 0$ at $x = 0$ and 1, and $\tau'_{xz} = v' = 0$ at $z = 0$ and 1. The fixed temperature boundary condition requires that $T' = 0$ at $z = 0$ and 1.

The perturbations can be expressed in Fourier transform as

[4] The appendixes are in the paper "Liu, X., and S.J. Zhong, 2013. Analysis of marginal stability, heat transfer and boundary layer propoerties for thermal convection in a compressible fluid, *Geophys. J. Int*, **194**, 125-144"

$$
\begin{aligned}
T' &= \int T_0(z)\cos(\mathrm{k}_x x)e^{\alpha' t}\mathrm{dk}_x \\
u' &= \int U(z)\sin(\mathrm{k}_x x)e^{\alpha' t}\mathrm{dk}_x \\
v' &= \int V(z)\cos(\mathrm{k}_x x)e^{\alpha' t}\mathrm{dk}_x \\
\tau'_{xz} &= \int Y_{xz}(z)\sin(\mathrm{k}_x x)e^{\alpha' t}\mathrm{dk}_x \\
\sigma'_{zz} &= \int S_{zz}(z)\cos(\mathrm{k}_x x)e^{\alpha' t}\mathrm{dk}_x
\end{aligned}
\tag{A1}
$$

where k_x is the horizontal wave-number, $T_0(z)$, $U(z)$, $V(z)$, $Y_{xz}(z)$ and $S_{zz}(z)$ represent the vertical dependence of the perturbations corresponding to k_x. The boundary conditions $T' = v' = \tau' = 0$ at $z = 0$ and 1 require that

$$T_0 = V = Y_{xz} = 0 \text{ at } z = 0 \text{ and } 1. \tag{A2}$$

Linearized governing equations (2.18)-(2.20) should be formulated into a vector linear differential equation (2.22) so that it can be solved by a propagator matrix method. Based on a velocity-stress formulation, the vector W in equation (2.22) is chosen as (2.23). Linearized governing equations and constitutive equation are rearranged such that only items in vector W are used in the equations as unknown variables. In the following equations, non-dimensional forms are used and the variables with a prime are perturbations in the linearized equations.

Considering the depth-dependent density profile (equation 2.16), non-dimensional linearized mass conservation equation (2.18) can be rewritten as:

$$\left(\rho_r u'_i\right)_{,i} = \rho_{r,i} u'_i + \rho_r u'_{i,i} = -Die^{Di(1-z)}v' + e^{Di(1-z)}u'_{i,i} = 0, \tag{A3}$$

or

$$\frac{\partial u'}{\partial x} + \frac{\partial v'}{\partial z} - v'Di = 0, \tag{A4}$$

The total stress σ_{ij} can be related to dynamic pressure p and deviatoric stress τ_{ij} as

$$\sigma_{ij} = -p\delta_{ij} + \tau_{ij}, \tag{A5}$$

where τ_{ij} is given in equation (2.7). From equation (A5), σ_{zz} and p are

$$\sigma_{zz} = -p + \eta[2\frac{\partial v}{\partial z} - \frac{2}{3}(\frac{\partial u}{\partial x} + \frac{\partial v}{\partial z})], \tag{A6}$$

$$p = \frac{4}{3}\eta\frac{\partial v}{\partial z} - \frac{2}{3}\eta\frac{\partial u}{\partial x} - \sigma_{zz}. \tag{A7}$$

Substituting (A7) into the x component momentum conservation equation (2.19) leads to

$$\frac{\partial \sigma'_{zz}}{\partial x} + \frac{\partial \tau'_{xz}}{\partial z} + 4\eta\frac{\partial^2 u'}{\partial x^2} - 2\eta\gamma\frac{\partial v'}{\partial x} = 0, \tag{A8}$$

Substituting (A7) into the z-component of equation (2.19) leads to

$$\frac{\partial \sigma'_{zz}}{\partial z} + \frac{\partial \tau'_{xz}}{\partial x} + Ra(\alpha g)\rho_r(T - T_r) - \frac{g}{c_P\Gamma}\alpha\gamma(\frac{4}{3}\eta\frac{\partial v'}{\partial z} - \frac{2}{3}\eta\frac{\partial u'}{\partial x} - \sigma'_{zz}) = 0. \tag{A9}$$

The non-dimensional linearized energy equation (2.20) may be written as:

$$\rho_r c_P\dot{T}' + \rho_r c_P v'\frac{\mathrm{d}T_r}{\mathrm{d}z} + \rho_r v' Di\alpha g\Gamma(T_r + T_s) = k(\frac{\partial^2 T'}{\partial x^2} + \frac{\partial^2 T'}{\partial z^2}). \tag{A10}$$

From the constitutive equation (2.7),

$$\tau_{xz} = \eta(\frac{\partial u}{\partial z} + \frac{\partial v}{\partial x}). \tag{A11}$$

For each wave-number k_x, combining equations (A4), (A8)-(A11), and eliminating $\sin(\mathrm{k}_x x)$, $\cos(\mathrm{k}_x x)$ and $e^{\alpha' t}$, these equations can be written as:

$$\frac{\mathrm{d}U}{\mathrm{d}z} = \mathrm{k}_x V + \frac{1}{\eta}Y_{xz}, \tag{A12}$$

$$\frac{\mathrm{d}V}{\mathrm{d}z} = -\mathrm{k}_x U + \gamma V, \tag{A13}$$

$$\frac{\mathrm{d}S_{zz}}{\mathrm{d}z} = -2\eta\mathrm{k}_x\gamma(\frac{\alpha g}{c_P\Gamma})U + \frac{4}{3}\eta\gamma^2(\frac{\alpha g}{c_P\Gamma})V - (\frac{\alpha g}{c_P\Gamma})\gamma - \mathrm{k}_x Y_{xz} - Ra\rho_r(\alpha g)T_0, \tag{A14}$$

$$\frac{\mathrm{d}Y_{xz}}{\mathrm{d}z} = 4\eta \mathrm{k}_x{}^2 U - 2\eta \mathrm{k}_x \gamma V + \mathrm{k}_x S_{zz}, \tag{A15}$$

$$\frac{\mathrm{d}}{\mathrm{d}z} T_0 = \frac{\mathrm{d}T_0}{\mathrm{d}z} \ , \tag{A16}$$

$$\frac{\mathrm{d}}{\mathrm{d}z}\frac{\mathrm{d}T_0}{\mathrm{d}z} = \frac{\rho_r}{k}[Di(\alpha g)(1 - z + T_s) - c_P]V + [\frac{\rho_r c_P \alpha'}{k} + \mathrm{k}_x{}^2]T_0 \ . \tag{A17}$$

Equations (A12)-(A17) may be written as a vector equation (2.22) or dW/dz = AW, and the vector W and the matrix A are defined in equations (A18) and (A19):

$$\mathrm{W} = \left(V, U, \frac{S_{zz}}{2\mathrm{k}_x}, \frac{Y_{xz}}{2\mathrm{k}_x}, T_0, \frac{\mathrm{d}T_0}{\mathrm{d}z}\right)^{\mathrm{T}}, \tag{A18}$$

$$\mathrm{A} = \begin{pmatrix} Di & -\mathrm{k}_x & 0 & 0 & 0 & 0 \\ \mathrm{k}_x & 0 & 0 & \frac{2\mathrm{k}_x}{\eta} & 0 & 0 \\ \frac{2\eta g}{3c_P\Gamma}\frac{\alpha Di^2}{\mathrm{k}_x} & -\frac{g\eta}{c_P\Gamma}\alpha Di & -\frac{g}{c_P\Gamma}\alpha Di & -\mathrm{k}_x & -g\frac{\alpha Ra\rho_r}{2\mathrm{k}_x} & 0 \\ -Di\eta & 2\mathrm{k}_x\eta & \mathrm{k}_x & 0 & 0 & 0 \\ 0 & 0 & 0 & 0 & 0 & 1 \\ \frac{\rho_r \alpha g}{k}\left[Di(1 - z + T_s) - c_P\right] & 0 & 0 & 0 & \left(\frac{c_P \alpha' \rho_r}{k} + \mathrm{k}_x{}^2\right) & 0 \end{pmatrix}, \tag{A19}$$

where the superscript T for equation (A18) represents matrix transpose. We assume that all the parameters in matrix A except for ρ_r in (A19) are constant and independent of *z*. This leads to dimensionless parameters *g*, c_P, Γ, η, α, and *k* in (A19) to be 1, and matrix A may be written as:

$$\mathrm{A} = \begin{pmatrix} Di & -\mathrm{k}_x & 0 & 0 & 0 & 0 \\ \mathrm{k}_x & 0 & 0 & 2\mathrm{k}_x & 0 & 0 \\ \frac{2}{3}\frac{Di^2}{\mathrm{k}_x} & -Di & -Di & -\mathrm{k}_x & -\frac{Ra\rho_r}{2\mathrm{k}_x} & 0 \\ -Di & 2\mathrm{k}_x & \mathrm{k}_x & 0 & 0 & 0 \\ 0 & 0 & 0 & 0 & 0 & 1 \\ \rho_r\left[Di(1 - z + T_s) - 1\right] & 0 & 0 & 0 & \left(\alpha'\rho_r + \mathrm{k}_x{}^2\right) & 0 \end{pmatrix}. \tag{A20}$$

We then discuss solution procedures of equation (2.22) using a propagator matrix method. Propagator matrix method was proposed by Gilbert & Backus (1966) and is widely used to solve vector linear differential equation in the form of equation (2.22). Equation (2.22) has a solution:

$$\mathrm{W}(z) = e^{\mathrm{A}(z-z_0)}\mathrm{W}(z_0) = \mathrm{P}(z, z_0)\mathrm{W}(z_0), \tag{A21}$$

where

$$\mathrm{P}(z, z_0) = e^{\mathrm{A}(z-z_0)} \tag{A22}$$

is a propagator matrix that has the same dimensions as matrix A (i.e., 6×6), and $\mathrm{W}(z_0)$ is vector W at $z = z_0$ (e.g., at a boundary).

If matrix A is dependent on z, the solution at any depth can be obtained by propagating along z direction from a starting point z_0 with

$$\begin{aligned} \mathrm{W}(z_n) &= \mathrm{P}(z_n, z_{n-1})\mathrm{P}(z_{n-1}, z_{n-2})\cdots\mathrm{P}(z_2, z_1)\mathrm{P}(z_1, z_0)\mathrm{W}(z_0) \\ &= \mathrm{P}_n\mathrm{P}_{n-1}\cdots\mathrm{P}_2\mathrm{P}_1\mathrm{W}(z_0) = \mathrm{P}\mathrm{W}(z_0) \end{aligned}, \tag{A23}$$

where $\mathrm{P}_i = e^{\mathrm{A}_i(z_i - z_{i-1})}$ is a propagator matrix between z_i and z_{i-1} over which A_i and P_i can be treated as constant matrices.

Given boundary conditions (A2), vectors W at z=1 and z=0, denoted as W_1 and W_0, respectively, are

$$\mathrm{W}_1 = \left(0, U(z=1), \frac{S_{zz}(z=1)}{2\mathrm{k}_x}, 0, 0, \frac{\mathrm{d}T_0}{\mathrm{d}z}_{z=1}\right)^{\mathrm{T}}, \tag{A24}$$

$$\mathrm{W}_0 = \left(0, U(z=0), \frac{S_{zz}(z=0)}{2\mathrm{k}_x}, 0, 0, \frac{\mathrm{d}T_0}{\mathrm{d}z}_{z=0}\right)^{\mathrm{T}}, \tag{A25}$$

and from equation (A21)

$$\mathrm{W}_1 = \mathrm{P}(1,0)\mathrm{W}_0 . \tag{A26}$$

Propagator matrix P(1,0) in equation (A26) is constructed as given in (A22) and (A23), based on a grid between z=0 and z=1 from z-dependent matrix A. There are six unknowns in W_1 and W_0: horizontal velocity U, vertical normal stress $S_{zz}/2k_x$, and dT_0/dz at the surface and bottom boundaries, and they are represented as x, y, z, a, b, and c, respectively. Equation (A26) can be written as

$$\begin{aligned} 0 &= P_{12}a + P_{13}b + P_{16}c \\ 0 &= P_{42}a + P_{43}b + P_{46}c \\ 0 &= P_{52}a + P_{53}b + P_{56}c \\ x &= P_{22}a + P_{23}b + P_{26}c \\ y &= P_{32}a + P_{33}b + P_{36}c \\ z &= P_{62}a + P_{63}b + P_{66}c \end{aligned}, \qquad \text{(A27)}$$

where P_{ij} is the ij item of propagator matrix P(1,0). Equation (A27) may be rearranged as:

$$\begin{pmatrix} P_{12} & P_{13} & P_{16} & 0 & 0 & 0 \\ P_{42} & P_{43} & P_{46} & 0 & 0 & 0 \\ P_{52} & P_{53} & P_{56} & 0 & 0 & 0 \\ P_{22} & P_{23} & P_{26} & -1 & 0 & 0 \\ P_{32} & P_{33} & P_{36} & 0 & -1 & 0 \\ P_{62} & P_{63} & P_{66} & 0 & 0 & -1 \end{pmatrix} \begin{pmatrix} a \\ b \\ c \\ x \\ y \\ z \end{pmatrix} = 0 \qquad \text{(A28)}$$

A non-trivial solution for equation (A28) requires that the determinant of the 6×6 matrix in equation (A28) is zero, which in turn requires

$$\det \begin{pmatrix} P_{12} & P_{13} & P_{16} \\ P_{42} & P_{43} & P_{46} \\ P_{52} & P_{53} & P_{56} \end{pmatrix} = 0 . \qquad \text{(A29)}$$

Equation (A29) forms the basis of our marginal stability analysis using the propagator matrix technique.

For a given set of thermodynamic parameters, mantle compressibility, density structure, and wave-number of the perturbation, there are two unknown parameters in matrix A in (A20) or matrix E in (A29): the growth rate α' and the Rayleigh number *Ra*. Note that critical Rayleigh number Ra_c is defined as *Ra* which makes $\alpha' = 0$. A search scheme is developed to determine Ra_c: setting $\alpha' = 0$, we compute det(E) for different *Ra*, and when det(E)=0, *Ra* equals Ra_c. Different Ra_c can be determined for different wave-number k_x and other model parameters such as the dissipation number *Di*.

To illustrate the search scheme, we present contour plots of det(E) in the *Ra*-α' space in Figure A1 for two calculations with $k_x=\pi$ and *Di*=0 and *Di*=2, respectively. For *Di*=0, it is observed that the zero contours of det(E), which we use to find Ra_c at $\alpha' = 0$, are straight lines, indicating that in the limit of weak convection, growth rate increases linearly with *Ra*. As there are multiple zero contour lines of det(E) (Fig. A1a), more than one Ra_c can be obtained, and each Ra_c is for a distinct mode. We use n=0 to represent the fundamental mode and n=1, 2, … to represent the first, second, … mode. The value of n represents the number of nodes where the vertical flow velocity is zero (excluding *z*=0 and *z*=1), and n+1 is the number of convection cells that are stacked in the vertical direction. For the range of *Ra* shown in Fig. A1, zero contours of det(E) cross the α'=0 line twice for *Di*=0 but only once for *Di*=2. What mode each zero contour of det(E) corresponds to depends on eigenfunction of vertical flow velocity *V(z).*

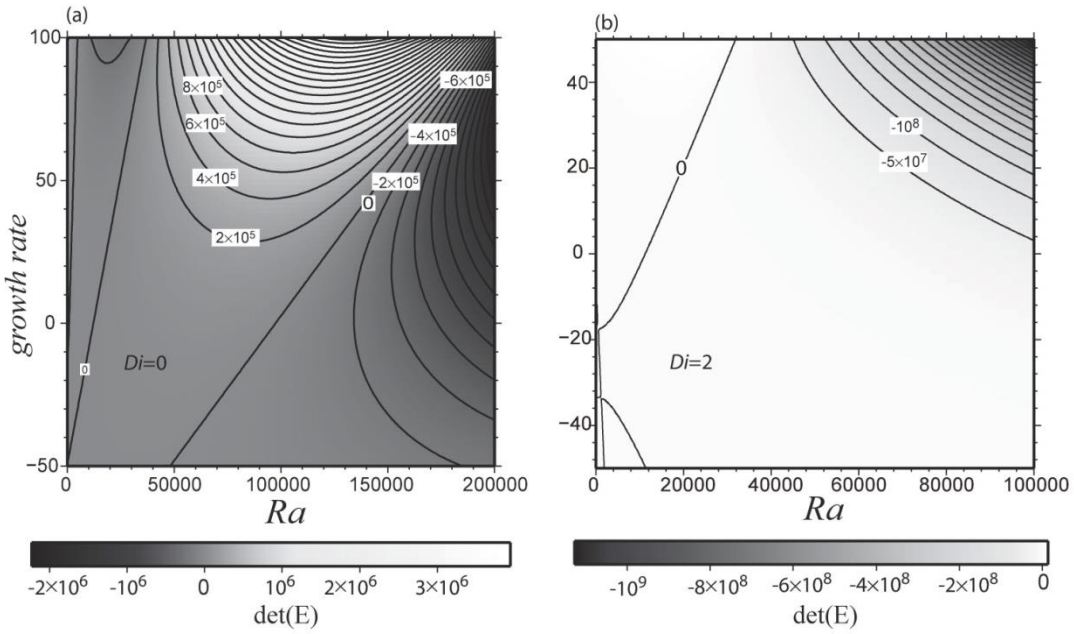

Figure A1. Contour plots of the determinant of matrix E in growth rate α' and *Ra* space for cases with $k_x=\pi$ and (a) *Di*=0 and (b) *Di*=2.

The eigenfunctions of $T_0(z)$, $U(z)$ and $V(z)$ are also determined from the propagator matrix method. First, we need to determine $W_0 = W(z=0)$ in equation (A24). From equations (A24)-(A26), we get

$$EW_0^{sub} = \begin{pmatrix} P_{12} & P_{13} & P_{16} \\ P_{42} & P_{43} & P_{46} \\ P_{52} & P_{53} & P_{56} \end{pmatrix} \begin{pmatrix} U(z=0) \\ \dfrac{S_{zz}}{2k_x}(z=0) \\ \dfrac{dT_0}{dz}_{z=0} \end{pmatrix} = 0, \qquad \text{(A30)}$$

where W_0^{sub} consists of the three non-zero items of W_0. Since det(E)=0, W_0^{sub} cannot be uniquely determined. However, we seek for a solution by fixing $dT_0/dz_{z=0}=1$. For a given set of model parameters (e.g., *Di* and k_x), propagator matrix P(*z*,0) is formed by equations (A22) and (A23), using $Ra_c = Ra$ and growth rate $\alpha' = 0$ in matrix A (i.e.,

equation A20). With W_0 and the propagator matrix P(*z*,0), W(*z*) (i.e., the eigenfunctions) can be computed from equation (A23). In Figure 2.2, we show eigenfunctions of $T_0(z)$, $U(z)$, and $V(z)$ for some selective cases. Note that $T_0(z)$ is scaled such as its maximum value is 1, and $U(z)$ and $V(z)$ are scaled accordingly.

Based on $V(z)$, we also determined that the two modes in Fig. A1a for Di=0 are for n=0 and n=1 modes, while the only mode in Fig. A1b for Di=2 is for n=1 mode. The latter suggests that for Di=2, n=0 mode (i.e., the fundamental mode) does not exist. In this study, we use 129 uniform grid points in *z* direction to compute propagator matrix for all the results shown in section 2.3.2.

B. Quantifying thermal boundary layer (TBL) properties.

In compressible convection, an isentropic central region is developed (e.g., Jarvis & McKenzie, 1980), and the adiabatic temperature follows equation (2.35). While the horizontally average temperature follows adiabatic temperature T_{ad} in the isentropic central regime, it deviates significantly from T_{ad} within the top and bottom TBLs (i.e., super-adiabatic). Here we describe how the thicknesses and temperature difference of TBLs are defined and quantified.

As an example, Fig. B1b shows the gradients of typical horizontally averaged temperature $\mathrm{d}T/\mathrm{d}z$ and of adiabatic temperature $\mathrm{d}T_{ad}/\mathrm{d}z$ (computed from equation 2.35) for case AC1017, where Di=1 and Ra=10^7. The temperature gradient deviates from adiabatic gradient in the top and bottom TBLs and we define the bottom (top) of the top (bottom) TBL as where the deviation of temperature gradient starts to develop:

$$\left(\left|\frac{\mathrm{d}T}{\mathrm{d}z}\right| - \left|\frac{\mathrm{d}T_{ad}}{\mathrm{d}z}\right|\right)/\left(Nu - \left|\frac{\mathrm{d}T_{ad}}{\mathrm{d}z}\right|\right) > \varepsilon . \qquad \text{(B1)}$$

In equation (B1), ε is a small value, and in our study is set as 0.2, and $\mathrm{d}T_{ad}/\mathrm{d}z$ in both numerator and denominator is the adiabatic temperature gradient at depth z. Equation (B1) measures super-adiabatic gradient normalized by surface super-adiabatic gradient and helps to determine the top and bottom TBL thicknesses δ_t and δ_b. The choice of ε affects the values of δ_t and δ_b. The larger ε is, the smaller δ_t and δ_b are. However, we found that the ratios of TBL thicknesses and the scalings of such determined TBL properties are insensitive to the choice of ε. After δ_t and δ_b are determined, the temperature difference in TBLs, ΔT_t and ΔT_b can be determined from the horizontally averaged temperature profile (Fig. B1a). Interpolation is needed to obtain ΔT_l, because δ_t and δ_b do not necessarily occur at the grid points. For each case, we determine average TBL thickness and temperature difference over a large

number of time steps for steady-state or quasi-steady state solutions. The adiabatic temperature is also plotted in Fig. B1a. Since equation (2.35) might not be applicable within TBLs, here we assume that the adiabatic temperatures within the top and bottom TBLs are assumed to be the same as those outside the TBLs. This assumption is valid because the TBLs are very thin, and ΔT_{adi} within TBLs should be very small.

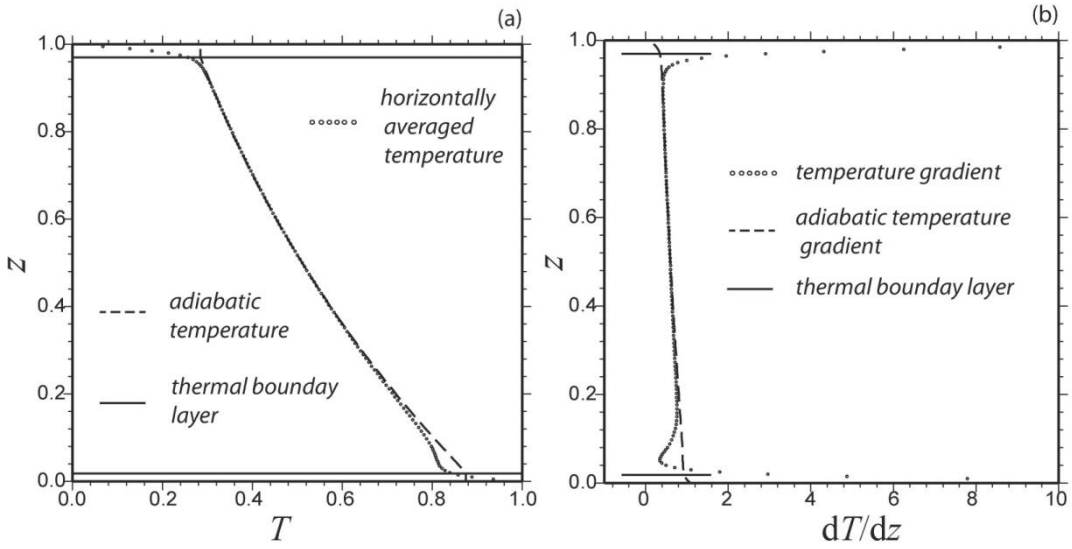

Figure B1. (a) Horizontally averaged temperature profile for case AC1017, with *Di* = 1.0, and *Ra* = 10^7. (b) Temperature gradients for case AC1017. In both (a) and (b), the dotted lines are the horizontally averaged temperature (gradient), where dots show the grid points in the numerical models. The dashed lines are the adiabatic temperature (gradient) (equation 2.35). The solid lines in both figures show the TBLs determined by the method introduced in Appendix B.